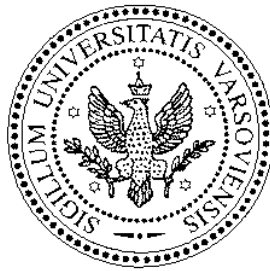


Search for the heavy,
neutral MSSM Higgs particles
in the $H/A \rightarrow \tau\tau \rightarrow \mu + X$ channel
in the CMS detector at the LHC



Artur Kalinowski

Institute of Experimental Physics

Warsaw University

A thesis submitted in the partial fulfillment

for the degree of Doctor of Philosophy in Physics

written under the supervision of Prof. J. Królikowski

Warsaw, July 2006

Acknowledgements

I would like to thank my supervisor Prof. Jan Królikowski for his guidance over years of my M.Sc. and Ph.D. studies.

I would like to thank Prof. Krzysztof Doroba, head of the Division of Particles and Fundamental Interactions of the Faculty of Physics at Warsaw University, for his open attitude to all students and readiness to help in all issues.

I am grateful to Dr. Alexandre Nikitenko, head of the CMS Higgs group, for all his comments and inspiration.

I would like to thank Dr. Danek Kotliński for his hospitality during my visits to the Paul Scherrer Institute, and further help with my work.

Finally I would like to thank my colleagues from the CMS Warsaw group, for their readiness to help and many fruitful discussions. In particular I would like to thank Dr. Marcin Konecki and M.Sc. Paweł Zych.

Abstract

This thesis is devoted to search for heavy, neutral, supersymmetric Higgs particles H and A in the $H/A \rightarrow \tau\tau \rightarrow \mu + \text{hadrons} + X$ decay channel at the CMS detector. Standard selection procedure, based on consecutive cuts on basic physics objects, has been implemented within the object oriented framework for the physics analysis of the CMS experiment. Full detector simulation and reconstruction software was used to determine the CMS detector discovery reach in the $\langle m_A, \tan(\beta) \rangle$ plane for 20 fb^{-1} integrated luminosity (one year with low LHC accelerator luminosity) for the representative choice of the MSSM parameters.

Various detector systematics effects, in particular those arising from uncertainty on the absolute calorimetry energy scale, were investigated.

Analysis of agreement between the Next to Leading Order calculations for the $gg \rightarrow b\bar{b}H$ production and PYTHIA used for the simulation was examined.

A method for estimating the τ tagging efficiency from the experimental data was developed.

Contents

1	Introduction	1
2	Minimal Supersymmetric Standard Model	4
2.1	Overview	4
2.2	Particle content of the MSSM	6
2.3	Higgs sector in MSSM	6
2.4	Supersymmetry breaking	10
3	Cross sections predictions	13
3.1	Signal cross section calculations	13
3.2	Background cross section calculations	14
4	CMS experiment	20
4.1	Introduction	20
4.2	Detector	21
4.2.1	Tracking detectors	21
4.2.1.1	Pixel detectors	22
4.2.1.2	Silicon detectors	22
4.2.2	Calorimetry	23
4.2.2.1	Electromagnetic calorimeter	24
4.2.2.2	Hadronic calorimeter	25
4.2.3	Muon detectors	25
4.3	Triggering system	26
4.4	Reconstruction	28
4.4.1	Tracks	28
4.4.2	Vertices	29
4.4.3	Muons	30
4.4.4	Electrons and photons	31
4.4.5	Jets	33
4.4.6	b tagging	34

4.4.7	Missing transverse energy	35
5	Physics simulation	38
5.1	Generation	38
5.1.1	Introduction	38
5.1.2	The generation procedures	39
5.2	Simulation	41
5.3	Digitization	42
6	Analysis	44
6.1	Trigger path	44
6.1.1	Level 1 trigger	44
6.1.2	High Level Trigger	44
6.2	Offline selections	46
6.2.1	Offline τ identification	47
6.2.2	Background suppression specific selections	47
6.2.2.1	Leading τ – jet track p_T cut	47
6.2.2.2	Opposite charge of the μ and τ – jet signal tracks	48
6.2.2.3	Single b tagging	48
6.2.2.4	Central jet veto	49
6.2.2.5	Transverse mass cut	49
6.2.2.6	Electron veto	49
6.2.3	Mass reconstruction specific cuts	49
6.2.4	Thresholds optimization	50
6.2.5	Efficiencies	52
6.3	Higgs boson mass reconstruction	53
6.3.1	The method	53
6.3.2	Impact of the \cancel{E}_T measurement	56
6.4	Background contribution estimates	58
6.4.1	The non Z background process	58
6.4.2	The Z background	60
7	Results	62
7.1	Results for the m_h^{\max} scenario	62
7.2	Dependency on the MSSM parameters	65
8	Conclusions	67
	Appendices	70

A	Comparison between MCFM and PYTHIA for the $g b \rightarrow b h$ and $g g \rightarrow b b h$ processes at the LHC	70
A.1	Introduction	70
A.2	Simulation setup	71
A.3	Comparison of PYTHIA and MCFM at leading order	71
A.4	Comparison of next-to-leading order MCFM and PYTHIA	72
A.5	Conclusions	73
B	QCD events simulation	78
C	Selection efficiencies as a function of the threshold	81
D	Correlations between selection variables	86
D.1	$b\bar{b}H$ with $m_A = 200 \text{ GeV}/c^2$	87
D.2	$t\bar{t}$	89
E	Plots used for the selections thresholds optimization	92
F	Trigger and offline selection efficiencies	97
F.1	Trigger selections	97
F.2	Offline selections	100
G	Measurement of the τ tag efficiency using the $Z \rightarrow \tau\tau \rightarrow \mu + \text{hadrons} + X$ events	103
G.1	Introduction	103
G.2	The method	104
G.3	Background	105
G.4	Experimental selections	106
G.4.1	Trigger selection	106
G.4.2	Offline selection	106
G.5	Selection uncertainty due to the calorimeter scale	107
G.5.1	Signal	108
G.5.2	Background	109
G.6	Results	111
G.6.1	Total uncertainty on the number of background events . .	111
G.6.2	Total uncertainty on the τ tag efficiency	113
G.7	Conclusions	114

CONTENTS

References	122
------------	-----

List of Figures

2.1	Fermion loop correction to the Higgs boson propagator.	5
2.2	Scalar loop corrections to the Higgs boson propagator.	6
2.3	The $\cos^2(\beta - \alpha)$ as a function of the m_A , for the $\tan(\beta) = 30$. . .	9
3.1	Example of the leading order diagrams for the Higgs boson production.	13
3.2	Example of the leading order diagram for the Higgs boson production.	14
3.3	Cross section times $\text{BR}(A/H \rightarrow \tau\tau)$ for associated $b\bar{b}H/A$ production via gluon fusion as a function of m_A for $\tan(\beta) = 20$	15
3.4	Cross section times $\text{BR}(A/H \rightarrow \tau\tau)$ for associated $b\bar{b}H/A$ production via gluon fusion as a function of $\tan(\beta)$	15
3.5	The decay widths of the Higgs bosons A and H as a function of m_A for $\tan(\beta) = 20$	16
3.6	The decay widths of the Higgs bosons A and H as a function of $\tan(\beta)$ for $m_A = 200 \text{ GeV}/c^2$	16
3.7	Pseudoscalar Higgs boson branching ratios as a function of m_A for $\tan(\beta) = 20$	17
3.8	Higgs boson branching ratio into $\tau\tau$ as a function of $\tan(\beta)$ for $m_A = 200 \text{ GeV}/c^2$	17
4.1	The CMS detector.	21
4.2	View of the CMS tracking system	22
4.3	Longitudinal view of one quadrant of the CMS detector.	23
4.4	Electromagnetic calorimeter supermodule resolution.	24
4.5	Energy response of the ECAL+HE system for single pions as a function of the beam momentum.	25
4.6	View of the CMS muon system.	26
4.7	Cross section for selected processes to be observed at the LHC. . .	27
4.8	Muon p_T resolution.	31
4.9	Electron energy resolution.	32

LIST OF FIGURES

4.10	Photon energy resolution.	33
4.11	Jet transverse energy resolution for three η regions of the CMS detector.	35
4.12	Track counting b miss tag probability versus the b tag efficiency. .	36
4.13	Error on the reconstructed missing transverse energy.	37
4.14	Missing transverse energy direction resolution.	37
5.1	Material budget of the tracker system.	42
6.1	Definition of the cones used for the τ jet isolation.	45
6.2	Direction resolution of the τ jet for $m_A = 200 \text{ GeV}/c^2$	48
6.3	Relative orientation of the $\vec{\cancel{E}}_T$, \vec{p}_T^μ and $\vec{E}_T^{\tau \text{ jet}}$ on the XY plane. . .	50
6.4	Reconstructed and generated transverse energy of the neutrinos from τ decays.	51
6.5	Mass distribution for the signal with $m_A = 200 \text{ GeV}/c^2$ and all background sources.	52
6.6	Mass distribution for the signal with $m_A = 200 \text{ GeV}/c^2$ and all background sources.	52
6.7	Delta R between the neutrino and the generated charged particles, for $m_A = 200 \text{ GeV}/c^2$	55
6.8	Reconstructed Higgs boson mass.	56
6.9	Reconstructed Higgs boson mass in the limit of the ideal $\vec{\cancel{E}}_T$ recon- struction.	57
6.10	Reconstructed Higgs boson mass.	57
6.11	Reconstructed $\tau\tau$ invariant mass after all offline selections for $f < 0.1$. .	59
6.12	Ratio of the selection efficiency for the jet and missing E_T scale variations.	61
7.1	The reconstructed Higgs boson mass.	63
7.2	The reconstructed $\tau\tau$ mass for the two main background processes after the offline selection: Z/γ^* and $t\bar{t}$	63
7.3	Five sigma contour in the $< m_A, \tan(\beta) >$ plane for the 20 fb^{-1} . .	64
7.4	Five sigma contour, calculated assuming 12% systematic error on the number of background events.	66
8.1	Five sigma contours, calculated including systematic error on the number of background events.	68
A.1	The p_T of the b quark in PYTHIA and LO MCFM for $g b \rightarrow b h$ process, $m_h = 500 \text{ GeV}/c^2$. See more explanations in the text. . . .	74

A.2	The Higgs boson mass distribution in PYTHIA and MCFM for $m_h=500 \text{ GeV}/c^2$	74
A.3	The p_T of the leading b jet in PYTHIA and in MCFM for $m_h=200 \text{ GeV}/c^2$	75
A.4	The p_T of the leading b jet in PYTHIA and in MCFM for $m_h=500 \text{ GeV}/c^2$	75
A.5	The p_T of the second b jet in PYTHIA and in MCFM for $m_h=200 \text{ GeV}/c^2$	75
A.6	The p_T of the second b jet in PYTHIA and in MCFM for $m_h=500 \text{ GeV}/c^2$	75
A.7	The η of the leading b jet in PYTHIA and in MCFM for $m_h=200 \text{ GeV}/c^2$	76
A.8	The η of the leading b jet in PYTHIA and in MCFM for $m_h=500 \text{ GeV}/c^2$	76
A.9	The η of the second b jet in PYTHIA and in MCFM for $m_h=200 \text{ GeV}/c^2$	76
A.10	The η of the second b jet in PYTHIA and in MCFM for $m_h=500 \text{ GeV}/c^2$	76
A.11	The p_T of the Higgs boson for the leading b jet in the tagging range and no other jets in the central region, $m_h=200 \text{ GeV}/c^2$	77
A.12	The p_T of the Higgs boson for the leading b jet in the tagging range and no other jets in the central region, $m_h=500 \text{ GeV}/c^2$	77
B.1	Muon rate for muons coming from the b quarks.	79
B.2	The origin of muons for the events passing the $\mu\tau$ HLT selection for low luminosity.	80
C.1	Integrated distribution of μp_T	81
C.2	Integrated distribution for τ – jet E_T	82
C.3	The τ – jet leading track p_T integrated distribution the events with 1 track in the signal cone.	82
C.4	The τ – jet leading track p_T integrated distribution for the events with 3 tracks in the signal cone.	83
C.5	First b tagged jet E_T integrated distribution.	83
C.6	Integrated distribution for E_T of central jet additional to τ jet and b tagged jet.	84
C.7	Integrated distribution of transverse mass of the muon and the missing E_T	84

LIST OF FIGURES

C.8	Integrated distribution of the ratio of the τ – jet hadronic energy and the leading track momentum.	85
C.9	Integrated distribution of the cosine of the azimuthal angle between the muon and the τ – jet directions.	85
D.1	Integrated distribution of the τ – jet leading track p_T	87
D.2	Integrated distribution of the transverse mass of the muon and the missing E_T	87
D.3	Integrated distribution of the cosine of the azimuthal angle between the muon and the τ – jet directions.	88
D.4	Integrated distribution of the ratio of the τ – jet hadronic energy and the leading track momentum.	88
D.5	Integrated distribution of the first b tagged jet E_T	89
D.6	Integrated distribution of the τ – jet leading track p_T	89
D.7	Integrated distribution of the transverse mass of the muon and the missing E_T	90
D.8	Integrated distribution of the cosine of the azimuthal angle between the muon and the τ – jet directions.	90
D.9	Integrated distribution of the ratio of the τ – jet hadronic energy and the leading track momentum.	91
D.10	Integrated distribution of the first b tagged jet E_T	91
E.1	The signal significance as the function of the offline muon transverse momentum cut.	92
E.2	The signal significance as the function of the offline τ – jet transverse energy cut.	93
E.3	The signal significance as the function of the offline threshold for the τ – jet leading track p_T thresholds for the 1 prong events. . .	93
E.4	The signal significance as the function of the offline threshold for the τ – jet leading track p_T thresholds for the 3 prong events. . .	94
E.5	The signal significance as the function of the upper offline thresholds for the transverse energy of the muon and the missing energy system.	94
E.6	The signal significance as the function of the upper offline threshold for the $\cos(\Delta\varphi_{\vec{p}_T, \vec{E}_T^{\text{jet}}})$	95
E.7	The signal significance as the function of the lower offline threshold for the ratio of the τ – jet energy stored in the hadron calorimeter to the leading track energy.	95

E.8	The signal significance as the function of the upper offline threshold for the ratio of the τ – jet energy stored in the hadron calorimeter to the leading track energy.	96
G.1	Ratio of the selection efficiency, after the jet and missing transverse energy scale variations.	109
G.2	Ratio of the selection efficiency, after the jet and missing E_T scale variations.	110
G.3	The τ – jet E_T distribution after the τ identification cuts before and after the leading track $p_T > 40$ GeV/c selection.	110
G.4	Ratio of the selection efficiency, after jet and missing E_T scale variations for the $t\bar{t}$ events.	111
G.5	Ratio of the selection efficiency, after jet and missing E_T scale variations for the W+jet events.	112
G.6	Ratio of the selection efficiency, after jet and missing E_T scale variations for the $b\bar{b}$ events.	113
G.7	The τ -tag efficiency for the τ leptons coming from the Z bosons decay and Higgs bosons with $m_H = 200$ and 500 GeV/c ²	114

List of Tables

2.1	Contents of the chiral multiplets of the MSSM.	7
2.2	Contents of the gauge multiplets of the MSSM model.	7
3.1	Cross sections used for background processes.	18
4.1	The machine parameters relevant for the LHC detectors.	20
4.2	Comparison of vertex fitters: position estimate	30
5.1	List of generated events types.	40
5.2	Generator level preselection efficiency. Numbers in parentheses show the generated m_A	41
6.1	Summary of the selection procedure for the signal processes. . . .	53
6.2	Summary of the selection procedure for the background processes.	53
6.3	Summary of the selection procedure for the Z/γ^* background pro- cesses.	54
6.4	Summary of the selection procedure for the $b\bar{b}Z$ background pro- cesses.	54
6.5	Mass reconstruction resolution for the two Higgs boson masses. . .	58
7.1	Significance of the signal over background for 20 fb ⁻¹	64
F.1	Trigger selection efficiency for signal processes.	97
F.2	Trigger selection efficiency for signal processes.	98
F.3	Trigger selection efficiency for background processes.	98
F.4	Trigger selection efficiency for background processes.	99
F.5	Trigger selection efficiency for background processes.	99
F.6	Offline selection efficiency for the signal events.	100
F.7	Offline selection efficiency for signal events.	100
F.8	Offline selection efficiency for background events.	101
F.9	Offline selection efficiency for the background events.	101
F.10	Offline selection efficiency for the background events.	102

F.11	Offline selection efficiency for the background events.	102
G.1	Cross section of all the considered processes.	106
G.2	Number of events for 30 fb^{-1} , with low luminosity, passing each selection step.	108
G.3	Contributions to the total measured τ tag efficiency relative un- certainty.	113

Chapter 1

Introduction

The Standard Model (SM) of elementary particles describes interactions between elementary fermions: quarks and leptons. The SM is a quantum field theory with the underlying $SU(3)_C \times SU(2)_L \times U(1)_Y$ gauge symmetry [1; 2; 3]. The forces are carried by the gauge bosons: massless gluons for the strong interaction preserving the $SU(3)_C$ symmetry, massive W^\pm ($m_W = 80.4 \text{ GeV}/c^2$) and Z^0 ($m_Z = 91.2 \text{ GeV}/c^2$) bosons for the broken electroweak symmetry $SU(2)_L \times U(1)_Y$ and the massless photon for the $U(1)_{EM}$ remaining after breaking the $SU(2)_L \times U(1)_Y$ symmetry. Precise experimental tests performed in the last decades of the XX century show perfect agreement with the predictions of the SM. The only unconfirmed element of the SM is the mechanism of breaking of the electroweak (EW) symmetry group.

The most popular realisation of the EW symmetry breaking is spontaneous symmetry breaking (SSB), with the Higgs mechanism, which is realised by the vacuum expectation value (VEV) of a new field, the Higgs field. The Higgs mechanism will not be described in the detail here, since it was explained in many articles and textbooks, e.g. [4; 5]. The Higgs mechanism leads to massive Z and W bosons and the massless photon. Also fermions acquire mass by interaction with the Higgs field. In the minimal theory there is also at least one new particle – the Higgs particle which is elementary massive scalar particle. In more complicated theories there can be more Higgs fields, like in the two Higgs doublet (2HD) model, where there are 5 physical Higgs bosons: $h_{1,2,3}$, and h^\pm .

There are also other models explaining the symmetry breaking, like the technicolor, which uses dynamical symmetry breaking [6], or introducing additional, warped, spatial dimensions [7]. Although all above mentioned models explain the EW symmetry breaking they have another phenomenological problems which make them less plausible than the Higgs mechanism.

1. INTRODUCTION

Even assuming Higgs mechanism, the SM does not give answers to many important questions, which include:

- the mass hierarchy - the Higgs mechanism does not explain the mass values
- the scale of neutrinos mass [8]
- the hierarchy problem [9]
- too small CP violation for baryogenesis [10]
- no candidate for dark matter [11; 12]

The theory which solves most of the listed problems is supersymmetry (SUSY). SUSY introduces a symmetry between fermions and bosons, which leads to prediction of existence of many new particles called supersymmetric partners of the SM particles. In the minimal supersymmetric extension of the standard model (MSSM) the Higgs sector contains five physical Higgs bosons: h , H , A , H^\pm . The new, SUSY, particles were directly searched at LEP2 [13] and are searched at Tevatron [14] with negative results setting only upper limits on searched particles masses.

The Large Hadron Collider (LHC), being build at the CERN, Geneva is aimed mainly at search for the SUSY particles, in particular Higgs bosons. There will be five experiments working by the LHC accelerator: two of general purpose: A Toroidal LHC ApparatuS (ATLAS), Compact Muon Solenoid (CMS), and three dedicated experiments: A Large Ion Collider Experiment (ALICE), LHCb and Total Cross Section, Elastic Scattering and Diffraction Dissociation at the LHC (TOTEM).

This thesis describes the CMS experiment discovery potential in the specific H/A decay channel for the τ pair: one τ decaying into hadrons (latter referred as τ jet) and neutrinos, the other one into μ and neutrinos. Previously established criteria [15] have been implemented within the latest full CMS reconstruction software [16] and optimized where needed. Events were simulated with the full detector simulation [17; 18].

The thesis is organized as follows: in the Chapter 2 description of the MSSM model is presented, in the Chapter 3 the cross section predictions for the signal and background processes are described. The CMS detector and basic reconstruction algorithms are presented in the Chapter 4. In the Chapter 5 the simulation process is explained. In the Chapter 6 analysis details are presented. The analysis results and conclusions are described in Chapters 7 and 8.

In the Appendix A comparison of the kinematic variables for $b\bar{b}H$ between leading order (LO) implemented in the PYTHIA program used for the generation of the signal events and next-to-leading order (NLO) results is presented. In the Appendix B the special $b\bar{b}$ events normalisation is explained. Integrated distributions of the selection variables for all considered processes are presented in the Appendix C. In the Appendix D integrated distributions of the selection variables after each offline selection cut for the signal events with $m_A = 200 \text{ GeV}/c^2$, and $t\bar{t}$ background events are showed. The plots used for the selections thresholds optimization are presented in the Appendix E. The tables with the selection efficiencies at the trigger and offline steps are presented in the Appendix F. The study on the estimation of the τ tagging efficiency from the data for the $Z \rightarrow \tau\tau$ events is presented in the Appendix G. This study is important for the validation of the Monte Carlo (MC) procedures used for $A/H \rightarrow \tau\tau$ analysis.

The author is a member of the CMS collaboration. He is working in the Warsaw CMS Group involved in the resistive plate chamber (RPC) trigger project. Author's responsibility was implementation and maintenance of the RPC trigger simulation in the CMS reconstruction software. The author's own contribution to the thesis consists in implementation of the τ trigger based on pixel hits in the latest CMS software, analysis described in Chapter 6, preparation and partial simulation of the Monte Carlo events, described in the Chapter 5, and studies described in the Appendixes.

The contents of the Chapter 6 and Appendixes B – F were published as a CMS Note [19], the Appendix A was published as a part of the summary report of the Les Houches physics at TeV colliders 2005 workshop [20]. The Appendix G was published as a CMS Note [21].

Chapter 2

Minimal Supersymmetric Standard Model

2.1 Overview

The $SU(3)_C \times SU(2)_L \times U(1)_Y$ gauge symmetry of the SM is spontaneously broken to the $SU(3)_C \times U(1)_{EM}$ group by introducing the elementary scalar fields (the Higgs fields), which possess a non zero vacuum expectation value (VEV) v . The couplings (λ_f) of Higgs fields (H) to all the particles of the Standard Model are proportional to the mass (m_f) of the particle (f and \bar{f}). Therefore $\lambda_f f \bar{f} H$ interaction terms lead to fermions mass terms $m_f f \bar{f}$ for the Higgs field acquiring the VEV. The quantum loop corrections for any elementary scalar field in the quantum field theory are proportional to the square of the cutoff scale Λ_{UV}^2 . The Λ_{UV}^2 is usually defined as the scale up to which the model is valid. In the case of the Standard Model, the next physical scale above the electroweak scale $\sim m_Z = 91 \text{ GeV}/c^2$ is the Planck scale: $M_P = \sqrt{\hbar c / G_{Newton}} = 1.2 \times 10^{19} \text{ GeV}/c^2$. The very large ratio of the two scales is known as the “hierarchy problem”. One of its manifestations is a very large loop correction to the Higgs boson mass parameter m_H^2 . This shows that the SM is only a low energy effective model, which is valid up to the $\sim \text{TeV}$ energy scale. Above this scale a “new physics” should be introduced to avoid the hierarchy problem. One of the most theoretically successful models beyond the SM is the supersymmetry (SUSY).

Supersymmetric models possess additional, internal symmetry, which transforms the fermions into bosons and the opposite:

$$Q|fermion\rangle = |boson\rangle, \quad Q|boson\rangle = |fermion\rangle \quad (2.1)$$

where the Q is a supersymmetry transformation generator. The Q is a fermionic object, which satisfies the following commutation and anticommutation relations

with the momentum operators P^μ :

$$\{Q, Q^\dagger\} = 2\sigma_\mu P^\mu \quad (2.2)$$

$$\{Q, Q\} = \{Q^\dagger, Q^\dagger\} = 0 \quad (2.3)$$

$$[P^\mu, Q] = [P^\mu, Q^\dagger] = 0 \quad (2.4)$$

Since the Q changes the spin of the particle it generates multiplets populated by both fermions and bosons. Such a multiplet is called a *supermultiplet*. Particles which belong to one supermultiplet are called the *superpartners*. The superpartners have the same mass. The mass equality emerges from the commutation relation (Eq. 2.4). Since if the P^μ commutes with Q and Q^\dagger , also the (mass)² operator, P^2 , does.

The loop corrections to the Higgs boson mass parameter arising from loop diagrams like the one shown in Figure 2.1 lead to the corrections given by the Eq. 2.5 [22; 23].

$$\Delta m_H^2 = \frac{|\lambda_f|^2}{16\pi^2} \left[-2\Lambda_{UV}^2 + 12m_f^2 \ln \left(\frac{\Lambda_{UV}}{m_f} \right) - 4m_f^2 \right] + \mathcal{O} \left(\frac{1}{\Lambda_{UV}^2} \right) \quad (2.5)$$

In SUSY there are also contributions from the loops where the superpartner of mass m_S and coupling λ_S is exchanged (Fig. 2.2). The contribution from these diagrams is [23]:

$$\Delta m_H^2 = \frac{\lambda_S}{16\pi^2} \left[\Lambda_{UV}^2 - 2m_S^2 \ln \left(\frac{\Lambda_{UV}}{m_S} \right) \right] + \frac{\lambda_S^2}{16\pi^2} v^2 \left[1 - 2 \ln \left(\frac{\Lambda}{m_S} \right) \right] + \mathcal{O} \left(\frac{1}{\Lambda_{UV}^2} \right) \quad (2.6)$$

The two contributions cancel in the case when $|\lambda_f|^2 = \lambda_S$, $m_S = m_f$, $\lambda_S =$

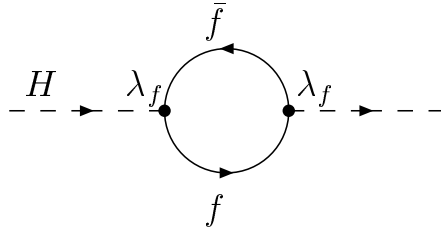


Figure 2.1: Fermion loop correction to the Higgs boson propagator.

$2m_f^2/v^2$, and if there are two scalar particles for each fermion. This is exactly the case for the SUSY with the Higgs EW breaking mechanism. In that case the couplings and masses are forced to be the same by the supersymmetry. The couplings are proportional to the particle mass due to the Higgs mechanism.

If the supersymmetry is a symmetry of nature there should exist superpartners for all known SM particles. The electron should have a bosonic partner of the

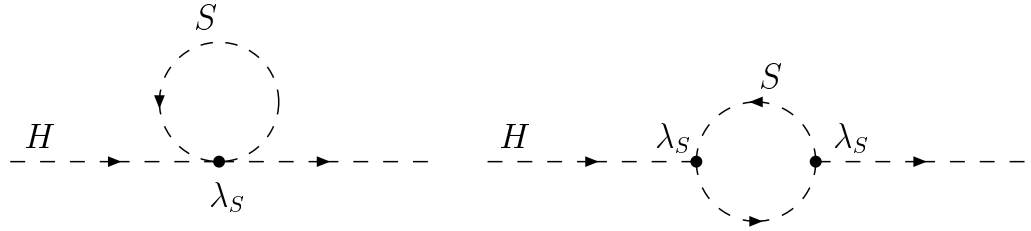


Figure 2.2: Scalar loop corrections to the Higgs boson propagator.

same mass, but with an integer spin. No such particles are known, therefore either the supersymmetry is broken, or it is not realised at all. Throughout this thesis the former scenario will be assumed. Below the particle content of the Minimal Supersymmetric extension of the Standard Model (MSSM), the Higgs mechanism in the MSSM, and the SUSY breaking are summarized.

2.2 Particle content of the MSSM

It can be easily shown, that in the supermultiplets the number of fermionic (n_F) and the bosonic (n_B) degrees of freedom are equal: $n_B = n_F$. Each Weyl fermion corresponds to two degrees of freedoms: the left and right helicity, therefore the multiplet contains two, complex, boson fields for each fermion. By the convention the bosonic partners of the left handed fermions are labeled by L, and partners of the right handed fermion are labeled by R, e.g. \tilde{e}_L, \tilde{e}_R . The multiplets containing the chiral fermions are called the chiral multiplets, the multiplets containing the gauge bosons are called the gauge multiplets. The chiral multiplets of the MSSM model are listed in Table 2.1, and the gauge multiplets are listed in Table 2.2. In the MSSM there are two, complex, Higgs fields, which are part of the Higgs chiral multiplet (see below).

2.3 Higgs sector in MSSM

The supersymmetric models require at least two complex Higgs doublets. This requirement arises from the conditions for the gauge anomalies cancellation. The sum of the third powers of the hypercharge for all the Weyl fields must vanish: $Tr[Y^3] = 0$. This condition is satisfied for Standard Model particles, therefore is also valid for their superpartners. The fermionic partners of the gauge bosons have 0 hypercharge (Tab. 2.2). The Higgs doublet must be a weak isodoublet with $Y = \pm 1/2$ (Tab. 2.1) and the fermionic Higgs partners, the Higgsinos, have the same hypercharges. To keep the $Tr[Y^3] = 0$ one has to have two Higgs fields

Table 2.1: Contents of the chiral multiplets of the MSSM. Only one generation for the leptons and quarks is shown. Transformation properties under all gauge groups of the SM are presented. The weak hypercharge is expressed in the normalisation, where $Q_{EM} = T_3 + Y$. All chiral fields are presented as a left handed Weyl fermions [24].

Names		spin 0	spin 1/2	charge SU(3) _C , SU(2) _L , U _Y
squarks, quarks ($\times 3$ families)	Q	$(\tilde{u}_L \tilde{d}_L)$	$(u_L d_L)$	$(3, 2, \frac{1}{6})$
	\bar{u}	\tilde{u}_R^*	u_R^\dagger	$(\bar{3}, 1, -\frac{2}{3})$
	\bar{d}	\tilde{d}_R^*	d_R^\dagger	$(\bar{3}, 1, \frac{1}{3})$
sleptons, leptons ($\times 3$ families)	L	$(\tilde{\nu} \tilde{e}_L)$	(νe_L)	$(1, 2, -\frac{1}{2})$
	\bar{e}	\tilde{e}_R^*	e_R^\dagger	$(1, 1, 1)$
Higgs, higgsinos	H_u	$(H_u^+ H_u^0)$	$(\tilde{H}_u^+ \tilde{H}_u^0)$	$(1, 2, +\frac{1}{2})$
	H_d	$(H_d^0 H_d^+)$	$(\tilde{H}_d^0 \tilde{H}_d^-)$	$(1, 2, -\frac{1}{2})$

Table 2.2: Contents of the gauge multiplets of the MSSM model [24].

Names	spin 1/2	spin 1	charge SU(3) _C , SU(2) _L , U _Y
gluino, gluon	\tilde{g}	g	$(8, 1, 0)$
winos, W bosons	$\tilde{W}^\pm, \tilde{W}^0$	W^\pm, W^0	$(1, 3, 0)$
bino, B boson	\tilde{B}^0	B^0	$(1, 1, 0)$

with opposite hypercharges. The two Higgs fields are denoted by H_u – the field coupling exclusively to the up-type fermions and H_d – the field coupling only to the down-type fermions. After the minimization of the Higgs potential the two Higgs fields acquire the vacuum expectation values:

$$\langle H_d \rangle = \frac{1}{\sqrt{2}} \begin{pmatrix} v_d \\ 0 \end{pmatrix}, \quad \langle H_u \rangle = \frac{1}{\sqrt{2}} \begin{pmatrix} 0 \\ v_u \end{pmatrix} \quad (2.7)$$

The v_u and v_d are vacuum expectations values, with the chosen normalization $v = v_u^2 + v_d^2 = 4m_W^2/g^2 = (246 \text{ GeV}/c^2)^2$.

The interaction basis needs to be rotated to diagonalize the mass matrix of the Higgs fields. After the rotation, one obtains five physical Higgs bosons out of total $2 \times 4 = 8$ degrees of freedom for two complex doublet fields (the remaining three degrees of freedom are the Goldstone bosons absorbed as the longitudinal components of the massive gauge bosons W^\pm and Z^0):

2. MINIMAL SUPERSYMMETRIC STANDARD MODEL

- two charged Higgs bosons:

$$H^\pm = H_d^\pm \sin(\beta) + H_u^\pm \cos(\beta) \quad (2.8)$$

- one CP-odd Higgs boson:

$$A = \sqrt{2}[Im(H_d^0) \sin(\beta) + Im(H_u^0) \cos(\beta)] \quad (2.9)$$

- and two CP-even Higgs bosons, with the lighter denoted by h:

$$\begin{aligned} h &= -[\sqrt{2} \cdot Re(H_d^0) - v_d] \sin(\alpha) + [\sqrt{2} \cdot Re(H_u^0) - v_u] \cos(\alpha), \\ H &= [\sqrt{2} \cdot Re(H_d^0) - v_d] \cos(\alpha) + [\sqrt{2} \cdot Re(H_u^0) - v_u] \sin(\alpha) \end{aligned} \quad (2.10)$$

The $\sin(\alpha)$ is the sine of the diagonalisation angle for the mass matrix for the neutral, CP-even Higgs bosons. The $\tan(\beta)$ is defined as the ratio of the expectation values of two Higgs fields: $\tan(\beta) = \frac{v_u}{v_d}$.

Due to the supersymmetric constraints, the self interaction of the Higgs particles are expressed in terms of the gauge couplings. Therefore at the tree level, the Higgs sector can be described by two parameters only. Usually, the $\tan(\beta)$ and the m_A are chosen. All other masses and couplings are functions of these two parameters, in particular the masses of other Higgs bosons can be expressed as:

$$m_{H^\pm}^2 = m_A^2 + m_W^2 \quad (2.11)$$

$$m_{H,h}^2 = \frac{1}{2}(m_A^2 + m_Z^2 \pm \sqrt{(m_A^2 + m_Z^2)^2 - 4m_Z^2 m_A^2 \cos^2(2\beta)}) \quad (2.12)$$

In the limit of large CP-odd Higgs boson $m_A \gg m_Z$ the expressions for the masses simplify to:

$$m_h^2 = m_Z^2 \cos^2(2\beta) \quad (2.13)$$

$$m_H^2 = m_A^2 + m_Z^2 \sin^2(2\beta) \quad (2.14)$$

It is important to stress that only at the tree level the light Higgs boson mass is bounded by the Z mass (Eq. 2.13). There are relatively large radiative corrections from top and stop loops, which move this mass to the level of ~ 130 GeV/c² [5]. The masses squared of the heavy neutral Higgs bosons A and H differ by a factor of order of $[\frac{m_Z}{m_A} \cdot \sin(2\beta)]^2$ (Eq. 2.14), which is only $1.5 \cdot 10^{-2}$ for $m_A = 150$ GeV/c², and $\tan(\beta) = 10$. This makes the two Higgs bosons almost degenerate in mass.

The couplings of the neutral Higgs bosons to the down-type fermions, relative to the SM Higgs boson coupling, $g_{SM} = g_{\frac{m_f}{2m_W}}$, can be expressed as [5]:

$$hb\bar{b} \text{ (or } h\tau^+\tau^-) : -\frac{\sin\alpha}{\cos\beta} = \sin(\beta - \alpha) - \tan\beta \cdot \cos(\beta - \alpha) \quad (2.15)$$

$$Hb\bar{b} \text{ (or } H\tau^+\tau^-) : \frac{\cos\alpha}{\cos\beta} = \cos(\beta - \alpha) + \tan\beta \cdot \sin(\beta - \alpha) \quad (2.16)$$

$$Ab\bar{b} \text{ (or } A\tau^+\tau^-) : \gamma_5 \tan\beta \quad (2.17)$$

The couplings to the up-type fermions are:

$$ht\bar{t} : -\frac{\cos\alpha}{\sin\beta} = \sin(\beta - \alpha) + \cot\beta \cdot \cos(\beta - \alpha) \quad (2.18)$$

$$Ht\bar{t} : \frac{\sin\alpha}{\sin\beta} = \cos(\beta - \alpha) - \cot\beta \cdot \sin(\beta - \alpha) \quad (2.19)$$

$$At\bar{t} : \gamma_5 \cot\beta \quad (2.20)$$

Figure 2.3 shows the $\cos^2(\beta - \alpha)$ as a function of the m_A for relatively large $\tan(\beta) = 30$. The $\cos^2(\beta - \alpha)$ is less than 10^{-2} , for $m_A \geq 150$ GeV/c², therefore $\sin(\beta - \alpha)$ becomes of order of 1, and the couplings can be simplified to the form of:

$$hb\bar{b} \text{ (or } h\tau^+\tau^-) \simeq \sin(\beta - \alpha) \simeq 1 \quad (2.21)$$

$$Hb\bar{b} \text{ (or } H\tau^+\tau^-) \simeq \tan\beta \cdot \sin(\beta - \alpha) \simeq \tan\beta \quad (2.22)$$

$$ht\bar{t} \simeq \sin(\beta - \alpha) \simeq 1 \quad (2.23)$$

$$Ht\bar{t} \simeq \cot\beta \cdot \sin(\beta - \alpha) \simeq \cot\beta \quad (2.24)$$

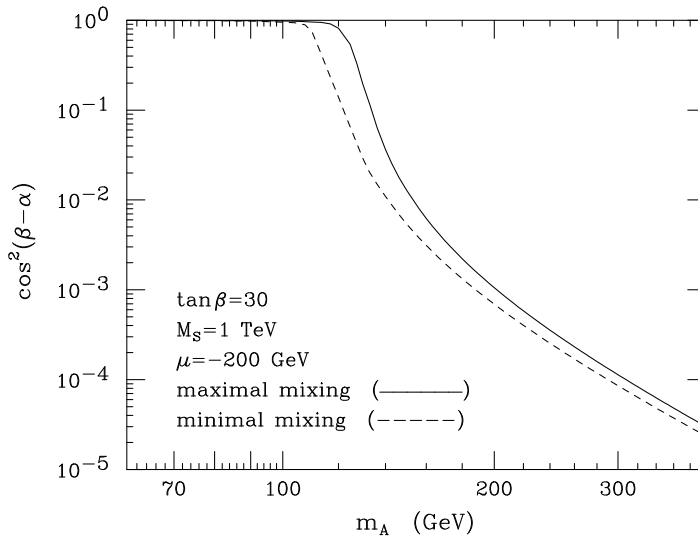


Figure 2.3: The $\cos^2(\beta - \alpha)$ as a function of the m_A , for the $\tan(\beta) = 30$.

The couplings of the lighter, neutral, Higgs boson are almost the same as the couplings of the SM Higgs boson for $\tan(\beta) \geq 10$, and $m_A \geq 150 \text{ GeV}/c^2$ (the “decoupling limit”).

The couplings of the heavy neutral Higgs bosons to b quarks and τ leptons are enhanced with large $\tan(\beta)$, which makes the associated $b\bar{b}H/A$ production, with subsequent decay to τ lepton pair, a possibly promising discovery channel. More detailed discussion of the production cross section will be done in Chapter 3.

2.4 Supersymmetry breaking

Negative result of the current search for the supersymmetric partners of ordinary particles, prove that the supersymmetry is broken, or is not realized in nature. Adding supersymmetry breaking terms to the lagrangian will lead in particular to the mass difference of the particles belonging to the same supermultiplet. Therefore, the superpartners of know particles can be made heavy enough to escape direct and indirect search in current energy and precision range.

Breaking of the supersymmetry can lead to differences of the masses and couplings of scalar and fermion members of multiplets. The difference in couplings will lead to large, quadratic, corrections to the Higgs mass (Eq. 2.25),

$$\Delta m_H^2 = \frac{1}{8\pi^2}(\lambda_S - |\lambda_f|^2)[\Lambda_{UV}^2 + \dots] \quad (2.25)$$

which will lead to the hierarchy problem. In the case when the couplings remain the same, but masses differ, only logarithmic corrections remain (Eq. 2.26).

$$\Delta m_H^2 = m_{soft}^2 \left[\frac{1}{16\pi^2} \ln(\Lambda_{UV}/m_{soft}) + \dots \right] \quad (2.26)$$

The m_{soft} determines the mass splitting between scalar and fermionic partners induced by additional, supersymmetry breaking, terms in lagrangian. The latter pattern of the supersymmetry breaking is called a “soft” breaking. It can be achieved by adding SUSY breaking terms to SUSY preserving lagrangian (Eq. 2.27).

$$\mathcal{L} = \mathcal{L}_{SUSY} + \mathcal{L}_{soft} \quad (2.27)$$

The \mathcal{L}_{soft} part can only contain mass terms and couplings with positive mass dimension (Eq. 2.28).

$$\mathcal{L}_{soft} = -\frac{1}{2}(M_a \lambda^a \lambda^a + c.c.) - (m^2)_j^i \phi_j^* \phi_i - \left(\frac{1}{2} b^{ij} \phi_i \phi_j + \frac{1}{6} a^{ijk} \phi_i \phi_j \phi_k + c.c. \right) \quad (2.28)$$

The M_a are \tilde{g} , \tilde{W} and \tilde{B} gaugino masses, $(m^2)_j^i$ and b^{ij} are the squares of the scalars masses and a^{ijk} are trilinear scalar couplings. Since all the parameters are

complex, and in general not related to known parameters of the SM, $\mathcal{L}_{\text{soft}}$ part of the MSSM lagrangian introduces over 100 new parameters.

To include precise experimental constraints, in particular amount of the CP violation [25], and large flavor changing neutral currents (FCNC) [26; 27] a number of assumptions are done for the parameters of the $\mathcal{L}_{\text{soft}}$. Usually it is assumed that [28]:

- squark and slepton mass matrices are flavor-blind, this is are proportional to unit 3×3 matrix in the flavour space, e.g. $\mathbf{m}_{\mathbf{Q}}^2 = m_Q^2 \cdot \mathbf{1}_{3 \times 3}$;
- scalar trilinear couplings, are proportional to Yukawa matrices of the SM, e.g.: $\mathbf{a}_{\mathbf{u}} = A_u \cdot \mathbf{y}_{\mathbf{u}}$, where $\mathbf{a}_{\mathbf{u}}$ is coupling matrix in term $\tilde{u}\mathbf{a}_{\mathbf{u}}\tilde{Q}H_u$, and \mathbf{y}_u is Yukawa matrix for the up-type quarks;
- it is assumed that masses of the gauginos, and A_i parameters are either real or pure imaginary.

There is a number of specific supersymmetry breaking scenarios. The most popular are the gauge (GMSB) [29; 30], and gravity mediated [31; 32] supersymmetry breaking. Most of the supersymmetry breaking scenarios lead to the similar parameters pattern, as described above. Although the mechanism of the supersymmetry breaking is important, the specific MSSM parameter set can be used without specifying the supersymmetry breaking scenario.

In this thesis, a parameter set, the so called “max m_h scenario” [33], leading to the conservative bounds on the $\tan(\beta)$ for given values of the top quark mass and the mass scale of supersymmetric particles was used [34; 35]. The “max m_h scenario” was used for the exclusion limits for the MSSM Higgs boson searches at LEP [1; 36], and Tevatron [37; 38]. The parameters of the “max m_h scenario” are reported below:

$$m_t = 175 \text{ GeV}/c^2 \quad (2.29)$$

$$M_{SUSY} = 1000 \text{ GeV}/c^2 \quad (2.30)$$

$$\mu = 200 \text{ GeV}/c^2 \quad (2.31)$$

$$M_1 = \frac{5 \sin^2(\theta_W)}{3 \cos^2(\theta_W)} M_2 \quad (2.32)$$

$$M_2 = 200 \text{ GeV}/c^2 \quad (2.33)$$

$$M_{\tilde{g}} = 800 \text{ GeV}/c^2 \quad (2.34)$$

$$X_t^{OS}(= A_t - \mu \cot(\beta)) = 2000 \text{ GeV}/c^2 \quad (2.35)$$

$$A_b = A_t \quad (2.36)$$

In this scenario, all soft supersymmetry breaking scalar masses are equal to M_{SUSY} . The masses of the SU(2) gauginos are set by M_2 , gluino masses are set by $M_{\tilde{g}}$, and the SU(1) gaugino masses, M_1 , are set by the Grand Unification Theory (GUT) relation, Eq. 2.32 [28]. The scalar trilinear couplings of stop and sbottom squarks are set by requiring that $X_t^{OS}(= A_t - \mu \cot(\beta)) = 2 \cdot M_{SUSY}$. For this special value of the X_t parameter the mass of the lightest, neutral, scalar Higgs boson h is maximized when the other SUSY parameters fixed. There are two remaining free parameters describing the Higgs sector: the pseudoscalar mass m_A , and $\tan(\beta)$. The final discovery reach will be plotted as a function of these two parameters in Chapter 7.

The dominant SUSY loop corrections to the Higgs bosons couplings to down-type leptons are sensitive to the Higgsino mass parameter μ [35]. These corrections affect the associated production $gg \rightarrow b\bar{b}H$ cross section, and the decay $H \rightarrow \tau\tau$ width. The corrections become large for large $\tan(\beta)$ and $|\mu|$. The discovery reach will be plotted for several, representative, values of the μ parameter.

Chapter 3

Cross sections predictions

3.1 Signal cross section calculations

In this thesis the $H/A \rightarrow \mu + \text{hadrons} + X$ process is analyzed. The hadrons coming from the τ decay will be denoted here as τ jet. Due to the small H-A bosons mass difference, the contributions from the two Higgs bosons are added. Higgs boson production from gluon and quark annihilation, both with (Fig. 3.1) and without (Fig. 3.2) associated b quark pair have been considered. The main contribution comes from the $gg \rightarrow b\bar{b}H/A$ process. The contribution from the $q\bar{q} \rightarrow b\bar{b}H/A$ is negligible: $\frac{\sigma(gg \rightarrow b\bar{b}H)}{\sigma(q\bar{q} \rightarrow b\bar{b}H)} \sim 10^{-4}$. For large $\tan(\beta)$ the cross section for $gg \rightarrow H$ is a few times smaller than $\sigma(gg \rightarrow b\bar{b}H)$. Also the events produced without the b quark pair are rejected by the single b tag requirement.

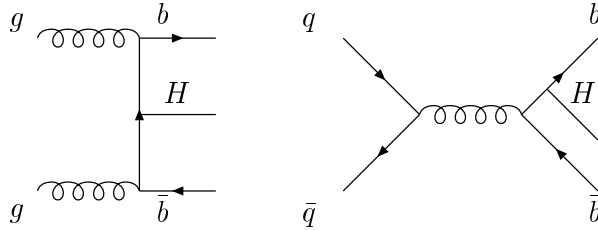


Figure 3.1: Example of the leading order diagrams for the $gg \rightarrow b\bar{b}H$ (left) and $q\bar{q} \rightarrow b\bar{b}H$ (right) Higgs boson production.

Signal cross sections has been computed using the FeynHiggs 2.3.1 program [39]. The FeynHiggs program calculates the masses and branching ratios of the MSSM Higgs bosons with corrections up to the dominant two loops corrections [40]. The program also calculates the production cross sections by scaling the NLO cross section for the Standard Model Higgs boson by appropriate factors coming from ratio of the SM and MSSM Higgs bosons couplings. The HDECAY [41] program with the C++ interface SigmaBr6 [42] was used for the qualitative predictions

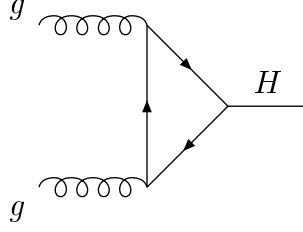


Figure 3.2: Example of the leading order diagram for the $gg \rightarrow H$ Higgs boson production.

shown in Figures 3.7 and 3.5. The differences between the FeynHiggs and the HDECAY are of the order of 10%.

Figure 3.3 shows the cross section for both H and A bosons as function of m_A . The H and A production have almost the same cross sections for $m_A \gg m_Z$. Also the masses become more degenerate, therefore the two particles are indistinguishable in the detector when their CP is not measured. The cross section times $\text{BR}(A/H \rightarrow \tau\tau)$ as a function of $\tan(\beta)$ grows as $\tan^2(\beta)$ (Fig. 3.4), which results from the $b\bar{b}H/A$ coupling being proportional to $\tan(\beta)$.

The width of the Higgs particles is small compared to its mass. It is of the order of $1 \text{ GeV}/c^2$ for $m_A = 200 \text{ GeV}/c^2$, and slowly increases with m_A to $10 \text{ GeV}/c^2$ for $m_A = 700 \text{ GeV}/c^2$ (Fig. 3.5). As a function of $\tan(\beta)$ the width grows proportional to $\tan^2(\beta)$. It changes from $1.4 \text{ GeV}/c^2$ for $\tan(\beta) = 20$ to $14 \text{ GeV}/c^2$ for $\tan(\beta) = 70$ (Fig. 3.6) for $m_A = 200 \text{ GeV}/c^2$.

The $\text{BR}(H/A \rightarrow \tau\tau)$ is of order of 10% for $m_A \geq 150 \text{ GeV}/c^2$, $\tan(\beta) = 20$, and slowly decreases for larger values of m_A to $\sim 8\%$ for $m_A \sim 500 \text{ GeV}/c^2$ (Fig. 3.7). Since the $\tau\tau H/A$ coupling is proportional to $\tan(\beta)$, the $\text{BR}(H/A \rightarrow \tau\tau)$ increases with $\tan(\beta)$ (Fig. 3.8).

With a $\text{BR}(\tau\tau \rightarrow \mu + X) = 0.22$ [43], the total branching ratio is $\text{BR}(H/A \rightarrow \tau\tau \rightarrow \mu + \tau \text{ jet} + X) \simeq 0.02$.

3.2 Background cross section calculations

Processes leading to a hard isolated muon and a hard jet have been selected as a possible backgrounds. In most of the processes, the leptonic decays of W bosons are the source of isolated muons. The list of analyzed backgrounds includes:

1. top quark pair production: $t\bar{t}$;
2. QCD multi-jet production (minimum bias) estimated by $b\bar{b}$ events;

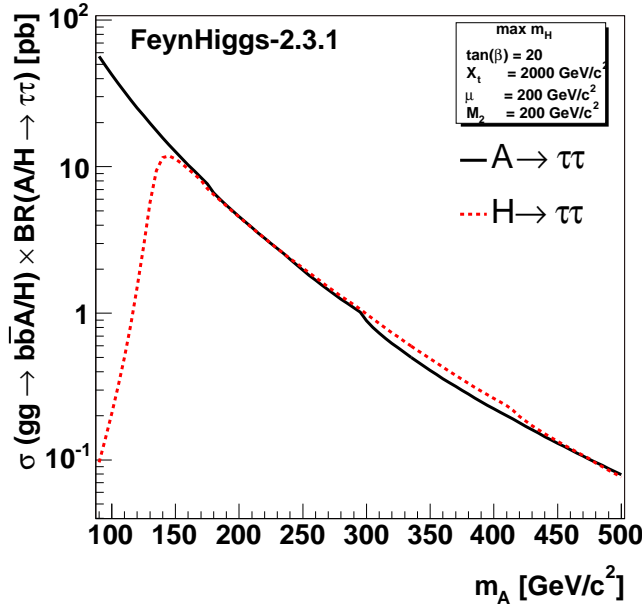


Figure 3.3: Cross section times $\text{BR}(A/H \rightarrow \tau\tau)$ for associated $b\bar{b}H/A$ production via gluon fusion as a function of m_A for $\tan(\beta) = 20$.

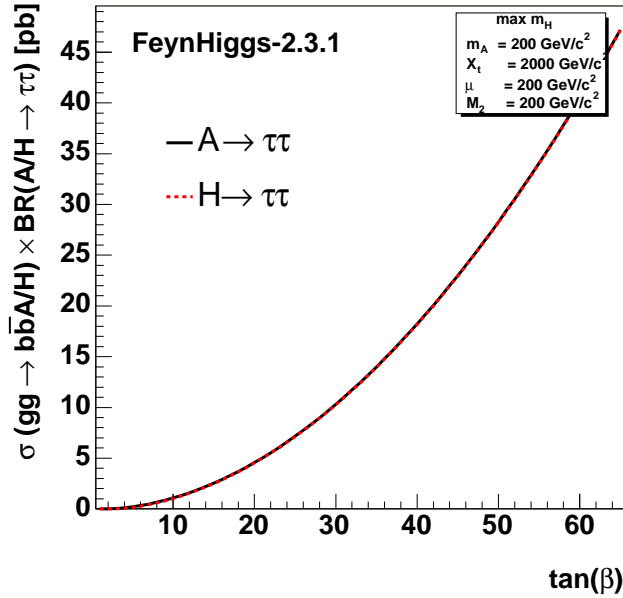


Figure 3.4: Cross section times $\text{BR}(A/H \rightarrow \tau\tau)$ for associated $b\bar{b}H/A$ production via gluon fusion as a function of $\tan(\beta)$, for $m_A = 200 \text{ GeV}/c^2$. Curves for A and H bosons overlap.

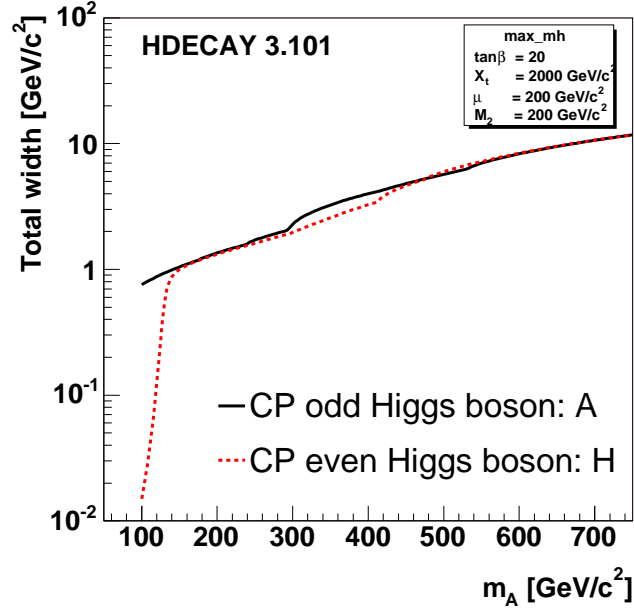


Figure 3.5: The decay widths of the Higgs bosons A and H as a function of m_A for $\tan(\beta) = 20$.

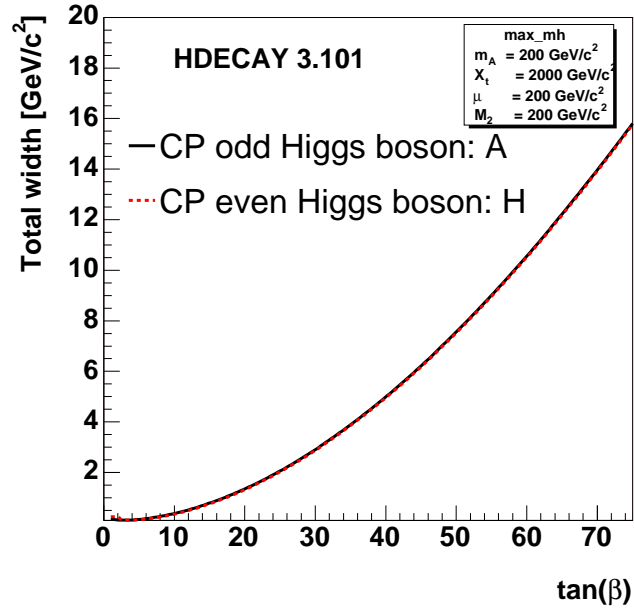


Figure 3.6: The decay widths of the Higgs bosons A and H as a function of $\tan(\beta)$ for $m_A = 200 \text{ GeV}/c^2$. Curves for A and H bosons overlap.

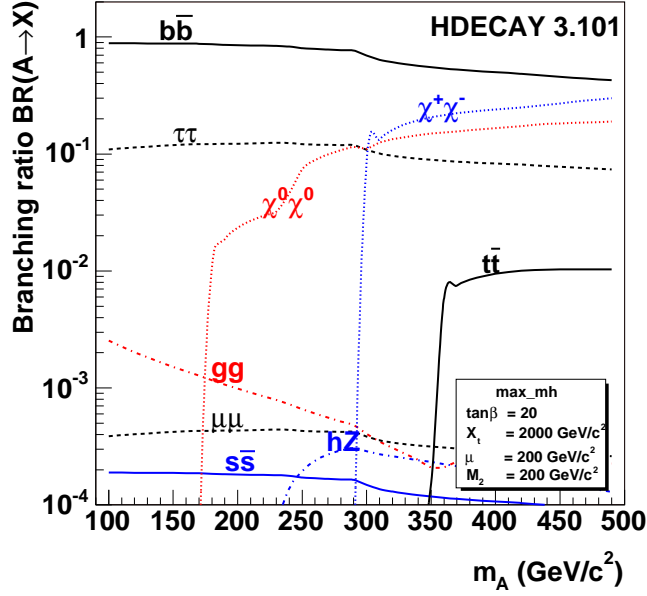


Figure 3.7: Pseudoscalar Higgs boson branching ratios as a function of m_A for $\tan(\beta) = 20$.

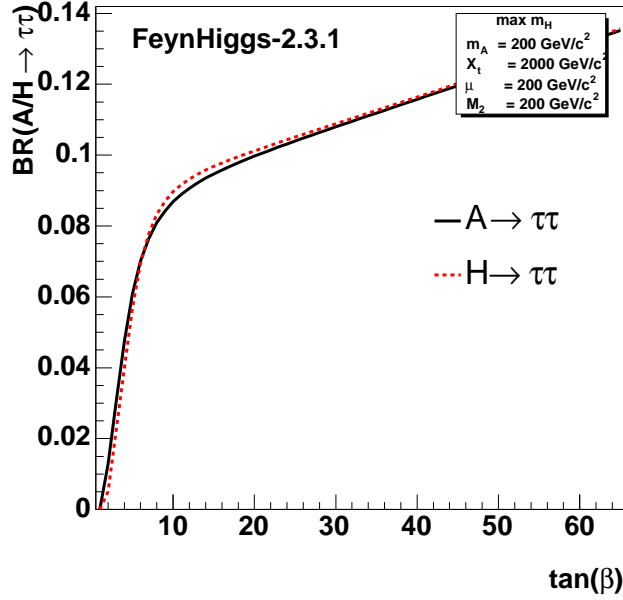


Figure 3.8: Higgs boson branching ratio into $\tau\tau$ as a function of $\tan(\beta)$ for $m_A = 200 \text{ GeV}/c^2$.

3. CROSS SECTIONS PREDICTIONS

3. W boson accompanied by a t quark: Wt ;
4. W boson accompanied by a light quark or gluon jet: Wj ;
5. the $(b\bar{b})Z/\gamma^*$ production with the Z/γ^* decaying the same way as the Higgs particles.

Cross sections used for the backgrounds considered are reported in Table 3.1.

Only the decay into $\tau\tau \rightarrow \mu + \tau \text{ jet} + X$ has been considered for the Z/γ^* background. The relevant branching ratio $\text{BR}(Z/\gamma^* \rightarrow \tau\tau \rightarrow \mu + X) = 0.0337 \cdot 0.22 = 0.007$ was included in the cross section. The decay into $\tau\tau$ without forcing any specific τ decay. was considered for the $b\bar{b}Z/\gamma^*$ background No specific decay path was required for other background processes.

The Wj process was generated with the PYTHIA [44] processes $f + \bar{f}' \rightarrow g + W^\pm$ and $f + g \rightarrow f' + W^\pm$. Those processes give one or two, in the case of gluon splitting, jets in the final state. Also there can be additional jets coming from the initial or final state radiation (Chapter 5).

The theoretical calculations involving higher orders were used for the processes 1, 2, 3 and 5. The CompHep [45] program was used for the $b\bar{b}Z/\gamma^*$ process. The program calculates cross sections from the LO matrix element, and provides the events at the parton level, which are then hadronized with PYTHIA [44]. The $(b\bar{b})Z/\gamma^*$ processes were considered in $\tau\tau$ mass bins, described in the Table 3.1.

Table 3.1: Cross sections used for background processes.

Process	PYTHIA 6.233 [pb]	Calculations		
		Source	[pb]	K factor
$b\bar{b}$	$4.78 \cdot 10^8$	[46]	$5 \cdot 10^8$	1.05
$t\bar{t}$	490	[47]	840	1.79
$gb \rightarrow Wt$	281	[48]	62	n.a.
Wj	$4.15 \cdot 10^4$	—	—	—
$Z/\gamma^* \rightarrow \tau\tau \rightarrow \mu + \tau \text{ jet}$ $40 < m_{\tau\tau} < 120 \text{ GeV}/c^2$	390	[49]	463	1.2
$Z/\gamma^* \rightarrow \tau\tau \rightarrow \mu + \tau \text{ jet}$ $m_{\tau\tau} > 120 \text{ GeV}/c^2$	4.14	[49]	4.88	1.18
$b\bar{b}Z/\gamma^* \rightarrow \tau\tau$ $60 < m_{\tau\tau} < 100 \text{ GeV}/c^2$	—	[45]	26.13	—
$b\bar{b}Z/\gamma^* \rightarrow \tau\tau$ $m_{\tau\tau} > 100 \text{ GeV}/c^2$	—	[45]	1.05	—

The decays of the supersymmetric particles can be potentially large source of the background. The SUSY background has been estimated using the events

for the LM2 mSUGRA CMS test point, which corresponds to the Post-WMAP benchmark point I' of [50]. At this point $\text{BR}(\tilde{\chi}_2^0 \rightarrow \tilde{\tau}_1 \tau) = 96\%$, and $\text{BR}(\tilde{\chi}_1^\pm \rightarrow \tilde{\tau}_1 \nu) = 95\%$ which makes the $\tilde{\tau}$ and τ production rate potentially dangerous. The total NLO SUSY cross section at this point is 9.4 [pb] [51]. The number of events passing all selection criteria has been estimated to be less than one, therefore the SUSY background has been considered negligible, and was not studied in detail.

Chapter 4

CMS experiment

4.1 Introduction

The Compact Muon Solenoid (CMS) detector is one of the two general purpose detectors at the Large Hadron Collider (LHC) being build at CERN, Geneva. The LHC will be a proton-proton and heavy ion collider. Proton collision will occur with the CM energy of 14 TeV, and with design luminosity of $10^{34} \text{ cm}^{-2}\text{s}^{-1}$. Basic parameters of the LHC machine are reported in Table 4.1. The design luminosity is called “high luminosity” opposite to “low luminosity”, $\mathcal{L} = 2 \cdot 10^{33} \text{ cm}^{-2}\text{s}^{-1}$, which is expected for the first years of running. With the total p-p cross section of order of 10^2 mb , at each beam crossing there will be on average a few p-p interactions for the low luminosity and 25 for the high luminosity. This effect, called the “pile-up”, has important consequences for Data Acquisition (DAQ) and the reconstruction of physics objects. The CMS is aimed to discover the “new

Table 4.1: The machine parameters relevant for the LHC detectors for the proton-proton (p-p) and heavy ions (HI) runs [52].

		p-p	HI	
Energy at collision	E	7	2.56	TeV
Dipole field at 7 TeV	B	8.33	8.33	T
Design Luminosity	L	10^{34}	10^{27}	$\text{cm}^{-2} \text{ s}^{-1}$
Bunch separation		25	100	ns
No. of bunches	k_B	2835	608	
No. particles per bunch	N_p	1.1	0.35	10^{11}
Luminosity lifetime	τ_L	10	10	hr
Number of evts/crossing	n_c	25	–	

physics”. Its main advantage is a large solenoid, generating magnetic field of 4 T, which guarantees high momentum resolution. The magnetic field is enclosed in

the iron return yoke equipped with muon detectors. As most of the modern, large scale particle detectors, CMS is composed of layers of detectors starting from the innermost tracking detectors, then calorimetry and the outermost muon system (Fig. 4.1). The CMS detector can be divided into three parts: the barrel part, covering the central region of the detector, up to $|\eta| \sim 1$, and the endcap disks located at two sides of the central barrel. In this thesis, the R, η, φ coordinate system will be used. The η is defined as the pseudorapidity: $\eta = -\ln(\tan(\frac{\theta}{2}))$, θ being the polar angle, and φ is the azimuthal angle. The $\theta = 0$ direction is parallel to the beam pipe, and the $\varphi = 0$ vector points to the inside of the LHC ring. The beginning of the coordinate system is placed at the center of the detector.

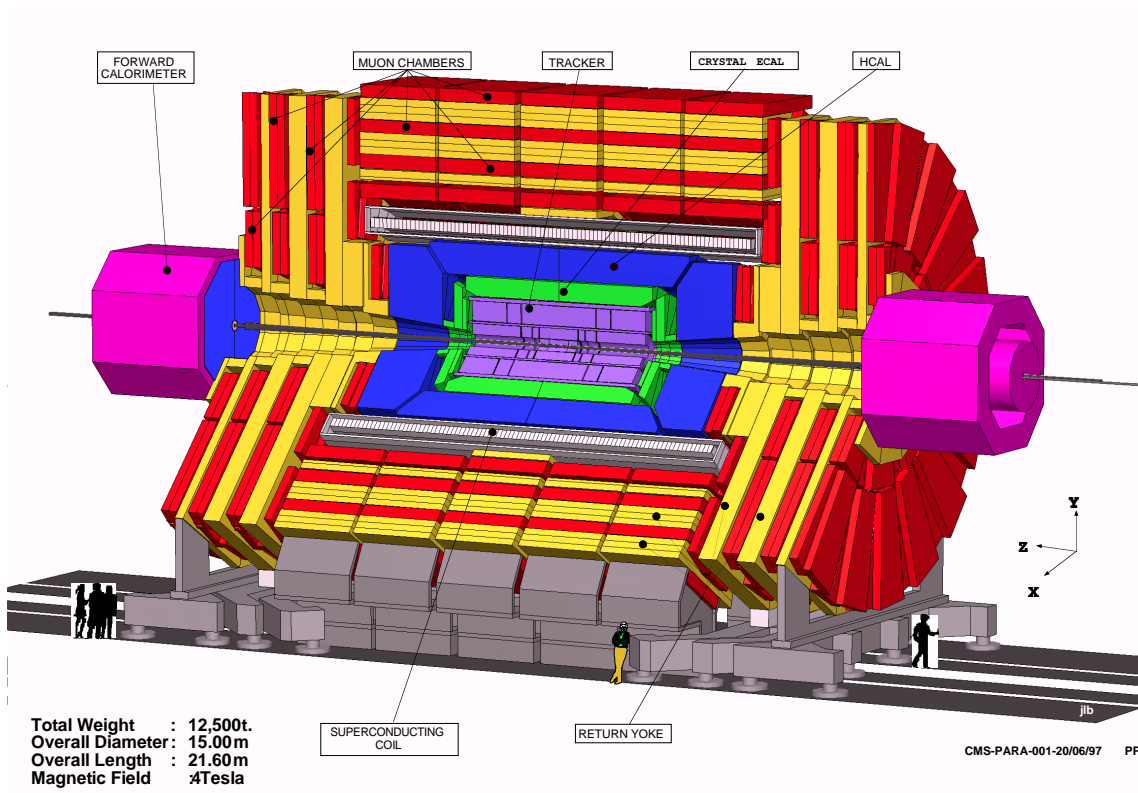


Figure 4.1: The CMS detector [52].

4.2 Detector

4.2.1 Tracking detectors

The inner most system of the CMS detector is the silicon tracking system composed of two parts: the inner pixel detectors and the outer strip detectors. The

4. CMS EXPERIMENT

layout of the tracking system is shown in Figure 4.2. The system covers full 2π in the azimuthal direction and ± 2.5 in the η direction. In the radial direction, tracker spans radii from 4 to 110 cm from the beam pipe center.

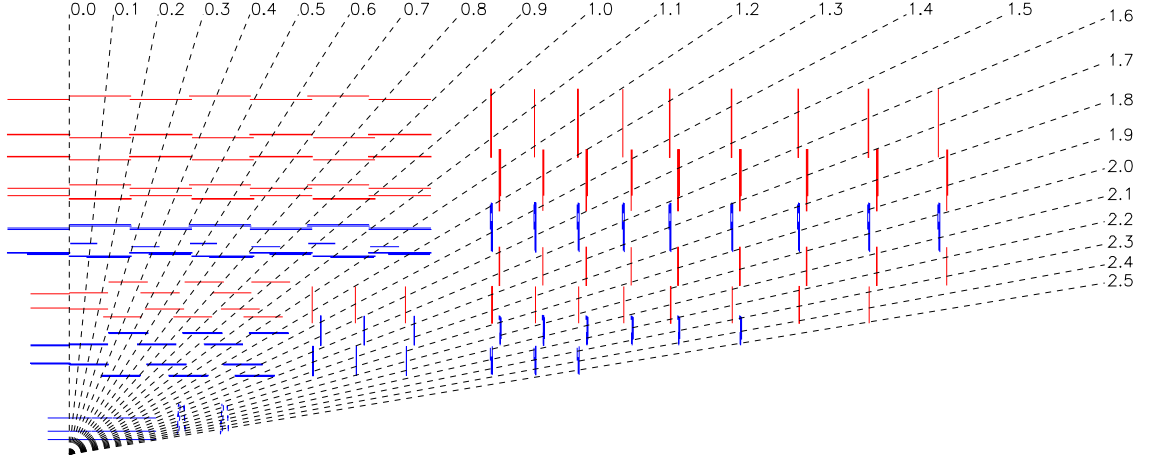


Figure 4.2: View of the CMS tracking system. The pixel and the micro-strip trackers are shown. The η coordinates are labeled. [52].

4.2.1.1 Pixel detectors

The pixel detectors are arranged in three layers in the barrel region, placed at radial distance of 4.4, 7.3 and 10.2 cm from the designed beam position. The layers span ± 26.5 cm in the z direction. In the each endcap there are two disks of inner radius of 6 cm and outer radius of 15 cm. The disks are located at the distance of 34.5 and 46.5 cm from the center of the detector (Fig. 4.2). The silicon pixel tracker covers area of 1 m^2 and the total number of pixels is 66 millions.

The pixel size is $100 \times 150 \text{ } \mu\text{m}^2$. Large magnetic field of 4 T leads to large Lorentz angle ¹ (32°) which induces significant charge share between pixels. In the endcaps the sensors are tilted by 20° around the radial direction to increase the Lorentz $\vec{E} \times \vec{B}$ force. Due to the the charge sharing between pixels the hit position resolution is smaller than the pixel size. The resolution is $10 \text{ } \mu\text{m}$ in the R - φ plane, and $20 \text{ } \mu\text{m}$ in the z direction.

4.2.1.2 Silicon detectors

Silicon strip detectors are arranged in eleven cylindrical layers in the barrel region and twelve disks in the endcaps. The innermost barrel layer is placed at

¹The Lorentz angle is the angle under which charge carriers are deflected in a magnetic field perpendicular to the electric field.

20 cm, and the outermost layer is placed at 110 cm from the beam position. The innermost endcap disk is placed at 120 cm position in the z direction, the outermost disk is placed at 280 cm (Fig. 4.2). The silicon strip pitch varies from 81 to $183\ \mu\text{m}$. The single hit position resolution varies from the $23\text{--}34\ \mu\text{m}$ in the $R\text{--}\varphi$ plane and $230\ \mu\text{m}$ in the z direction for the inner part of the strip tracker, and $35\text{--}52\ \mu\text{m}$ in the $R\text{--}\varphi$ plane and $530\ \mu\text{m}$ in the z direction for the outer part. The silicon strip tracker covers area of $220\ \text{m}^2$, the total number of strips is 9.6 million.

4.2.2 Calorimetry

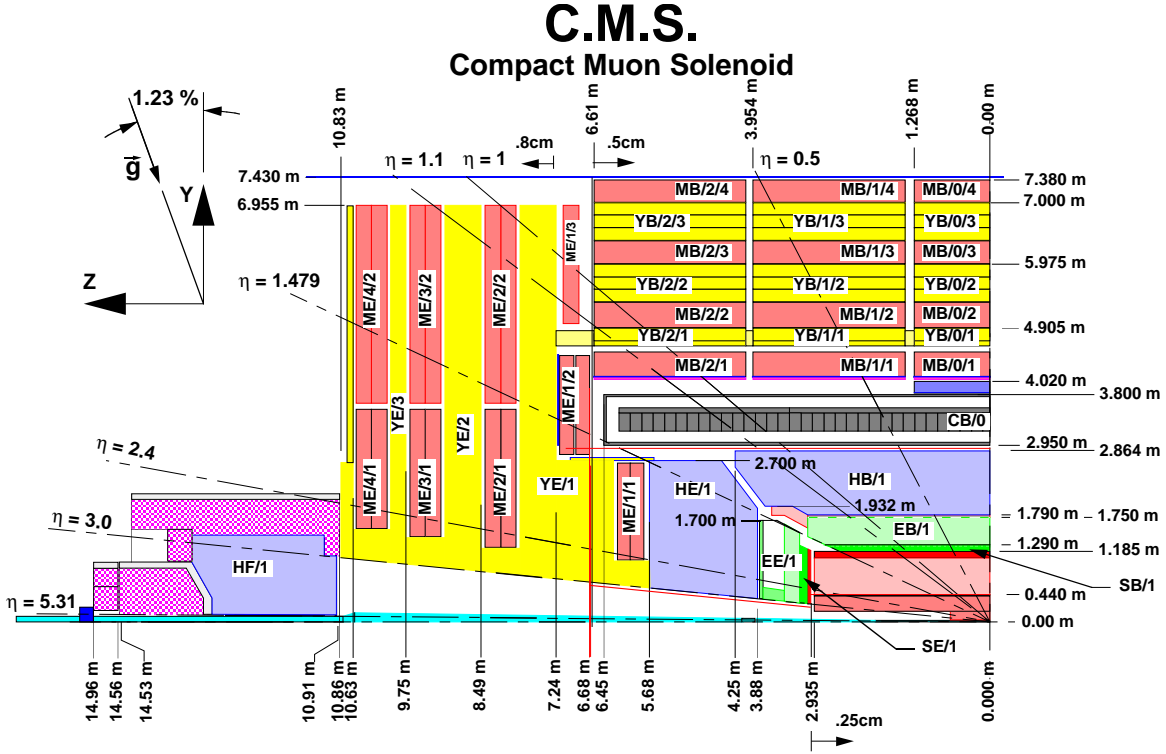


Figure 4.3: Longitudinal view of one quadrant of the CMS detector. The ECAL parts are marked EB and EE. The HCAL parts are marked HB, HE and HF. The superconducting coil is marked CB. The muon chambers are marked MB and ME. The magnet return yoke is marked YB and YE.

The CMS is equipped with the almost hermetic calorimetry system for the precise measurement of the energy of particles and jets as well as the measurement of the total transverse energy. The calorimetric system is composed of two parts: the electromagnetic and the hadronic calorimeters.

4.2.2.1 Electromagnetic calorimeter

The CMS electromagnetic calorimeter (ECAL) is build from 64200 lead tungstate (PbWO_4) crystals in the barrel (EB) and 7324 crystals in each endcap (EE) part. The barrel crystal cross section is approximately $22 \times 22 \text{ mm}^2$, which covers one Moliere radius and its length is 230 mm, which corresponds to 25.8 radiative lengths (X_0). In the barrel region, the front face starts at the radius of 129 cm, and at the distance of 314 cm in the endcaps. The endcap crystal front face covers $28.6 \times 28.6 \text{ mm}^2$, and the crystal length is 220 mm ($24.7 X_0$). The ECAL covers the pseudorapidity range $|\eta| < 3$ (Fig. 4.3).

Additionally in the forward region, $1.653 < |\eta| < 2.6$, there is a preshower detector. The preshower allows for the identification of the neutral pions and improves the electrons and photons position determination. The preshower is a sampling calorimeter with lead radiators and silicon strip sensors for readout. There are two lead layers, first is $2 X_0$ thick, second is $1 X_0$ thick. The silicon readout is divided into strips of 1.9 mm pitch, and the strips in two layers are orthogonal.

The ECAL resolution can be parametrized in term of the stochastic (S), noise (N) and the constant (C) contributions: $\left(\frac{\sigma}{E}\right)^2 = \left(\frac{S}{\sqrt{E}}\right)^2 + \left(\frac{N}{E}\right)^2 + C^2$. The values of the above parameters fitted to the test beam data for the part of the ECAL called a supermodule are listed in Figure 4.4 [52]. The resolution is between $\sim 1.5\%$ for $< 50 \text{ GeV}/c$ electrons to $\sim 0.4\%$ for electrons with momentum above $100 \text{ GeV}/c$.

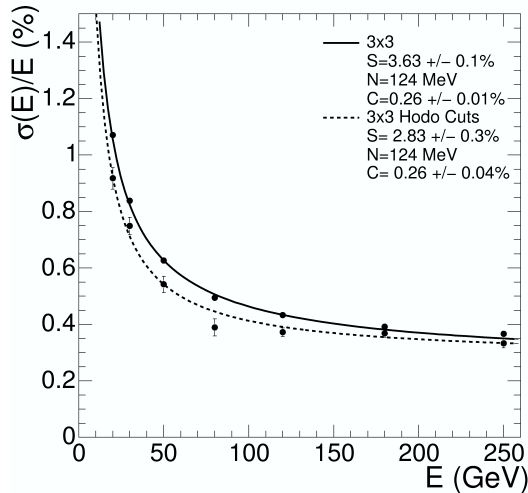


Figure 4.4: Electromagnetic calorimeter supermodule resolution [52].

4.2.2.2 Hadronic calorimeter

Hadron calorimeter (HCAL) is designed to provide the measurement of the strongly interacting particles and the missing transverse energy by covering the wide range in the η . The HCAL is composed of several parts: the barrel part (HB) covering the range $|\eta| < 1.4$, the endcap part (HE) in the range $1.4 < |\eta| < 3$, and the forward part (HF), covering the range $3 < |\eta| < 5$ (Fig. 4.3). In the barrel part, there is an additional scintillator layer outside the superconducting coil, covering $|\eta| < 1.2$, which serves as the “tail-catcher” of the showers leaving the barrel HCAL. The hadron calorimeter uses brass plates as the absorber, which are interspaced with the plastic scintillator tiles as the active elements.

The HCAL segmentation in the $\langle \eta, \varphi \rangle$ plane is 0.087×0.087 in the barrel part. In the endcap the segmentation varies from 0.087×0.087 for the smaller η to 0.37×0.175 at large η . The segmentation of the forward hadron calorimeter is 0.175×0.175 .

The measured resolution of the ECAL + HE system for the single pions in the endcap is parametrised as $\frac{\sigma}{E} = \frac{(140.2 \pm 1.1)\%}{\sqrt{E[\text{GeV}]}} \otimes (4.7 \pm 0.2)\%$ [52]. Figure 4.5 shows the ratio of the pion energy measured with ECAL+HB to the beam energy as a function of the beam momentum. The calorimeter response is nonlinear, therefore the measured energy requires corrections and the reconstruction step.

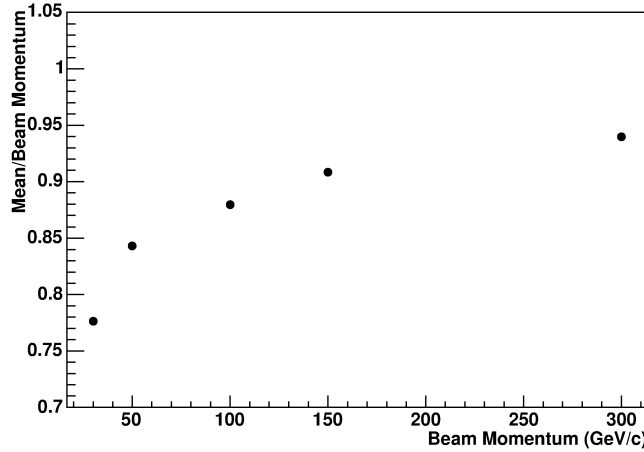


Figure 4.5: Non linear energy response of the ECAL+HE system for single pions as a function of the beam momentum [52].

4.2.3 Muon detectors

The muon identification is performed with the muon system, located outside the superconducting coil (Fig. 4.6). There are three types of the detectors in the

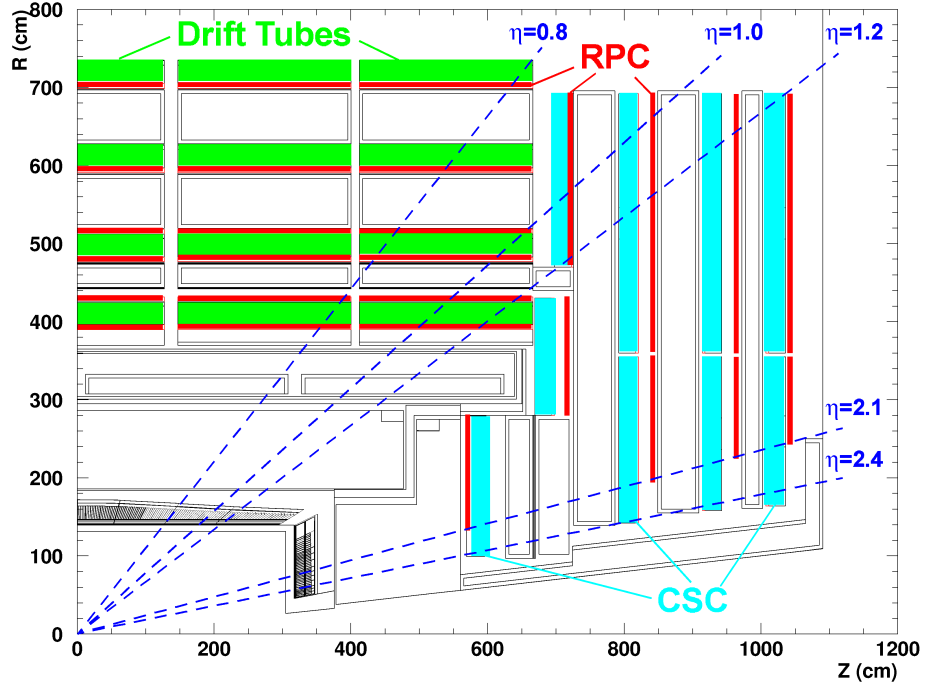


Figure 4.6: View of the CMS muon system [52].

muon system: the drift tubes (DT) located in the barrel region, $|\eta| < 1.2$, the cathode strip chambers (CSC) in the endcap region $1.2 < |\eta| < 2.4$ and the resistive plate chambers (RPC) in the whole detector up to $|\eta| < 2.1$.

The DT and the CSC chambers provide accurate track determination, with the precision of $100 \mu\text{m}$ in position and 1 mrad in the φ direction for the DT and 10 mrad for the CSC. The RPC spatial resolution is much worse than the DT and CSC, but the excellent time resolution of 2 ns provides efficient bunch crossing assignment, which is difficult for the two other muon detectors, which have drift time much longer than the time between two beam crossings.

The muon chambers are placed between iron layers of the magnet return yoke. They are arranged in four stations in barrel and endcaps. In the barrel, the stations form cylinders with radius of approximately 4, 5, 6 and 7 meters. In the endcaps, the muon stations are arranged in disks placed at 7, 8.5, 9 and 10 meters from the $z = 0$ plane (Fig. 4.6).

4.3 Triggering system

At the LHC the proton beams will collide each 25 ns , which gives the bunch crossing rate of 40 MHz . With the assumed luminosity of $\mathcal{L} = 10^{34} \text{ cm}^{-2}\text{s}^{-1}$ there will be $\sim 10^9$ interactions per second. Assuming the event size of the

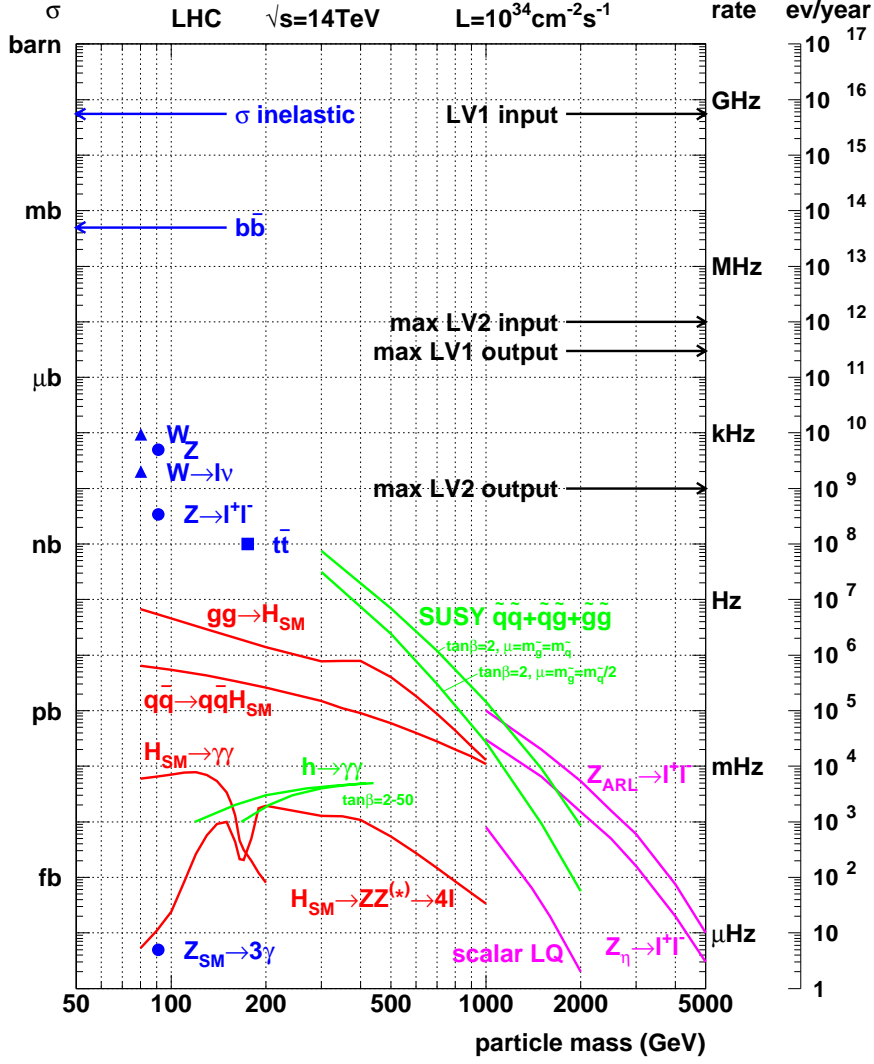


Figure 4.7: Cross section for selected processed to be observed at the LHC. The event rate for the high luminosity is shown.

order $\sim 1\text{MB}$, the data stream produced by each LHC detector will be of order of 40 PB/s , which is far beyond current data storage capabilities. Only about 100 MB/s can be saved to the mass storage. The trigger system is responsible for reducing the initial rate of 40 MHz to final 100 Hz . The system is divided into two parts: L1, which is hardware implemented logic in dedicated chips, and the high level trigger (HLT) which is designed as algorithms running in parallel on large computer farm. The maximal L1 trigger output rate is 100 kHz , which gives the reduction factor of $\sim 10^4$. To account for the uncertainties of cross sections at LHC energies, the safety factor of three is introduced. Therefore the L1 algorithms are designed to give the 30 kHz output. The HLT output rate is 100 Hz , which gives the reduction factor of ~ 1000 (Fig. 4.7).

The rate of the interesting “new physics” events is still much less than 100 Hz. It varies from ~ 10 Hz for the low mass supersymmetric particles, through single Hz for the Higgs boson production, to μHz for exotic physics like leptoquarks, or new gauge bosons (Fig. 4.7).

The event data will be stored in a pipeline before arriving to the L1 hardware. The pipeline can store data from 128 beam crossings, therefore the total time available to make the decision to whether accept the event is $128 \cdot 25 \text{ ns} = 3.2 \mu\text{s}$. Large fraction of this time is used for the propagation of the information from the detector to the counting room, where the L1 trigger hardware logic is placed. The time available for the L1 calculations is of order of $1 \mu\text{s}$. The L1 uses information from the muon and calorimetric systems only.

The HLT uses the full information available from the CMS detector. Each event is processed by a single processor. The HLT algorithms can be modified during the running of the experiment. The technique of the partial reconstruction is used during the HLT event processing: only the objects necessary to make the trigger decision are reconstructed, and events are rejected as soon as possible without reconstructing unnecessary objects.

The triggers used for the $\mu \tau$ jet final state are described in Chapter 6.

4.4 Reconstruction

The basic algorithms used for the reconstruction of elementary objects: charged particles tracks, vertices, jets with b tagging, muons, electrons, photons and missing transverse energy will be described in the current section. Some of the algorithms will be used already at the HLT level, some, being too much CPU time consuming, will be used at the offline selection step. A more detailed description of all the presented algorithms can be found in [52].

4.4.1 Tracks

The charged particles tracks can be reconstructed using the silicon tracking detectors, and muon chambers for the muon tracks. The charged particle track in the presence of the magnetic field is described by a helix. It requires six parameters to be fully determined: the position, and the momentum vectors. Having fixed a plane one has remaining five parameters to be reconstructed. Usually plane at the point of the closest approach of the track to the beam axis is chosen. The track is parametrised then by: d_0 – the distance in transverse plane, z_0 – the distance in the z direction, ϕ , and $\cot(\theta)$ – angles determining the momentum

direction and transverse momentum p_T . The track reconstruction, starting from reconstructed clusters in the tracker, consists in three main steps [52]:

1. Seed generation – initial track candidates are generated. Since the track is described by 5 parameters at least three hits (triplets), or two hits (pairs) with the vertex constraint are needed. Usually only the pixel detectors are used at this step. There are $\sim 4 \cdot 10^3$ pairs and $\sim 10^1$ triplets found in the $h \rightarrow ee\mu\mu$ events with the low luminosity;
2. Pattern recognition – using the coarse track parameters estimate from the track seed, the hits belonging to the track are searched in the tracker layers using the iterative Kalman filter method;
3. Track parameters fit – After finding all the hits belonging to the given track, the final parameter fit is performed. There are ~ 10 tracks with $p_T > 1$ GeV/c in the low luminosity $h \rightarrow ee\mu\mu$ events.

The minimal p_T of the reconstructed track in the central region ($\eta \sim 0$) is ~ 0.7 GeV/c. At this p_T the track curvature diameter is equal to the distance to the outermost tracker layer. The maximal p_T possible to reconstruct is determined by the tracker strip pitch. If the track bending inside the tracker volume is less than strip pitch, the track is reconstructed as a straight line, and the p_T is undetermined. The maximum reconstructible p_T in the CMS tracker is ~ 1 TeV/c.

4.4.2 Vertices

The vertex determination involves two steps: the vertex finding which groups tracks into vertex candidates, and subsequent vertex fitting with precise estimation of the vertex position. There are two groups of fitting algorithms used: linear (least squares) and non linear. In the linear approach all tracks have the same weight, whereas in the non linear approach tracks have individual weights and outlying tracks can be down weighted, or even discarded.

The most popular fitting algorithm is Kalman Filter (KF), which is mathematically equivalent to the global least squares method.

Another algorithm introduced for the first time in the CMS experiment is Adaptive Vertex Fitting (AVF). The AVF uses the iterative re-weighted fit. The individual track weight is reduced according to its reduced distance (χ^2) from the fitted vertex. The weights are varied until the fit converges.

4. CMS EXPERIMENT

Table 4.2: The resolution, 95% coverage and pull of the x and z -coordinates of the reconstructed vertex from the three vertex fitting algorithms, determined using different data samples, assuming a perfectly aligned tracker. The biases are compatible with zero and are not shown [52].

Filter	x -coordinate			z -coordinate		
	σ [μm]	95% Cov. [μm]	σ Pull	σ [μm]	95% Cov. [μm]	σ Pull
$B_s \rightarrow J/\psi\phi$ - secondary vertex						
KVF	54.8	164	1.08	73.8	471	1.08
AVF	53.6	155	1.02	73	440	1.02
TKF	54	174	1.04	75	502	1.05
$H \rightarrow \gamma\gamma$ - primary vertex						
KVF	28.1	124	1.11	34	152	1.06
AVF	22.1	73.7	0.9	29.2	106	0.9
TKF	23	74.9	0.93	29.6	111	0.92
$t\bar{t}H, m(H) = 120 \text{ GeV}/c^2$ - primary vertex						
KVF	14	118	1.51	17.9	122	1.46
AVF	9.55	21.1	0.99	13	30.3	1
TKF	9.87	21.7	1.01	13.3	31.7	1.02

Next algorithm is the Trimmed Kalman Filter (TKF) which is a robust version of the conventional KF vertex fitter, where tracks are removed from the fit starting from the least compatible track.

Table 4.2 summarizes the performance of the three described algorithms for several representative event types. The variance of the Gaussian fit to the distribution of the fitted vertex parameters is shown. A half width of the area covering the 95% of the events (95% Cov.) is shown for the estimation of the non Gaussian tails. Also, the fit to the pull of the mean value $\left(\frac{x^{\text{fit}} - x^{\text{gen}}}{\sigma_x}\right)$ has been done. The standard deviation of the fit is shown (σ Pull). The transverse position resolution varies from 10 μm for the primary vertex in the $t\bar{t}H$ events to 55 μm for the $B_s \rightarrow J/\psi\phi$ secondary vertex. The pull is compatible with zero, and its width is close to 1.

4.4.3 Muons

The muon reconstruction starts from the reconstruction of a muon track in the muon system only, then the track is propagated to the tracker system and the compatible tracker hits are searched. The last step is refitting the muon track with all the hits from the tracker and the muon systems. The resolution at $\eta = 0.1$ of the reconstructed muon momentum with the full system, tracker part only and

the muon system only is presented in Figure 4.8. The inner tracker resolution dominates for the muon tracks with the $p_T < 100$ GeV/c. The resolution in the central region ($|\eta| < 0.2$) is of order of 5% for the very high energetic muon tracks with the $p_T \sim 1$ TeV/c.

Important part of the muon identification is the muon isolation. The muon isolation can be done by requiring that there are no tracks within a given cone around the muon track. Also it can be required that there are no deposits in the calorimeter system around the muon track impact point on the calorimeter surface. In this case one has to exclude small cone around the muon track not to count the deposit from the muon itself.

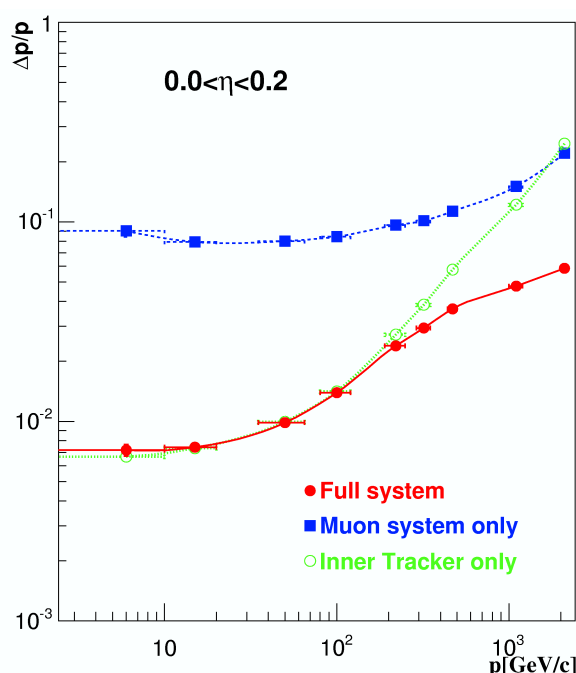


Figure 4.8: Muon p_T resolution for the muon reconstructed with the tracker and muon systems, with tracker only, and with the muon system only [52].

4.4.4 Electrons and photons

The presence of material in front of the the calorimeter, varying from $0.4 X_0$ for the $\eta \simeq 0$ to $1.4 X_0$ for the $\eta \simeq 1.5$ (Fig. 5.1) causes large photon radiation (bremsstrahlung) off the electrons passing the tracker volume. The possible subsequent conversions of the bremsstrahlung photons increases the difficulty of the electron energy reconstruction. The presence of the bremsstrahlung introduces large non-Gaussian event-by-event energy loss fluctuations, which cause the large

tails in the track momentum resolution. To recover the energy spread in φ , groups of cells called a supercluster are formed.

Electron reconstruction starts from finding the superclusters in the ECAL, which serve as a seed for the track reconstruction. The energy is reconstructed as a weighted mean of the track momentum and the supercluster energy. The resolution for the combined energy measurement, and for the separate supercluster and track measurements are shown in Figure 4.9. The calorimetric measurement dominates the total energy reconstruction resolution for the electrons with $p_T > 15$ GeV/c. Electron identification involves a number of variables, like the E/p ratio of the energy reconstructed in ECAL to the momentum reconstructed in the tracker [52].

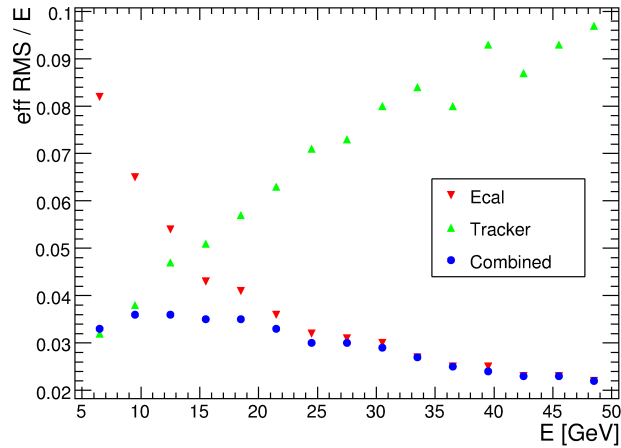


Figure 4.9: Electron energy resolution for the energy reconstructed with the ECAL alone, from the tracker track and the combined information from the calorimeter and the tracker [52].

The photons are identified using the photon isolation, which requires that there are no additional charged particles, reconstructed in the tracker, or neutrals in the calorimeter [52]. The photon energy is reconstructed by adding up the energy deposits in the 5×5 ECAL cell area for the non converted photons. For the photons that underwent a conversion in the tracker material the spread of the energy deposits is larger due to the bending and of the electrons and their bremsstrahlung. In that case, a sum over a supercluster is used as a estimate of the photon energy. The photon is considered to be converted if the energy contained in the 3×3 blocks of the ECAL cells around the cell with the maximal deposit is less than 94.3% of the total cluster energy. The resolution of the photon energy reconstructed for the class of events, where a 94.3% of the photon energy was contained in a 3×3 blocks of the ECAL cells, is shown in Figure 4.10.

This class covers 70% of the $H \rightarrow \gamma\gamma$ events. The resolution parametrisation is shown. The energy resolution for the high E ($E > 100$ GeV) photons is limited by a constant term of 0.66%.

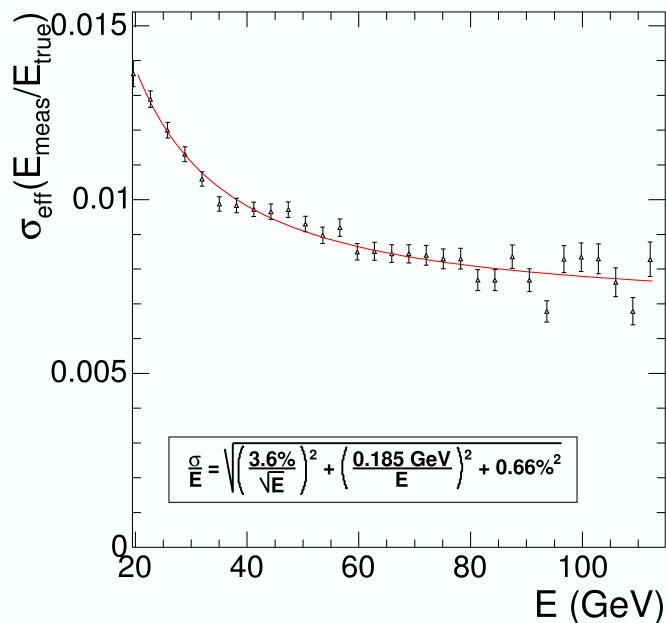


Figure 4.10: Photon energy resolution for the events where 95.4% of the super-cluster energy was contained in the 3×3 cells region around the cell with the maximal energy deposit [52].

4.4.5 Jets

The jet algorithms use the trigger calorimeter towers as input objects. The calorimeter tower covers one HCAL cell, and several ECAL cells. The HCAL cell size in the barrel is 0.087×0.087 in the $< \eta, \varphi >$ space. Three main jet algorithms are used in the CMS reconstruction software:

- iterative cone algorithm [52; 53] ;
- midpoint cone algorithm – this algorithm is a modification of the iterative cone algorithm, which ensures the infrared safety of the jetting procedure [53]. A detailed description of the algorithm can be found in [52];
- inclusive k_T algorithm – a detailed description of the algorithm can be found in [52].

In this analysis the simplest, iterative cone algorithm was used. In this algorithm a cone in the $< \eta, \varphi >$ space is cast around the input object with the maximal E_T above specified threshold. The objects inside the cone are summed up using the E_T recombination scheme (described below) and form a proto-jet. The computed direction is used as a new seed, and the procedure is repeated until the computed jet energy vary less than 1% and the direction vary less than $\Delta R < 0.01$. Then the objects forming the jet are removed from the list of all the input objects, and the proto-jet is added to the list of jets. The procedure of forming proto-jets is repeated until there are no input objects above the specified threshold. There are two ways, the so called recombination schemes, to construct the jet momentum four-vector from constituents four-vectors:

- the E recombination scheme, where constituents four vectors are added. This scheme leads to massive jets;
- the E_T recombination scheme, where the transverse momentum of jet is defined as a sum of E_T of all constituents, and the jet position is estimated as weighted mean position of constituent with the E_T used as a weight, e.g.
$$\varphi_{\text{jet}} = \sum E_{Ti} \varphi_i / \sum E_{Ti}.$$

The jet resolution for three η ranges: the central part $|\eta| < 1.4$, the forward part $1.4 < |\eta| < 3.0$ and the very forward part $3.0 < |\eta| < 5.0$ is presented in Figure 4.11. The jets were reconstructed using the iterative cone algorithm with cone size $R = 0.5$, and E_T recombination scheme. The jet resolution is of order of 60% for jets with $E_T < 50$ GeV, and of order of 10% for jets with high E_T . The improvement of the jet resolution for jets with the same E_T , but in more forward region, is caused by higher total jet energy for jets with the same E_T , but higher η . The results do not depend significantly on the jet algorithm, or the recombination scheme.

4.4.6 b tagging

Many processes involve production of b quarks and subsequent production of b hadrons in the hadronization process. The b hadrons can be distinguished from the lighter hadrons by their relatively long life time ($\simeq 1.5$ ps, $c\tau \simeq 450$ μm), their large mass and relatively large branching ratio into leptons (of order of 10%). The long life time leads to displaced secondary vertex. There are three main b tagging algorithms used in CMS:

- track counting – in this algorithm a jet is b tagged if it contains certain number of tracks with sufficiently large transverse impact parameter;

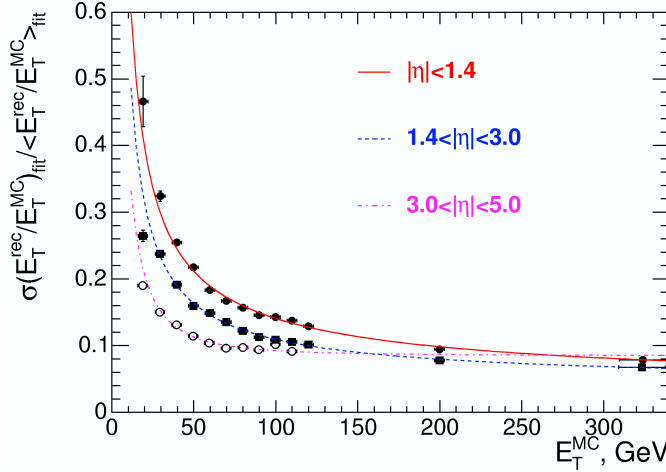


Figure 4.11: Jet transverse energy resolution for three η regions of the CMS detector [52].

- probability b tagging – for each track in a jet the probability for coming from the primary vertex is computed, then a combined probability P_{jet} for the whole jet is calculated. The discriminating variable $-\log(P_{\text{jet}})$ is peaked near 0 for jets coming from light quarks and gluons;
- combined secondary vertex tag – in this algorithm the secondary vertex of the weakly decaying b-hadron is reconstructed. To improve the purity of the tagging, additional discriminating variables are used, like the invariant mass of charged particles associated with the secondary vertex and the tracks multiplicity. The variables are combined into one discriminating variable using the Likelihood ratio technique.

The track counting algorithm was used in this analysis. The algorithm is very simple, therefore it requires small amount of the CPU time. Also it does not require calibration, which makes it more robust with respect to the two other algorithms. It will be particularly useful at the beginning of the LHC running, when the detector will not be fully understood yet.

The misstag efficiency versus the b-tag probability for the light quark jets, c jets and the gluon jets tagged with the track counting algorithms presented in Figure 4.12. At the 50% efficiency the miss tag probability is 10% for the c-jets, 2 % for gluon jets and 0.7% for light quarks jets.

4.4.7 Missing transverse energy

The missing transverse energy ($\vec{\cancel{E}}_T$) is reconstructed as a vector sum of all the deposits in the calorimeter trigger towers. Each deposit is treated as a two–

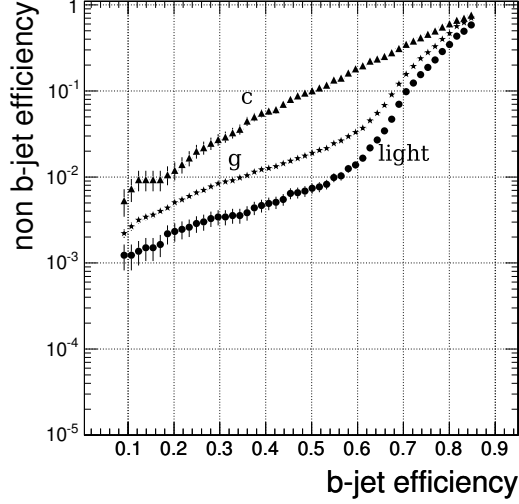


Figure 4.12: Track counting b miss tag probability versus the b tag efficiency for gluon, c quark and light quark jets [52].

dimensional vector, with magnitude equal to the deposit E_T , and the direction set by the deposit position (Eq. 4.1).

$$\vec{E}_T = -\Sigma(E_n \sin \theta_n \cos \varphi_n \hat{e}_x + E_n \sin \theta_n \sin \varphi_n \hat{e}_y) = -E_{Tx} \hat{e}_x - E_{Ty} \hat{e}_y \quad (4.1)$$

Reconstructed muons are also taken into account, by subtracting the reconstructed muon \vec{p}_T from the calculated \vec{E}_T .

The reconstructed \vec{E}_T has poor resolution, therefore it should be corrected with the use of the reconstructed and calibrated jets in an event instead of the raw calorimeter trigger towers (the so called Type 1 corrections). The missing transverse energy error for the $t\bar{t}$ events with and without the jet corrections is shown in Figure 4.13. The inclusion of the jet corrections improves significantly the \vec{E}_T bias ($\Delta E_T^{\text{miss}} = E_T^{\text{rec}} - E_T^{\text{gen}}$). The \vec{E}_T direction resolution is particularly important in the analyzes which require the reconstruction of the particle mass with the use of the \vec{E}_T , e.g. for $W \rightarrow l\nu$ with ν taken from the \vec{E}_T . The direction resolution as a function of the missing \vec{E}_T is shown in Figure 4.14. The resolution is of order of 0.5 radians (28°) for the low values of the \vec{E}_T .

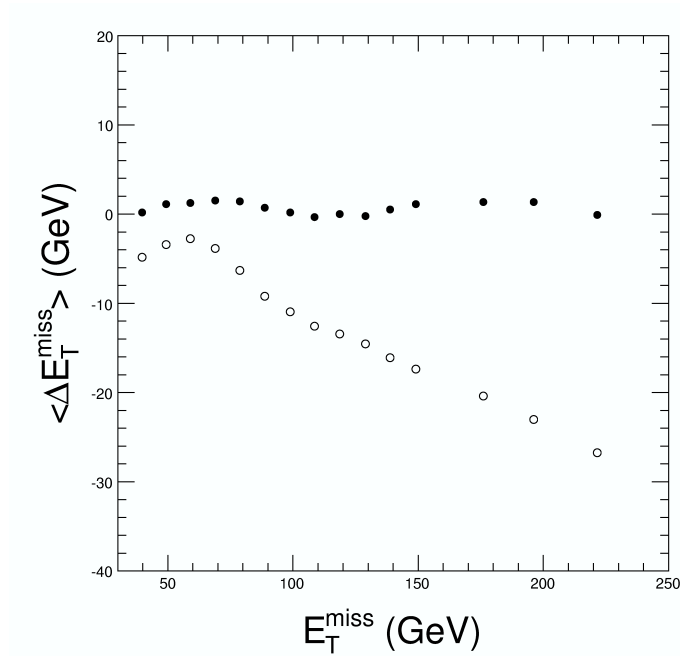


Figure 4.13: Error on the reconstructed missing transverse energy for the $t\bar{t}$ events with (full circles) and without (open circles) the jet corrections [52].

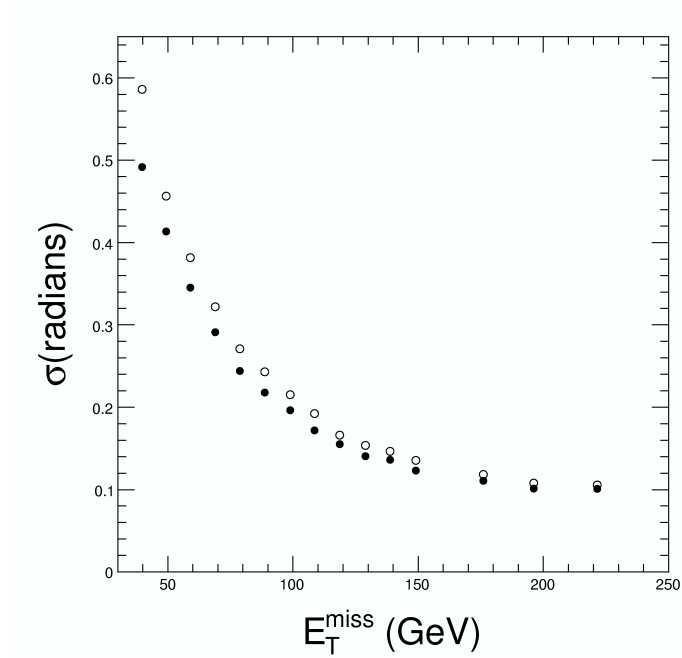


Figure 4.14: Missing transverse energy direction resolution for the $t\bar{t}$ events with (full circles) and without (open circles) the jet corrections [52].

Chapter 5

Physics simulation

Results presented in this thesis are based on the Monte Carlo simulations of the physical processes and the CMS detector response. The simulation consists in three main steps:

- **generation** – list of particles momenta four vectors produced in the pp collisions is generated;
- **simulation** – the particles are propagated through detector representation. The interaction of the particles with the detector material is simulated;
- **digitization** – using simulated particle interaction with detector, a digital response is produced, e.g. charge collected on the silicon strips is expressed in terms of the ADC ¹ counts.

Below all steps of the simulation process are described in some detail.

5.1 Generation

5.1.1 Introduction

The generation of the list of the particles coming out from the pp collision includes simulation of the so called hard process, e.g. $gg \rightarrow b\bar{b}H$, which results in the four momenta of the outgoing particles: b , \bar{b} and H . The longitudinal momenta components of the initial partons are chosen according to the partons density distributions. The transverse momenta components, called the primordial parton k_T , are calculated assuming Fermi's momenta inside a nucleon. The four momenta of the final state particles are generated according to the differential cross sections for the given process. Usually leading order (LO) formulas are used [44]. Before the partons interact the initial state radiation (ISR), which includes radiation

¹ADC – Analog to Digital Converter

processes like $g \rightarrow gg, q \rightarrow gq$, is simulated. The similar procedure is applied to the outgoing partons, and it is called final state radiation (FSR). The ISR and FSR together are called parton showers. Parton showers include some leading-logarithmic (LL) corrections, making the LO with parton shower treatment to correspond to analytical LO calculations with LL corrections [44].

On the top of the final state of the hard scattering process, the remnants of the colliding protons, as well as results of another partons collisions, the so called underlying event (UE), are added. The structure of the UE was studied in detail in the Tevatron [54; 55], and will be studied at the LHC [56]. In the current simulation, a description of the underlying event fitted to the Tevatron data, and extrapolated to the LHC energy, is used.

At the end of the generation processes, partons are hadronised and short living ($c\tau < 10$ mm) particles are decayed. In the PYTHIA program the hadronisation is done using the Lund fragmentation model [57].

It has been verified that the LO PYTHIA with parton showers result reproduces well most of the NLO kinematic distributions for the signal $gg \rightarrow b\bar{b}H$ process. The details of the comparison are presented in the Appendix A.

5.1.2 The generation procedures

Generation of the physical processes has been done using the PYTHIA 6.215 [44] program with the CTEQ5L [58] parton density distribution. The PYTHIA program was used through the general CMS interface to Monte Carlo generators – the CMKIN package [59].

The decays of the τ leptons coming from Higgs bosons were done using a dedicated program – TAUOLA [60]. This program takes into account the τ pair polarization state depending on the spin of the decaying particle, and includes complete $\mathcal{O}(\alpha_s)$ corrections to the leptonic decays, and approximate simulation of QED corrections for hadronic decays [60].

All the event samples were produced using official CMS production service [61], except for the signal events for $m_A = 300$ GeV/ c^2 , which were produced by the author using the CERN batch services [62]. Table 5.1 shows the list of generated event samples, including the number of available events.

A fixed set of MSSM parameters has been used to generate signal events. Dependency of the results on the MSSM parameters was obtained with proper cross section normalization. This procedure is reliable, since in the considered range of parameters the Higgs boson width remains smaller than the mass resolution (Chapter 3). Only the CP even Higgs boson production was considered. Since

5. PHYSICS SIMULATION

Table 5.1: List of generated events types. The number of produced events is shown.

Process	Number of of events	Comment
$gg \rightarrow b\bar{b}H \rightarrow \mu + \tau \text{ jet} + X$	9k	$m_A = 200 \text{ GeV}/c^2$
$gg \rightarrow H \rightarrow \mu + \tau \text{ jet} + X$	10k	$m_A = 200 \text{ GeV}/c^2$
$gg \rightarrow b\bar{b}H \rightarrow \mu + \tau \text{ jet} + X$	10k	$m_A = 500 \text{ GeV}/c^2$
$gg \rightarrow H \rightarrow \mu + \tau \text{ jet} + X$	10k	$m_A = 500 \text{ GeV}/c^2$
$gg \rightarrow b\bar{b}H \rightarrow \mu + \tau \text{ jet} + X$	9k	$m_A = 300 \text{ GeV}/c^2$, private production
$b\bar{b}$	898k	$\hat{p}_T > 20 \text{ GeV}/c$
$t\bar{t}$	287k	—
$W \text{ jet}$	897k	$\hat{p}_T > 20 \text{ GeV}/c$
$g b \rightarrow W t$	467k	—
$Z/\gamma^* \rightarrow \mu + \tau \text{ jet} + X$	100k	Z/γ^* with $40 < m_{\tau\tau} < 120 \text{ GeV}/c^2$
$Z/\gamma^* \rightarrow \mu + \tau \text{ jet} + X$	99k	Z/γ^* with $m_{\tau\tau} > 120 \text{ GeV}/c^2$
$b\bar{b}Z \rightarrow \tau\tau$	290.5k	$b\bar{b}Z/\gamma^*$ with $60 < m_{\tau\tau} < 100 \text{ GeV}/c^2$
$b\bar{b}Z \rightarrow \tau\tau$	100k	$b\bar{b}Z/\gamma^*$ with $m_{\tau\tau} > 100 \text{ GeV}/c^2$

the two heavy Higgs bosons are almost degenerate in mass, the cross section normalization for the signal sample was the sum of the cross sections for the A and H bosons.

A preselection procedure at the parton level was applied to save CPU time and disk space. The preselection cuts were chosen in such a way that the selected events were more likely to pass the trigger selection (Chapter 6). These requirements were:

- at least one isolated muon with $p_T > 15 \text{ GeV}/c$;
- at least one isolated τ -like jet with $E_T > 30 \text{ GeV}/c^2$.

The isolation requirement for muons was defined as no charged particle tracks with $p_T > 1 \text{ GeV}/c$ within a cone of radius $R = 0.2$ in the $\langle \eta, \phi \rangle$ space around the muon momentum direction.

The isolation requirement for the τ jets allowed for at most one additional charged particle track with $p_T > 1 \text{ GeV}/c$ in the ring around the jet leading track with the inner radius $R_{\text{in}} = 0.1$, and the outer radius $R_{\text{out}} = 0.4$. The leading track was required to have $p_T > 3 \text{ GeV}/c$.

These preselection criteria are softer than the trigger selection, presented in the Chapter 6. The preselection efficiencies for all considered processes are shown in Table 5.2. The numbers for the signal samples include selection of the $\tau\tau \rightarrow \mu + \tau \text{ jet} + X$ decay channel.

Table 5.2: Generator level preselection efficiency. Numbers in parentheses show the generated m_A .

Event sample:	Preselection efficiency
$b\bar{b}H(200)$	$9.47 \cdot 10^{-2}$
$H(200)$	$9.12 \cdot 10^{-2}$
$b\bar{b}H(300)$	$1.31 \cdot 10^{-1}$
$bbbH(500)$	$1.65 \cdot 10^{-1}$
$H(500)$	$1.58 \cdot 10^{-1}$
$t\bar{t}$	$9.01 \cdot 10^{-2}$
Wj	$1.44 \cdot 10^{-2}$
Wt	$6.58 \cdot 10^{-2}$
$b\bar{b}$	$7.56 \cdot 10^{-4}$
$Z/\gamma^*, 40 < m_{\tau\tau} < 120 \text{ GeV}/c^2$	$6.56 \cdot 10^{-2}$
$Z/\gamma^*, m_{\tau\tau} > 120 \text{ GeV}/c^2$	$2.14 \cdot 10^{-1}$

An event sample without preselection was used for the $b\bar{b}Z \rightarrow \tau\tau$ process.

A special procedure has been used for the $b\bar{b}$ events. Every event was decayed and fragmented 100 times and the last decay passing the preselection criteria was saved. A weight equal to the fraction of events passing the preselection was assigned to the event. The average weight was 0.025. The weight is not included in the Table 5.2, but it is taken into account in all other efficiency tables of Chapter 6 and Appendix B. The overall normalization of the $b\bar{b}$ events includes additional factor 7 to account for the simplifications at the generation step. This normalization procedure is explained in details in Appendix B.

5.2 Simulation

Stable and long living (e.g. K^\pm) particles obtained at the generation process are propagated through the detector volume, and decayed if $c\tau > 10 \text{ mm}$. The propagation includes the effect of the magnetic field present in the CMS detector and interaction with the detector material which leads to the multiple scattering and energy deposits in the active detectors volumes. The interactions between particles and the detector material is simulated using Geant 4 (G4) program [63] through the CMS simulation program OSCAR [18].

The CMS detector geometry implemented within the OSCAR program reflects the future detector geometry basing on the engineering drawings. The detector elements are implemented with details. Active volumes like the gas gaps in the

gaseous detectors, but also supporting structures, and dead zones like gaps between active areas are represented. The amount of the material in the tracker expressed in radiation lengths X_0 is shown in Figure 5.1. The magnetic field

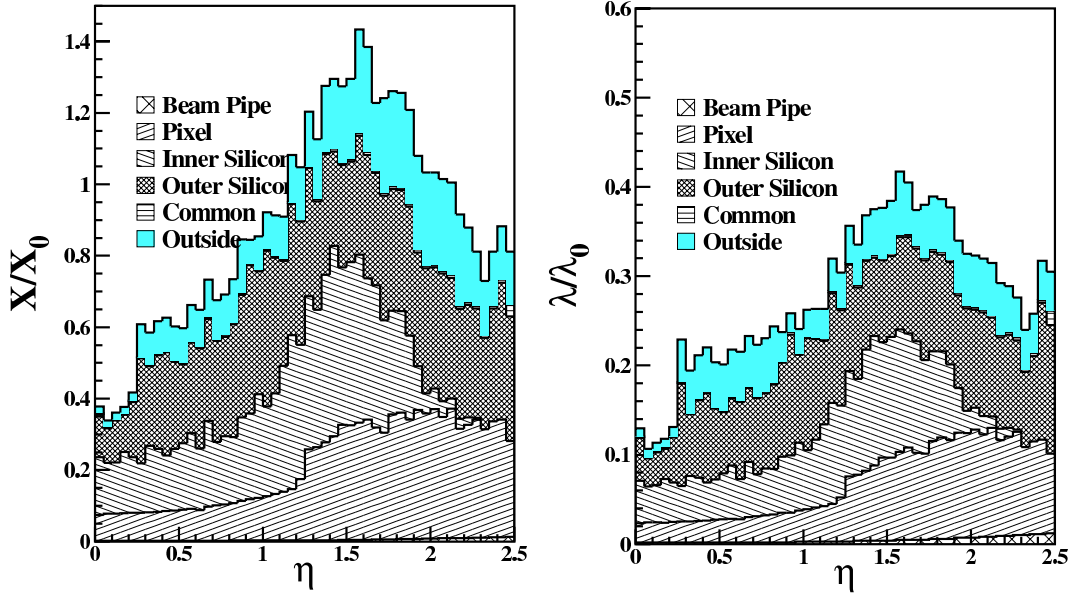


Figure 5.1: Material budget of the tracker system expressed in the units of radiation length (left plot) and interaction length (right plot) [52].

within the detector volume is represented by 3D field map.

The presence of the material in front of the ECAL leads in particular to photon conversion. The effect of the photon conversions as well as many other are present in the G4 physics simulation. The details of the CMS simulation program implementation are described in [52]. The simulation result is the list of the active detector volumes containing any deposits, called *hits*, left by the traversing particles coming from the initial pp collision, or from secondary interactions in the detector material, e.g. bremsstrahlung photons.

In reality the CMS detector will not be ideally equivalent to its engineering design, and there will be some misalignment of the detector elements with respect of each other, even after applying sophisticated alignment algorithms [52]. The effect of misalignment can be reproduced with the CMS simulation framework.

5.3 Digitization

At the digitization step the detector electronic response to the energy deposits in the active volumes is simulated. The digitization result, called *digi* is designed to be as close as possible to the real data coming from the detector read out system.

The simulation of the detectors and electronics response includes the detector inefficiency, detector noise, signal propagation through electronic systems leading to time delays and many other effects [52].

At the digitization step, the pile-up effect is taken into account. The number of the pp interactions in one bunch crossing depends on the machine luminosity. On average it is expected 5 pp interactions per beam crossing for the “low luminosity” ($\mathcal{L} = 2 \cdot 10^{33} \text{ cm}^{-2}\text{s}^{-1}$), and 25 for the “high luminosity” ($\mathcal{L} = 10^{34} \text{ cm}^{-2}\text{s}^{-1}$), including diffractive pp collisions. Some CMS subdetectors have relatively long response time. The Muon Drift Tubes drift time is of order of 16 beam crossings, i.e. 400 ns. The long response time leads to the effect of the out-of-time pile-up, when the deposits from the particles coming from few beam crossings are accumulated. Therefore for “slow” detectors, the real pile-up rate is higher than the pile-up rate for single beam crossing.

Chapter 6

Analysis

6.1 Trigger path

CMS trigger selection is divided into two parts: Level 1 trigger based on hardware logic [64], and High Level Triggers (HLT) implemented in the online selection software running on a large filter farm [65].

The selection criteria for the $\mu \tau$ jet channel are described in details below.

6.1.1 Level 1 trigger

The Level 1 trigger operates on simple objects like clusters in the calorimeter, or muons reconstructed in the muon system [64; 66].

At least one μ with $p_T \geq 14$ GeV/c was required at Level 1 for the $\mu \tau$ jet at low luminosity. The Level 1 muon trigger uses information from the three muon subsystems of the CMS detector: RPC up to $|\eta| < 2.1$, DT $|\eta| < 1.2$ and CSC in $1.2 < |\eta| < 2.4$ region (Chapter 4.2.3). The information from all three muon subsystems is combined by the Global Muon Trigger (GMT) [64]. The average L1 efficiency for the muons in the $|\eta| < 2.4$ and $5 < p_T < 100$ GeV/c is expected to be 98.3% [52].

6.1.2 High Level Trigger

High Level Trigger selection requires an isolated muon and an isolated τ jet in the event. The selection requirements are listed below:

- calorimeter jet with $E_T \geq 40$ GeV and $E_{\text{isol}} \leq 5.6$ GeV (described below), isolated in the pixel detector;
- AND μ with $p_T \geq 15$ GeV/c and calorimetry isolation ≤ 0.97 ;
- AND μ with tracker isolation ≤ 0.97 ;

- AND same μ and τ – jet vertex : $\Delta z(\mu, \tau - \text{jet leading track}) < 0.2$ cm, with z being the coordinate along the beam line.

The E_{isol} variable for the τ jet is the energy in a ring around the jet direction with an inner radius $R_{\text{in}} = 0.13$ and an outer radius $R_{\text{out}} = 0.4$. The requirement of $E_{\text{isol}} < 5.6$ GeV comes from the fact that real τ jets are very collimated [66].

The τ jet isolation [67; 68] requires that there are no tracks with $p_T > 1$ GeV/c in the isolation ring with an inner radius $R_s = 0.07$, and an outer radius $R_i = 0.35$ (Fig. 6.1). Tracks inside the inner cone (called the signal cone), are considered to come from the τ decay. The leading track is required to have $p_T > 3$ GeV/c, and should be within the matching cone, centered on the jet axis with radius $R_m = 0.1$. Due to the CPU time limitations for HLT algorithms information from pixel detectors only is used for the track reconstruction. The offline cut on the leading track p_T is set at 10 GeV/c, however the momentum resolution of tracks reconstructed with pixel hits only is poor therefore a lower cut is used in the HLT selection. In the presence of high pile-up the tracks coming from other interaction vertices may spoil the isolation of the real τ jets, therefore only tracks with their vertex z position close to the one of the leading track ($\Delta z < 0.2$ cm) are considered in the isolation procedure.

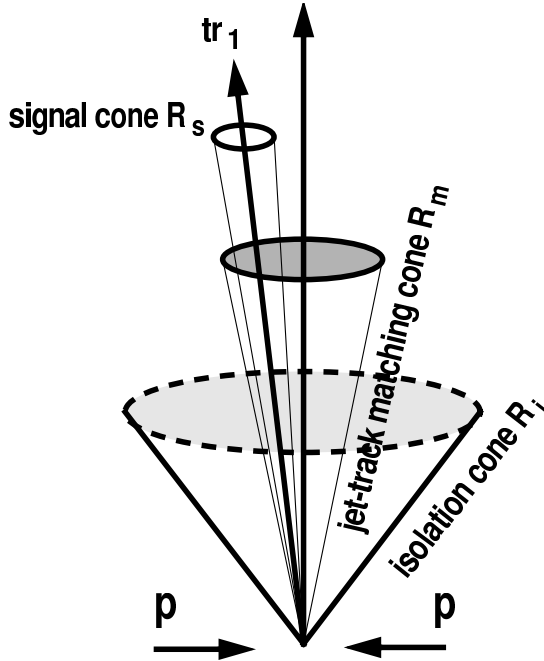


Figure 6.1: Definition of the cones used for the τ jet isolation.

The HLT muon isolation algorithms rely on the comparison of the energy deposit in a cone around the muon with the predefined threshold. The deposit

can be transverse energy for calorimeter based isolation or the sum of transverse momenta of reconstructed charged-particle tracks for tracker based isolation. The thresholds and cone sizes are adjusted automatically to retain 97% efficiency for $W \rightarrow \mu\nu$ events (HLT reference signal) and maximize the rejection for $b\bar{b} \rightarrow \mu X$ events (HLT reference background). At HLT calorimeter- and tracker-based algorithms are applied in cascade. More details about the muon isolation algorithms can be found in [69].

The z position of the τ – jet vertex was defined as the τ – jet leading track z position at the point of closest approach to the beam line. The leading track was reconstructed with the pixel system only. The muon vertex position along the beam line (the z coordinate) was taken from the reconstructed track position at the closest approach to the beam line [70]. The track was fitted without any constrain on the vertex position.

The efficiencies of the full trigger chain (L1+HLT) selection for the signal and background events is shown in Tables F.1 – F.5 of Appendix F

6.2 Offline selections

Offline selections can be divided into three groups: offline τ identification, cuts providing efficient background selection and cuts necessary for a good Higgs boson mass reconstruction.

All offline selection cuts are summarized below:

- Offline τ identification:
 - full tracker τ isolation;
 - 1 or 3 tracks in the τ signal cone;
 - improved τ – jet direction reconstruction.
- Background suppression specific selections:
 - leading τ – jet track $p_T > 10$ GeV/c for single prong decays, and $p_T > 20$ GeV/c for three prong decays;
 - opposite charge of the μ and the τ – jet signal tracks;
 - one b-tagged jet;
 - jet veto (no other jets with $E_T^{\text{calib.}} \geq 20$ GeV and $|\eta| \leq 2.4$);
 - $m_T(\mu, \cancel{E}_T) \leq 60$ GeV;

- ratio of jet HCAL energy to leading τ – jet track momentum:
 $0.2 < f < 1.1$ for single prong decays.

- Mass reconstruction specific selections:

- $-0.9962 \leq \cos(\Delta\varphi_{\mu,\tau \text{ jet}}) \leq -0.5$, ($\cos(175^\circ) = -0.9962$);
- positive reconstructed neutrino energy: $E_{\nu 1} > 0$, $E_{\nu 2} > 0$, which is equivalent to the requirement for the \vec{E}_T to be inside the $\mu - \tau$ jet $\Delta\varphi$ angle.

Since the calorimetric features of highly collimated τ jets are fully exploited at the trigger level no further offline selections based on the calorimeter are done.

Appendix C contains distributions of all selection variables for all considered event samples after the offline τ identification. Appendix D contains the same distributions after each offline selection, showing the correlations between the variables for the $b\bar{b}H$ with $m_A = 200 \text{ GeV}/c^2$ and the $t\bar{t}$ processes. All offline selections are described in detail below.

6.2.1 Offline τ identification

In the offline τ jet identification [67] the isolation algorithm identical to the one used at the HLT was used, but with the fully reconstructed tracks using all available tracker hits. Additionally, in order to retain one and three prong τ decays, only one or three tracks in the signal cone are allowed.

The offline τ jet is reconstructed using the iterative cone jet algorithm (Chapter 4.4.5), with the cone size $\Delta R = 0.4$. The sum of the momenta of the signal tracks is used for the τ – jet direction estimation. This gives much better direction resolution than the calorimeter jet alone, as shown in Figure 6.2). The calorimeter jet estimate with the Monte Carlo τ energy calibration [67] was used for the energy measurement.

6.2.2 Background suppression specific selections

6.2.2.1 Leading τ – jet track p_T cut

The leading τ – jet track is required to have $p_T > 10 \text{ GeV}/c$ in case of a single track in the signal cone, and $p_T > 20 \text{ GeV}/c$ for three prong decays, to suppress b jets faking a τ jets, (Fig. C.3, C.4).

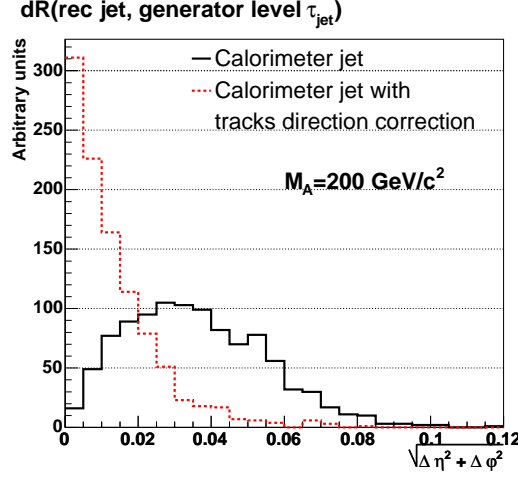


Figure 6.2: Direction resolution of the τ jet for $m_A = 200 \text{ GeV}/c^2$. The resolution is calculated as the difference in the directions of the MC jet and the reconstructed jet. The generated MC jet direction was calculated from the generated particles momenta.

6.2.2.2 Opposite charge of the μ and τ – jet signal tracks

The fact that the two taus have opposite signs is exploited by requiring the μ and the sum of charges of the τ – jet signal tracks to be opposite. This selection suppresses mainly the Wj process (Tab. F.8).

6.2.2.3 Single b tagging

To select events with associated $b\bar{b}H$ production at least one b tagged jet was required. A simple track counting method was used: a jet was b tagged if it had at least two tracks with 2D transverse impact parameter significance ($S = d_{\text{IP}}/\sigma_d$) greater than two. The b tagging efficiency, including the jet finding efficiency, for signal events was 0.17 for $m_A = 200 \text{ GeV}/c^2$ and 0.26 for $m_A = 500 \text{ GeV}/c^2$. For backgrounds with real b quarks it was 0.67 for $t\bar{t}$ and 0.46 for Wt. The “non-b” backgrounds had the mistag efficiency of 0.01 for the Wj and 0.03 for the Z/γ^* . The reason for the low b tag efficiency for the signal is the soft p_T spectrum of the associated b quarks. Only 36% of events from signal with $m_A = 200 \text{ GeV}/c^2$ have real b jets with $E_T > 20 \text{ GeV}$, and $|\eta| < 2.4$. Current results are in good agreement with the previous studies on the b tagging for this channel [71]. Since the b-jets are quite soft, demanding double b-tagging would reject most of the signal events. The b-tagging is, however, very efficient against the Wj and Z/γ^* backgrounds (Tab. F.8, F.9).

6.2.2.4 Central jet veto

An additional criterion against $t\bar{t}$ is the central jet veto. All events containing additional jets (other than the τ jet and the b-tagged jet) in the central region: $|\eta| \leq 2.4$ and with calibrated $E_T \geq 20$ GeV were rejected. The jets are reconstructed from the ECAL plus HCAL trigger towers with energy deposits greater than 0.8 GeV, and transverse energy greater than 0.5 GeV to reduce the rate of the fake jets at low E_T [72].

6.2.2.5 Transverse mass cut

Events containing W bosons decaying into $\mu + \nu_\mu$ are rejected using the cut on the transverse mass of the muon and the missing transverse energy (\cancel{E}_T): $m_T = \sqrt{2 \cdot p_T^\mu \cdot \cancel{E}_T (1 - \cos(\vec{p}_T^\mu, \vec{\cancel{E}}_T))}$. This quantity has a Jacobian peak near the W mass for μ coming from the W decay. Rejection of events with $m_T > 60$ GeV largely reduces the $t\bar{t}$, Wt and Wj backgrounds and retains a good fraction of signal events, (Fig. C.7, Tab. F.8, F.9).

6.2.2.6 Electron veto

W bosons in $t\bar{t}$ and Wt background samples are sources of electrons which are often misidentified as a τ jet. A cut on the ratio of the τ – jet energy in the HCAL to the leading track momentum has been used for electron rejection. The ECAL could not be used due to the presence of deposits from π^0 coming from the τ decay. The lower cut value was set to $f = 0.2$. This selection retains 90% of signal events and rejects 95% of events with real electrons. The cut on the upper value of the ratio is efficient against quark jets rich in neutral hadrons. The cut on $f = 1.1$ rejects 50% of Wj and $b\bar{b}$ events and only 15% of signal events (Fig. C.8). This selection is performed only for the single prong events (one track in the signal cone).

6.2.3 Mass reconstruction specific cuts

To be able to reconstruct the Higgs boson mass (as explained below, in the Section 6.3) one has to reject the events with μ and τ jet distributed “back-to-back”, by requiring $\cos(\Delta\varphi_{\vec{p}_T, \vec{E}_T^{\text{jet}}}) > -0.9962$. This selection necessarily removes a fraction of events, since the $\cos(\Delta\varphi_{\vec{p}_T, \vec{E}_T^{\text{jet}}})$ is peaked near -1 . Additional upper cut on $\cos(\Delta\varphi_{\vec{p}_T, \vec{E}_T^{\text{jet}}}) < -0.5$ retains most of the signal, while visibly reducing the number of background events (Fig. C.9).

Finally, to get positive reconstructed Higgs boson mass, one has to reject events, where a negative neutrino energy has been reconstructed. The reconstructed energy of one or two neutrinos can be negative in the case, when the $\vec{\cancel{E}}_T$ is the outside the smaller angle $\Delta\phi$ between \vec{p}_T^μ and the $\vec{E}_T^{\tau \text{ jet}}$ (Fig. 6.3). Due to the poor missing energy direction resolution (Fig. 4.14), the fraction of such events is around 50% (Fig. 6.4).

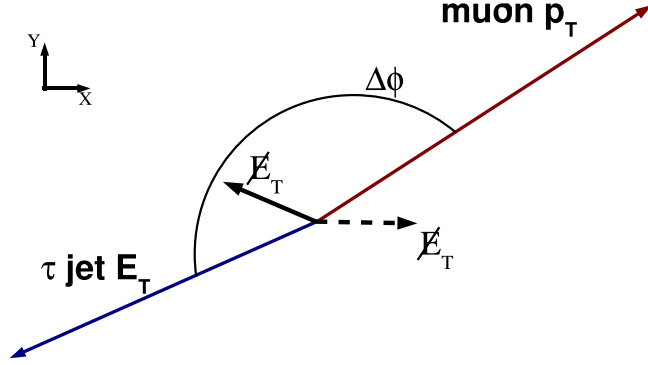


Figure 6.3: Relative orientation of the $\vec{\cancel{E}}_T$, \vec{p}_T^μ and $\vec{E}_T^{\tau \text{ jet}}$ on the XY plane. The $\vec{\cancel{E}}_T$ for which the reconstructed energy of both neutrinos is positive is marked by solid arrow. The $\vec{\cancel{E}}_T$ for which the reconstructed energy of one neutrino is negative is marked by dashed arrow.

6.2.4 Thresholds optimization

The thresholds values have been optimized by maximization of the signal significance as the function of the threshold value. The Monte Carlo event sample with $m_A = 200 \text{ GeV}/c^2$ was used for the signal reference. The events were counted in the mass window $159 < m_{\tau\tau} < 241 \text{ GeV}/c^2$. The mass window width was set by the Gaussian fit width (Section 6.3). The thresholds were optimized only for the $m_A = 200 \text{ GeV}/c^2$ due to the very low Monte Carlo statistics for the background in the mass window for the $m_A = 500 \text{ GeV}/c^2$. Figures in the Appendix E show the significance as the function of the threshold value for all optimized selections. The optimization was done using limited Monte Carlo events statistics, therefore due to statistical fluctuations an artificial peaks appeared for some variables. That was the case for the $\tau - \text{jet } E_T$ (Fig. E.2), leading track p_T in the single prong events (Fig. E.4) and $\cos(\Delta\varphi_{\vec{p}_T, \vec{E}_T^{\tau \text{ jet}}})$ (Fig. E.6), selections. Where it was possible, a conclusion on the threshold was made without considering the artificial peaks. Based on Figure C.4 a threshold of $20 \text{ GeV}/c$ was set for the leading

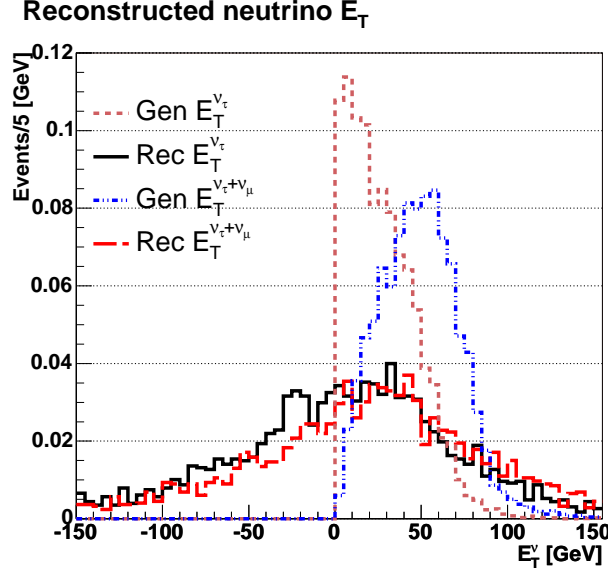


Figure 6.4: Reconstructed and generated transverse energy of the neutrinos from τ decays. Only events passing the $\cos(\Delta\varphi_{\vec{p}_T, \vec{E}_T^{\text{jet}}})$ selection contribute to the histogram.

track p_T in the three prong events. After the optimization there were no MC events left for the $b\bar{b}$ process, with one event weight equal to 12. Due to low statistics, the current optimization results can be treated only as an indication, and the optimization should be repeated with higher statistics for the background processes.

Two selections criteria – the τ – jet leading track p_T and the upper limit on the $\cos(\Delta\varphi_{\vec{p}_T, \vec{E}_T^{\text{jet}}})$, were used with the non optimized thresholds. The threshold of 10 GeV/c was used for the leading track in the single prong events instead of no threshold suggested by the optimization procedure. The value of -0.5 was used as the upper limit on the $\cos(\Delta\varphi_{\vec{p}_T, \vec{E}_T^{\text{jet}}})$ instead of no threshold preferred by the optimization procedure. These values provide additional benefits (Fig. 6.5 and 6.6):

- the Z peak is significantly reduced – although the Z peak is below the interesting mass range it may happen that in the case of jet and missing transverse energy resolution worse than that used in the simulation, events from the Z^0 peak will migrate into the interesting region thus, decreasing the discovery significance;
- the non $t\bar{t}$ background contribution is reduced, and the $t\bar{t}$ remains the most important background after the Z background – having one main

background makes the evaluation of this background from the data easier, and reduces the number of sources of the systematic error.

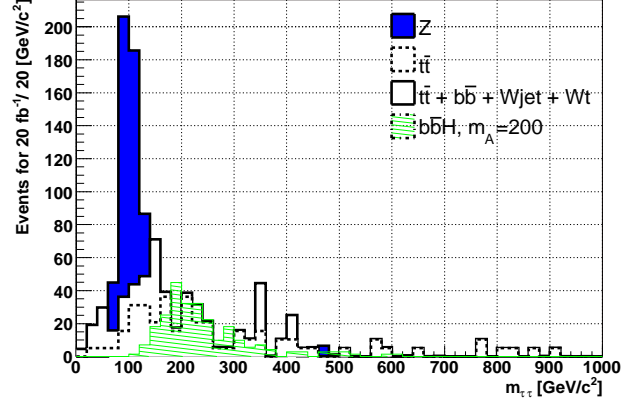


Figure 6.5: Mass distribution for the signal with $m_A = 200 \text{ GeV}/c^2$ and all background sources, after all offline selections for the thresholds optimized in the mass window $159 < m_{\tau\tau} < 241 \text{ GeV}/c^2$.

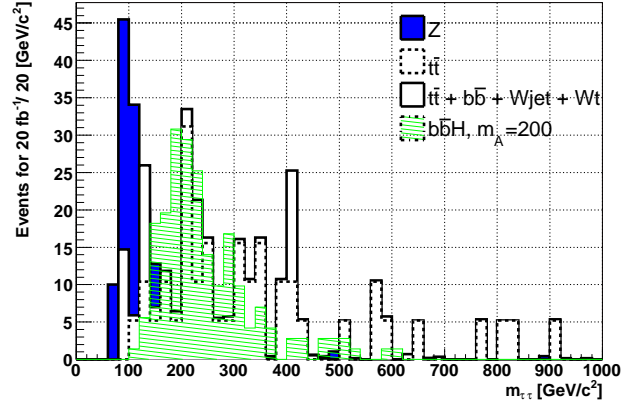


Figure 6.6: Mass distribution for the signal with $m_A = 200 \text{ GeV}/c^2$ and all background sources, after all offline selections for the thresholds optimized in the mass window $159 < m_{\tau\tau} < 241 \text{ GeV}/c^2$, except the leading track p_T for single prong events, and the upper cut on the $\cos(\Delta\varphi_{\vec{p}_T, \vec{E}_T^{\text{jet}}})$.

6.2.5 Efficiencies

After all selections the total efficiency for the signal is $1.66 \cdot 10^{-3}$ for $m_A = 200 \text{ GeV}/c^2$ and $4.53 \cdot 10^{-3}$ for $m_A = 500 \text{ GeV}/c^2$ (Tab. 6.1). Tables 6.2 and 6.3 show the ef-

6.3 Higgs boson mass reconstruction

iciencies for the background events. Two main background processes: $(b\bar{b})Z/\gamma^*$ and $t\bar{t}$ remain after all offline selections.

Tables F.6, F.7 and F.8 – F.11 of Appendix F show the details of the offline selection for the signal and the background events.

Table 6.1: Summary of the selection procedure for the signal processes. For the events with $m_A = 200$ and $300 \text{ GeV}/c^2$, $\tan(\beta) = 20$ is assumed. For the events with $m_A = 500 \text{ GeV}/c^2$, $\tan(\beta) = 30$ is assumed.

Sample	$bbH(200)$	$H(200)$	$bbH(300)$	$bbH(500)$	$H(500)$
Cross section \cdot BR [pb]	9.12	2.17	1.87	$4.51 \cdot 10^{-1}$	$7.73 \cdot 10^{-2}$
Events for 20 fb^{-1}	$1.82 \cdot 10^5$	$4.33 \cdot 10^4$	$3.75 \cdot 10^4$	$9.03 \cdot 10^3$	$1.55 \cdot 10^3$
Preselection eff	$9.47 \cdot 10^{-2}$	$9.12 \cdot 10^{-2}$	$1.31 \cdot 10^{-1}$	$1.65 \cdot 10^{-1}$	$1.58 \cdot 10^{-1}$
HLT eff (wrt. pres.)	$4.17 \cdot 10^{-1}$	$3.81 \cdot 10^{-1}$	$4.27 \cdot 10^{-1}$	$4.99 \cdot 10^{-1}$	$4.51 \cdot 10^{-1}$
Offline eff (wrt HLT)	$4.21 \cdot 10^{-2}$	$5.77 \cdot 10^{-3}$	$3.54 \cdot 10^{-2}$	$5.52 \cdot 10^{-2}$	$1.11 \cdot 10^{-2}$
Total efficiency	$1.66 \cdot 10^{-3}$	$2.01 \cdot 10^{-4}$	$1.97 \cdot 10^{-3}$	$4.53 \cdot 10^{-3}$	$7.90 \cdot 10^{-4}$
Rate after HLT [Hz]	$7.21 \cdot 10^{-4}$	$1.51 \cdot 10^{-4}$	$2.09 \cdot 10^{-4}$	$7.41 \cdot 10^{-5}$	$1.10 \cdot 10^{-5}$
Events for 20 fb^{-1}	303 ± 24	9 ± 2	74 ± 8	41 ± 3	1.22 ± 0.17

Table 6.2: Summary of the selection procedure for the background processes. The cross section and the number of events for $b\bar{b}$ sample includes a normalization factor 7 to account for the total Minimum Bias rate after the HLT selection, described in the Appendix B.

Sample	$t\bar{t}$	Wj	Wt	$b\bar{b}$
Cross section \cdot BR [pb]	$8.40 \cdot 10^2$	$4.15 \cdot 10^4$	$6.20 \cdot 10^1$	$2.29 \cdot 10^7$
Events for 20 fb^{-1}	$1.68 \cdot 10^7$	$8.29 \cdot 10^8$	$1.24 \cdot 10^6$	$4.58 \cdot 10^{11}$
Preselection eff	$9.01 \cdot 10^{-2}$	$1.44 \cdot 10^{-2}$	$6.58 \cdot 10^{-2}$	$7.56 \cdot 10^{-4}$
HLT eff (wrt. pres.)	$9.61 \cdot 10^{-2}$	$4.16 \cdot 10^{-2}$	$1.05 \cdot 10^{-1}$	$2.36 \cdot 10^{-4}$
Offline eff (wrt HLT)	$1.78 \cdot 10^{-3}$	$5.53 \cdot 10^{-5}$	$2.41 \cdot 10^{-3}$	$4.41 \cdot 10^{-4}$
Total efficiency	$1.54 \cdot 10^{-5}$	$3.31 \cdot 10^{-8}$	$1.66 \cdot 10^{-5}$	$7.86 \cdot 10^{-11}$
Rate after HLT [Hz]	$1.45 \cdot 10^{-2}$	$4.96 \cdot 10^{-2}$	$8.57 \cdot 10^{-4}$	$8.17 \cdot 10^{-3}$
Events for 20 fb^{-1}	259 ± 37	27 ± 19	21 ± 2	36 ± 25

6.3 Higgs boson mass reconstruction

6.3.1 The method

The Higgs boson mass is reconstructed using the assumption that the τ decay products, including neutrinos, are emitted collinear with the τ leptons. This

Table 6.3: Summary of the selection procedure for the Z/γ^* background processes.

	$Z/\gamma^* \rightarrow \tau\tau \rightarrow \mu + \tau_{jet} + \nu$	
	$40 < m_{\tau\tau} < 120 \text{ GeV}/c^2$	$m_{\tau\tau} > 120 \text{ GeV}/c^2$
Cross section \cdot BR [pb]	$4.63 \cdot 10^2$	4.88
Events for 20 fb^{-1}	$9.26 \cdot 10^6$	$9.77 \cdot 10^4$
Preselection eff	$6.56 \cdot 10^{-2}$	$2.14 \cdot 10^{-1}$
HLT eff (wrt. pres.)	$1.03 \cdot 10^{-1}$	$2.77 \cdot 10^{-1}$
Offline eff (wrt HLT)	$1.94 \cdot 10^{-3}$	$2.95 \cdot 10^{-3}$
Total efficiency	$1.31 \cdot 10^{-5}$	$1.75 \cdot 10^{-4}$
Rate after HLT [Hz]	$6.27 \cdot 10^{-3}$	$5.78 \cdot 10^{-4}$
Events for 20 fb^{-1}	122 ± 27	17 ± 2

Table 6.4: Summary of the selection procedure for the $b\bar{b}Z$ background processes.

	$b\bar{b}(Z \rightarrow \tau\tau)$	
	$60 < m_{\tau\tau} < 100 \text{ GeV}/c^2$	$m_{\tau\tau} > 100 \text{ GeV}/c^2$
Cross section \cdot BR [pb]	$2.61 \cdot 10^1$	1.05
Events for 20 fb^{-1}	$5.23 \cdot 10^5$	$2.10 \cdot 10^4$
Preselection eff	1.00	1.00
HLT eff (wrt. pres.)	$4.10 \cdot 10^{-3}$	$1.21 \cdot 10^{-2}$
Offline eff (wrt HLT)	$1.62 \cdot 10^{-2}$	$2.28 \cdot 10^{-2}$
Total efficiency	$6.64 \cdot 10^{-5}$	$2.76 \cdot 10^{-4}$
Rate after HLT [Hz]	$2.15 \cdot 10^{-4}$	$2.53 \cdot 10^{-5}$
Events for 20 fb^{-1}	35 ± 8	6 ± 1

approximation is good for relativistic taus. Taus from the Higgs boson decay in the interesting mass range $m_A \geq 200 \text{ GeV}/c^2$ have the Lorentz factor $\gamma \geq m_A/(2 \cdot m_\tau) \geq 59$, which is large enough to use the collinear approximation. The distance $\Delta R = \sqrt{\Delta\eta^2 + \Delta\phi^2}$ between neutrinos and charged objects: the τ lepton or its charged decay products both at the generator and the reconstruction levels is shown in Figure 6.7. The distance between the neutrino and the τ decay product, e.g. muon is roughly twice as large as the distance between the neutrino and the τ itself, but still it is relatively small.

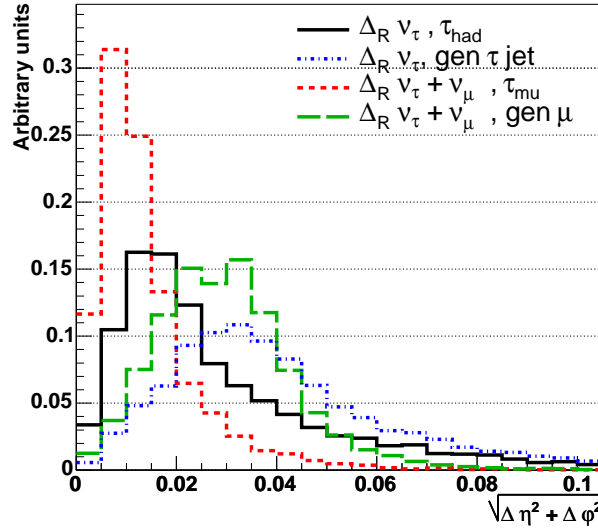


Figure 6.7: Delta R between the neutrino and the generated charged particles, for $m_A = 200 \text{ GeV}/c^2$. The distance between the neutrino and the τ decay products, e.g. muon is roughly twice as large as the distance between the neutrino and the τ itself due to the momentum conservation in the τ rest frame.

The neutrino transverse energy is reconstructed by projecting the transverse missing energy on the \vec{p}_T^μ and $\vec{E}_T^{\tau \text{ jet}}$ directions. The third, longitudinal, component is reconstructed with the use of the pseudorapidity of the charged objects. Defining the μ and τ – jet transverse directions:

$$\hat{e}_{T\tau \text{ jet}} = \frac{\vec{p}_T^{\tau \text{ jet}}}{p_T^{\tau \text{ jet}}} \quad (6.1)$$

$$\hat{e}_{T\mu} = \frac{\vec{p}_T^\mu}{p_T^\mu} \quad (6.2)$$

$$\cos(\varphi_{\mu-\tau \text{ jet}}) = \hat{e}_{T\tau \text{ jet}} \cdot \hat{e}_{T\mu} \quad (6.3)$$

one gets the following formulas for the neutrinos energies (momenta of the τ and

the muon neutrino on the muon side are summed up):

$$E_{\nu_1}^\tau = \vec{\cancel{E}}_T \cdot \frac{\hat{e}_{T\tau \text{ jet}} - \hat{e}_{T\mu} \cdot \cos(\varphi_{\mu-\tau \text{ jet}})}{\sin(\theta_{\tau \text{ jet}}) \cdot (1 - \cos^2(\varphi_{\mu-\tau \text{ jet}}))} \quad (6.4)$$

$$E_{\nu_2}^\tau = \vec{\cancel{E}}_T \cdot \frac{\hat{e}_{T\mu} - \hat{e}_{T\tau \text{ jet}} \cdot \cos(\varphi_{\mu-\tau \text{ jet}})}{\sin(\theta_\mu) \cdot (1 - \cos^2(\varphi_{\mu-\tau \text{ jet}}))} \quad (6.5)$$

6.3.2 Impact of the \cancel{E}_T measurement

The missing energy measurement is crucial for the Higgs boson mass reconstruction. The reconstructed Higgs boson for the generated mass $m_A = 200 \text{ GeV}/c^2$ is shown in Figure 6.8. The mass was calculated using the reconstructed muon and τ jet, but with the missing energy taken from the Monte Carlo information. The $\vec{\cancel{E}}_T$ was taken either as a sum of transverse momenta of all stable particles in the hadronic calorimeter η coverage ($|\eta| < 5.0$), or as a sum of the transverse momenta of the three neutrinos coming from the τ decays. The sum of Gauss

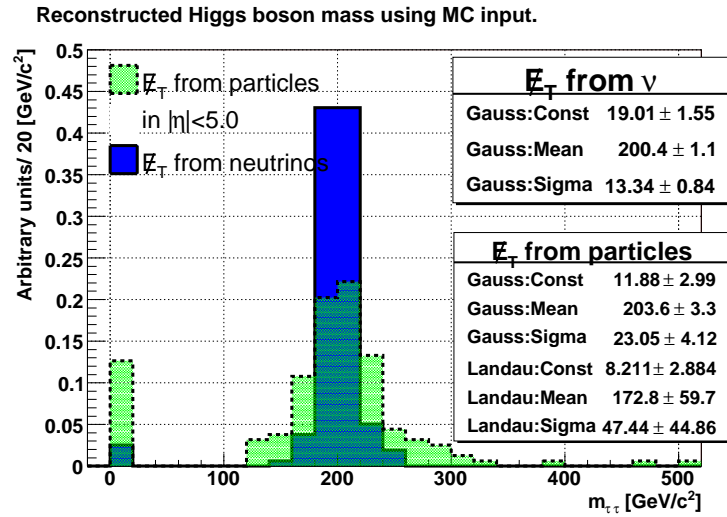


Figure 6.8: Comparison of the Higgs boson mass distributions reconstructed using the missing \cancel{E}_T taken as a sum of the transverse momenta of all stable particles, including neutrals, with $|\eta| < 5.0$ or as the sum of the three neutrinos from the τ decay. The bar at bin zero shows the fraction of events where at least one of the reconstructed neutrinos had a negative energy.

and Landau functions was used to fit the reconstructed mass distribution. The fit was performed with the MINUIT implemented in C++ in the ROOT package [73]. When the missing transverse energy experimentally possible to measure, that is within the detectors acceptance, $|\eta| < 5.0$, is used the mass resolution decreases. The distribution width (defined as the width of the Gaussian part of the fitted function) increases from 13 to 23 GeV/c^2 (see fit parameters in Figure 6.8).

The natural Higgs boson width for $m_A = 200 \text{ GeV}/c^2$ used here is of the order of 1 GeV (Fig. 3.5). The missing E_T calculated using generated particles in

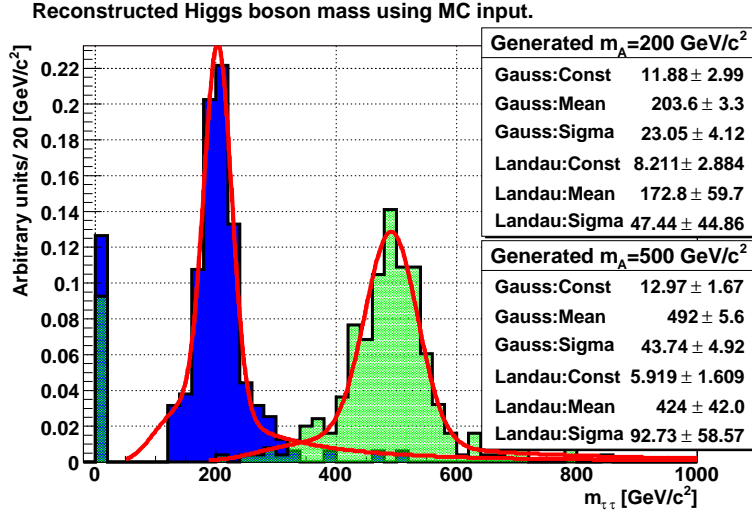


Figure 6.9: Reconstructed Higgs boson mass in the limit of the ideal \vec{E}_T reconstruction. The mass calculation is done using the reconstructed muon and τ jet. For the \vec{E}_T the sum of the transverse momenta of all, generated, stable particles with $|\eta| < 5.0$ was used. The bar at bin zero shows the fraction of events where at least one of reconstructed neutrinos had a negative energy. Distributions for $m_A = 200$ and $500 \text{ GeV}/c^2$ are shown. The fitted functions are sums of Gauss and Landau distributions.

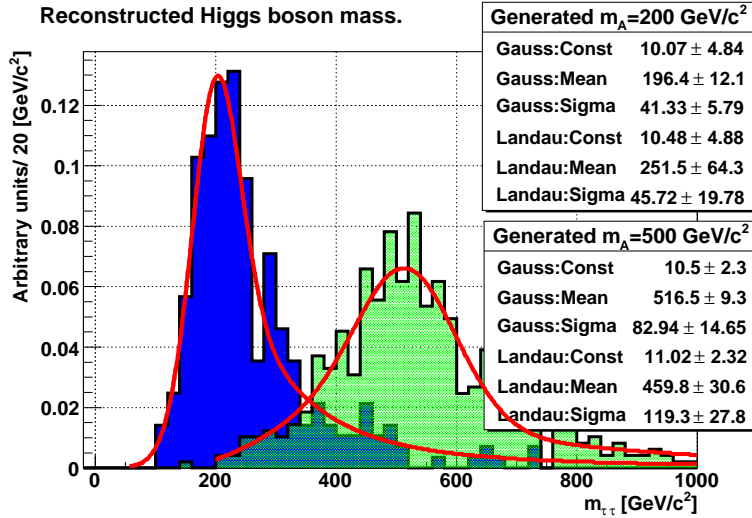


Figure 6.10: The reconstructed Higgs boson mass. The mass calculation is done using the measured muon, τ jet and \vec{E}_T . Distributions for $m_A = 200$ and $500 \text{ GeV}/c^2$ are shown. The fitted functions are sums of Gauss and Landau distributions.

$|\eta| < 5.0$ can be considered as a ideal limit for the perfect $\vec{\cancel{E}}_T$ reconstruction in detector fiducial volume. Additional decrease of the mass resolution is caused by usage of the reconstructed $\vec{\cancel{E}}_T$ instead of the $\vec{\cancel{E}}_T$ calculated from the Monte Carlo information. If one uses the reconstructed $\vec{\cancel{E}}_T$ the mass distribution is wider by a factor of ~ 2 than the ideal limit (see Gauss width fit results in Figures 6.9 and 6.10).

Table 6.5 summarizes the fitted values of the mass and the width for the two generated masses Higgs boson masses.

Table 6.5: Mass reconstruction resolution for the two Higgs boson masses.

Generated Higgs boson mass [GeV/c ²]	200	500
Fitted mass [GeV/c ²]	196	517
Gaussian fit width [GeV/c ²]	41	83
Ratio Γ/m	0.21	0.16

6.4 Background contribution estimates

6.4.1 The non Z background process

After all offline selections there are two main background processes: the $(b\bar{b})Z/\gamma^* \rightarrow \tau\tau \rightarrow \mu + \tau \text{ jet} + X$ and the $t\bar{t}$. A relatively pure sample of the $t\bar{t}$ can be selected with the inversion of the electron veto selection: requirement for the $f = E_{\text{HCAL}}/p_{\text{leading tk}} < 0.1$ instead of $0.2 < f < 1.1$ rejects more than 95% of all processes except the single and pair top production, and keeps more than 50% of the top events (Fig. C.8). The $\tau\tau$ invariant mass distribution for the above selection is presented in Figure 6.11. The number of the non Z background (mainly the $t\bar{t}$) events can be estimated using the measured number of events in the $m_{\tau\tau}$ window with $E_{\text{HCAL}}/p_{\text{leading tk}} < 0.1$ and all other offline selections, and then using the $E_{\text{HCAL}}/p_{\text{leading tk}}$ selection efficiency translated to the number of events in the $m_{\tau\tau}$ window with $0.2 < E_{\text{HCAL}}/p_{\text{leading tk}} < 1.1$ and all other offline selections:

$$N_{\text{window}}^{0.2 < f < 1.1} = N_{\text{window}}^{f < 0.1} \cdot \frac{\epsilon_{t\bar{t}}^{0.2 < f < 1.1}}{\epsilon_{t\bar{t}}^{f < 0.1}} \quad (6.6)$$

Event counting in the mass window shows that there are 367 events, with the following decomposition on the specific processes: $367 = 296_{t\bar{t}} + 39_{\text{other bkg.}} + 5_Z + 27_H$ for the $E_{\text{HCAL}}/p_{\text{leading tk}} < 0.1$, and 284 for the $0.2 < E_{\text{HCAL}}/p_{\text{leading tk}} < 1.1$: $284 = 64_{t\bar{t}} + 21_{\text{other bkg.}} + 55_Z + 144_H$. The efficiencies ratio for the $t\bar{t}$ background

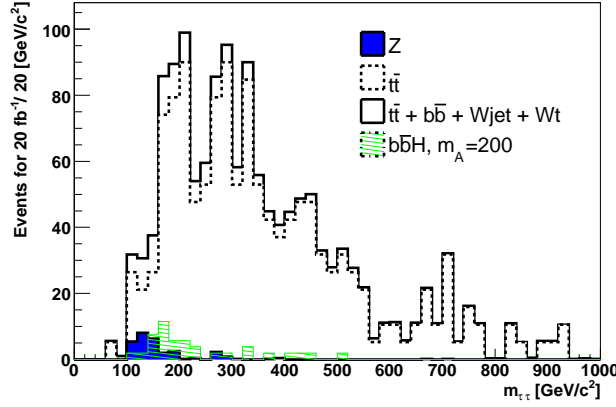


Figure 6.11: Reconstructed $\tau\tau$ invariant mass after all offline selections for $f < 0.1$.

for the both selections is 0.22 ± 0.07 . Assuming that the above procedure estimates the number of all background processes except the Z one, the estimate of the non Z background is:

$$367 \cdot 0.22 = 81 \quad (6.7)$$

and counting no Higgs events:

$$340 \cdot 0.22 = 75 \quad (6.8)$$

It is assumed that the $t\bar{t}$ mass distributions are similar for the $E_{\text{HCAL}}/p_{\text{leading } t\bar{t}} < 0.1$ and $0.2 < E_{\text{HCAL}}/p_{\text{leading } t\bar{t}} < 1.1$ selections. A detailed check of the distributions similarity for the mass spectrum can not be done due to the low number of MC events for the $0.2 < E_{\text{HCAL}}/p_{\text{leading } t\bar{t}} < 1.1$ selection. The systematic uncertainty on the number of the non Z background events has two main contributions:

- $E_{\text{HCAL}}/p_{\text{leading } t\bar{t}}$ selection efficiency uncertainty is expected to be of order of the jet energy scale variation, which is expected to be 3% [52];
- shape uncertainty – The estimated number of events is 81. This is 95% of the total non Z background, which is $85 = 64_{t\bar{t}} + 7_{Wt} + 14_{Wj}$, and 130% of the $t\bar{t}$ events. If one takes the result without the Higgs events (e.g. low $\tan(\beta)$) the estimated number is 75, which is 88% of the total non-Z background, therefore a conservative contribution from the event counting is **12%**.

The contribution from other systematic uncertainties, e.g. b tagging is assumed to be small, due to the cancellation in the efficiency ratio in Eq. 6.6.

The total uncertainty on the number of the non Z background events is: $3\% \otimes 12\% = 12\%$.

6.4.2 The Z background

The mass range analyzed in this thesis is $m_{\tau\tau} > 150 \text{ GeV}/c^2$. This is the tail of the mass distributions for the Z events. With any selection procedure this tail will be contaminated by events coming from other sources, including the Higgs boson signal events. The number of events from these sources will be similar to the number of Z events, therefore it will significantly modify the shape, making estimates based on the number of Z events in this range impossible. The $\tau\tau$ mass distribution for the Z events should be therefore taken from the Monte Carlo simulations and normalized in the peak region, where the Z events can be selected with the jet veto requirement, but without the single b tag.

The Z background contains two parts: the $b\bar{b}Z$ events and the Z events without genuine b quarks in the event. The cross section for the Z production without b quarks can be measured with high precision using the $Z \rightarrow \mu\mu$ events. The measured cross section can be used to determine the number of events in the selected mass window using of the selection efficiency obtained from the MC analysis. The systematic uncertainty on the number of Z events has following main contributions:

- total cross section for the Z production uncertainty is expected to be of order of 1% [74];
- calorimetry scale uncertainty: the number of the events in the mass window $159 < m_{\tau\tau} < 251 \text{ GeV}/c^2$ varies by $\pm 6\%$ for a jet scale variations by $\pm 3\%$ and missing transverse energy scale variations of 5% (Fig. 6.12);
- misstaging uncertainty: the conservative estimate is 5%.

The total uncertainty on the number of Z events with a quark or gluon jet misstaged as a b-jet is: $1\% \otimes 6\% \otimes 5\% = 8\%$.

For the $b\bar{b}Z$ events the systematic uncertainty has following main contributions:

- total production cross section uncertainty: for the $b\bar{b}Z$ events the cross section will be measured with a precision of 14.8 %, including 5% for the luminosity uncertainty [75], therefore the uncertainty on the number of the $b\bar{b}Z$ events without the luminosity uncertainty is 14%;
- calorimetry scale uncertainty: is assumed the same as for the Z events without the genuine b quarks.

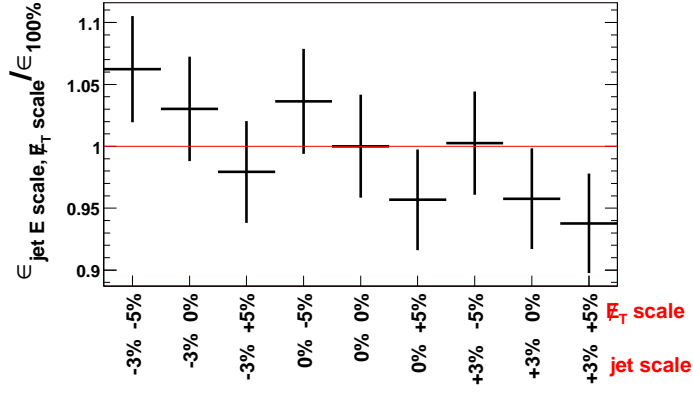


Figure 6.12: Ratio of the selection efficiency after the jet scale variation by $\pm 3\%$ and missing transverse energy scale variation by $\pm 5\%$, to the efficiency for the nominal calorimetry scale. The label of the X axis shows each scale variation, 0% means the nominal scale.

The total uncertainty on the number of the $b\bar{b}Z$ events is: $14\% \otimes 6\% = 15\%$.

The p_T spectrum of the Z boson can be estimated with high precision from the $b\bar{b}Z \rightarrow ll$ [75] and even better for the $Z \rightarrow \mu\mu$, therefore its contribution to the systematic uncertainty has been neglected.

Chapter 7

Results

7.1 Results for the m_h^{\max} scenario

The statistical significance has been obtained with the S_{c12} formula (Eq. 7.1), which from the statistical point of view gives the best results among the event counting methods [76; 77]. The S_{c12} formula is officially recommended to use by the CMS collaborators.

$$S_{c12} = 2 \cdot (\sqrt{N_s + N_b} - \sqrt{N_b + \Delta_b}) \quad (7.1)$$

The S_{c12} formula allows for the mathematically consistent inclusion of the systematic uncertainty on the number of background events Δ_b .

The number of signal and background events has been counted in a window around the generated Higgs boson mass (Fig. 7.1). The window width was set to the mass resolution defined as the width of the Gaussian part of the fit to the signal distribution only (Fig. 6.10). The events were counted in a histogram with bin width of 1 GeV/c². The histogram was filled with generated Monte Carlo events for the signal processes. Due to the low statistics for the background events, histograms filled with random numbers generated from the distributions fitted to the background spectra were used (Fig. 7.2). The histograms were filled with large number of events and then normalized to the number of events for the given luminosity. The shape for the $t\bar{t}$ process was normalised to the number of all non-Z background events. The number of events, the counting windows and the computed significances for $m_A = 200$ and 500 GeV/c² are reported in Table 7.1.

To obtain the CMS discovery reach in the $\langle m_A, \tan(\beta) \rangle$ plane the significance had been interpolated between two generated masses 200, and 500 GeV/c². The CMS reach with 20 fb⁻¹ of accumulated data, at low luminosity, with and without systematic error on the background estimate is shown in Figure 7.3.

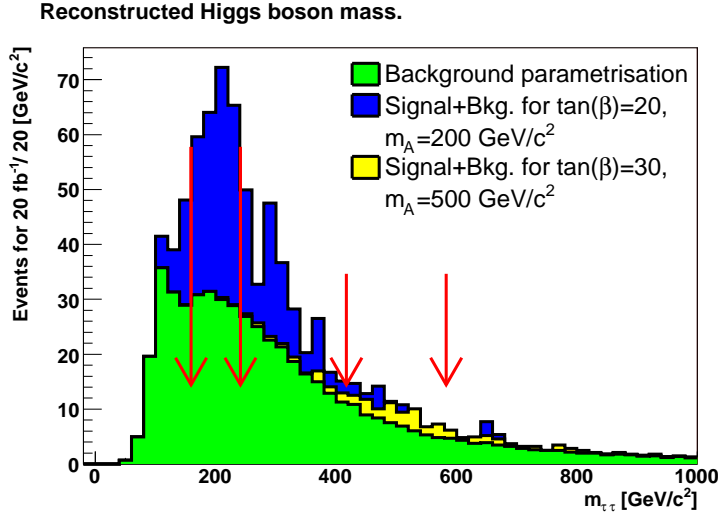


Figure 7.1: The reconstructed Higgs boson mass. The signal and the background contributions are shown. Arrows mark the mass window in which the events are counted for the significance calculations. Histograms filled from the distributions fitted to $t\bar{t}$ and Z/γ^* were used for the background. For the signal, the generated events passing all selection criteria were properly weighted.

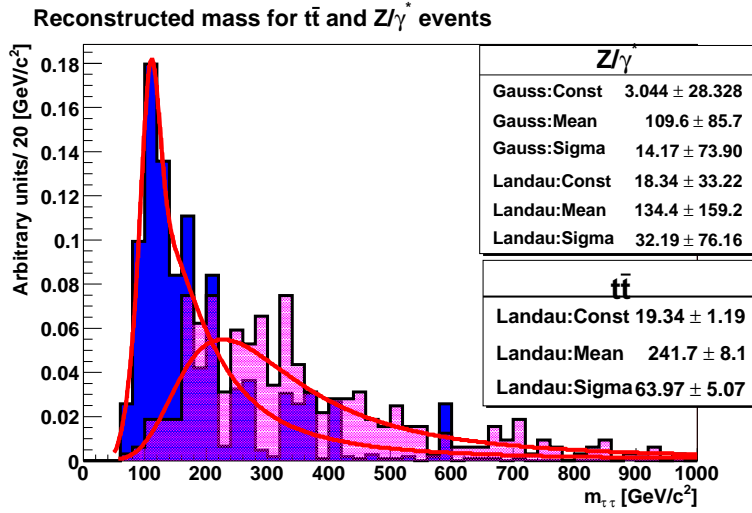


Figure 7.2: The reconstructed $\tau\tau$ mass for the two main background processes after the offline selection: Z/γ^* and $t\bar{t}$. Events passing all selections criteria except the leading track p_T cut, opposite charge of both taus and electron veto contribute to the histogram for the Z events. Only the electron veto requirement was relaxed for the $t\bar{t}$ events.

7. RESULTS

Table 7.1: Significance of the signal over background for 20 fb^{-1} . The events were counted in a histogram with bin width of $1 \text{ GeV}/c^2$.

Higgs boson mass [GeV/c^2]	$\tan(\beta)$	Mass window range [GeV/c^2]	Number of signal events	Number of back. events	S
200	20	± 41	146	127	10
500	30	± 83	21	61	2

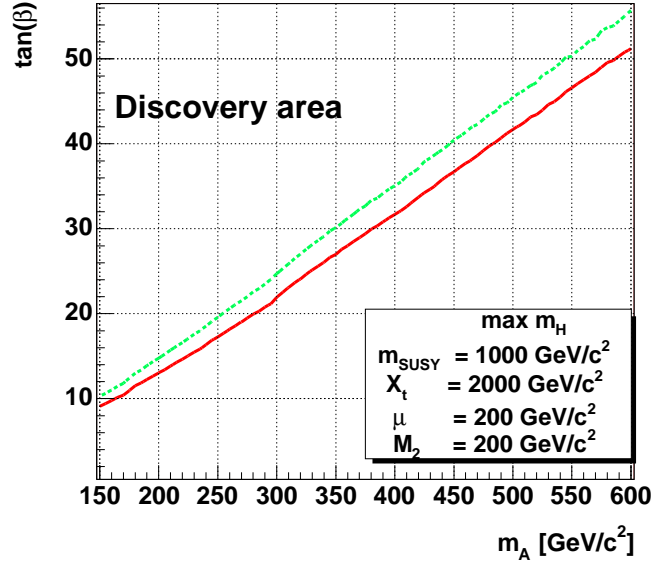


Figure 7.3: Five sigma contour in the $\langle m_A, \tan(\beta) \rangle$ plane for the 20 fb^{-1} integrated luminosity, in the maximal m_h MSSM scenario. The dashed line shows the five sigma contour calculated assuming 12% systematic error on the number of background events.

The significance interpolation procedure consisted in the following steps:

1. calculation of the $\sigma \times \text{BR}$ for the signal in bins in the $< m_A, \tan(\beta) >$ plane;
2. interpolation of the selection efficiency between masses of 200 and 500 GeV/c^2 ;
3. calculation of the number of signal events for a given bin in the $< m_A, \tan(\beta) >$ plane using the calculated cross sections and the interpolated selection efficiencies;
4. calculation of the number of background events using the formula fitted to the generated events. The number of background events was estimated as a integral in the window around the given mass. The window width was linearly interpolated between known values for $m_A = 200$ and $500 \text{ GeV}/c^2$;
5. calculation of the significance using the interpolated number of signal and background events.

7.2 Dependency on the MSSM parameters

As it was described in Section 2.4, the dominant SUSY radiative corrections to the analyzed production and decay mode of the Higgs boson are sensitive to the Higgsino mass parameter μ . Hence the discovery reach should be analyzed for various values of the μ , and for the both signs. Following suggestions of [35] the CMS discovery reach for the $gg \rightarrow b\bar{b}H/A \rightarrow \tau\tau \rightarrow \mu + \text{hadrons} + X$ search was plotted for $\mu = \pm 200, \pm 500 \text{ GeV}/c^2$ (Fig. 7.4). The best result is obtained for $\mu = -500 \text{ GeV}/c^2$, and worse for $\mu = +200 \text{ GeV}/c^2$. The difference is of order of 6 units in $\tan(\beta)$ for $m_A \sim 600 \text{ GeV}/c^2$.

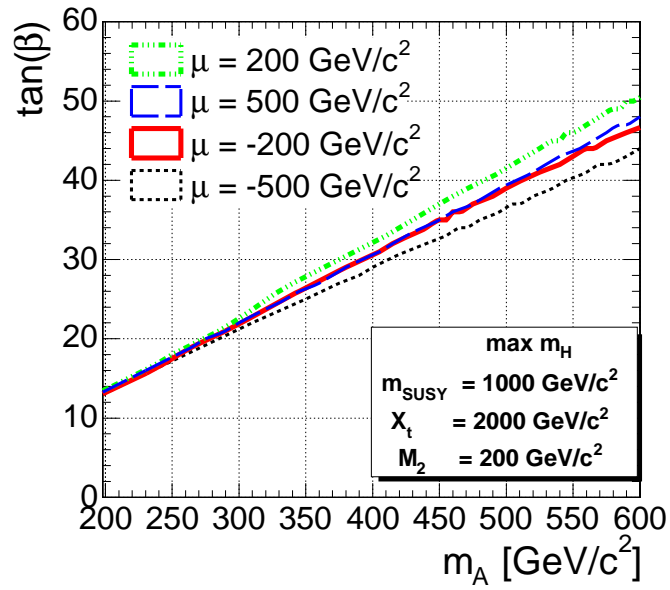


Figure 7.4: Five sigma contour, calculated assuming 12% systematic error on the number of background events. The 30 fb^{-1} integrated luminosity was assumed. The variation with the μ parameter is shown.

Chapter 8

Conclusions

The MSSM A and H Higgs bosons discovery in the $b\bar{b}(A/H \rightarrow \tau\tau \rightarrow \mu + \tau \text{ jet} + X)$ channel has been studied with full simulation, including leading systematic uncertainties. The discovery reach was evaluated for 20 and 30 fb^{-1} integrated luminosity. The study shows that it is possible to discover the heavy, neutral Higgs bosons with 20 fb^{-1} in the $\tan(\beta)$ and m_A region shown in Figure 7.3, and with 30 fb^{-1} in Figure 7.4.

The discovery limit obtained in this study can be compared with CMS limits in other channels. The search in the $\mu \tau \text{ jet}$ final state gives the best prospects for the heavy, neutral Higgs bosons, for moderate values of m_A (Fig. 8.1). At high pseudoscalar masses, $m_A \geq 500 \text{ GeV}/c^2$, the fully hadronic $\tau \text{ jet } \tau \text{ jet}$ final state gives better results [52].

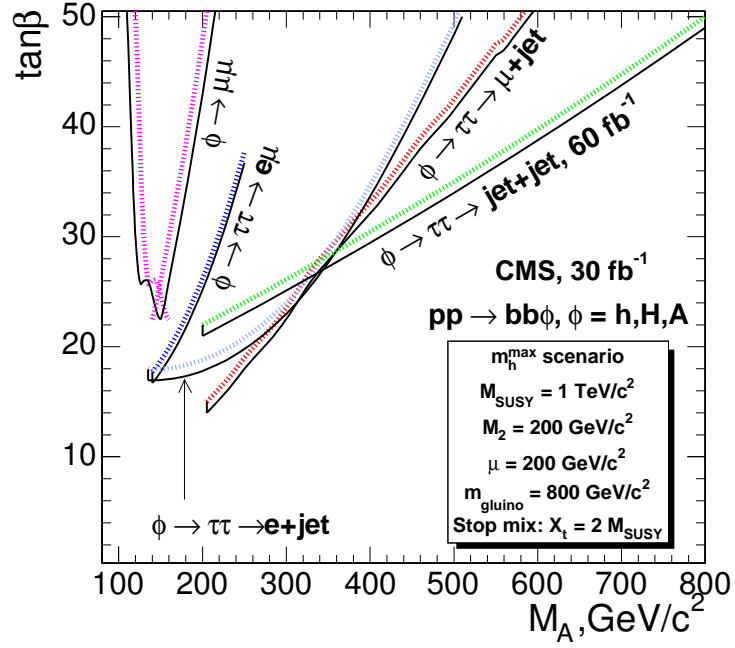


Figure 8.1: Five sigma contours, calculated including systematic error on the number of background events. Curves for the search in $\mu\mu$, $\tau\tau \rightarrow e\mu$, $\tau\tau \rightarrow \mu + \tau \text{ jet}$, $\tau\tau \rightarrow e + \tau \text{ jet}$ and $\tau\tau \rightarrow \tau \text{ jet} + \tau \text{ jet}$ are shown. The curve for $\tau \text{ jet} + \tau \text{ jet}$ was plotted for 60 fb^{-1} of integrated luminosity. Other curves were plotted for 30 fb^{-1} [78].

Appendices

Appendix A

Comparison between MCFM and PYTHIA for the $gb \rightarrow bh$ and $gg \rightarrow b\bar{b}h$ processes at the LHC

A.1 Introduction

An accurate generation of the $gb \rightarrow bh$ and $gg \rightarrow b\bar{b}h$ processes is crucial both for the measurement of the MSSM $gg \rightarrow b\bar{b}h$, $h \rightarrow 2\tau$ cross section and for constraining $\tan(\beta)$ from event-counting at the LHC [79]. The production of a MSSM Higgs boson in association with b quarks is the dominant production process at high $\tan(\beta)$ and for $M_h > 150\text{-}200 \text{ GeV}/c^2$. The CMS experimental selections include single b-tagging, a veto on the other jets in the event (excluding τ jets), a cut on the angle between the two τ leptons in the transverse plane and a cut on the reconstructed mass of the τ -lepton pair using the missing transverse energy. Thus, the correct generation of the pseudorapidity and p_T of the b quarks and the Higgs boson is very important.

In PYTHIA [44], both the $gb \rightarrow bh$ ($2 \rightarrow 2$) and $gg \rightarrow b\bar{b}h$ ($2 \rightarrow 3$) processes are available, each of which produces a $b\bar{b}h$ final state. In the $gb \rightarrow bh$ process the second b quark (\bar{b}) comes from the gluon splitting ($g \rightarrow b\bar{b}$) in the initial state parton shower and is always present in the PYTHIA event.

In this Appendix a comparison of the PYTHIA $2 \rightarrow 2$ and $2 \rightarrow 3$ processes with the next-to-leading order (NLO) calculations implemented in the MCFM program [80]. The NLO calculations in MCFM start from the leading order (LO) $gb \rightarrow bh$ process, with the LO $gg \rightarrow b\bar{b}h$ contribution included as part of the NLO calculation. The LO MCFM calculations were also compared with the PYTHIA $2 \rightarrow 2$ process when both the initial and final state radiation were switched off.

A.2 Simulation setup

The kinematic distributions were compared for two values of the Higgs boson mass, $m_h=200$ and $500 \text{ GeV}/c^2$. PYTHIA 6.227 was used to generate the processes $gg \rightarrow b\bar{b}h$ (MSUB(121)=1, KFPR(121,2)=5) and $gb \rightarrow bh$ (MSUB(32)=1) with gluon and b quark as incoming partons). The CTEQ6L1 PDF was used with the renormalization and the factorization scales equal and set to $\mu_R = \mu_F = (m_h + 2m_b)/4$. The primordial parton k_T was switched off in PYTHIA (MSTP(91)=0). To reduce the CPU time, the fragmentation, decays and multiple interactions were switched off in PYTHIA (MSTP(111)=0, MSTP(81)=0). For the $gb \rightarrow bh$ process, a lower cut of $20 \text{ GeV}/c$ was set on the p_T of the outgoing partons in the rest frame of the hard interaction (CKIN(3)=20 in PYTHIA). The jets were reconstructed from the partons using the simple cone algorithm with a cone size of 0.7.

A.3 Comparison of PYTHIA and MCFM at leading order

The distributions for the $gb \rightarrow bh$ process in PYTHIA and LO MCFM were compared. The initial and the final state radiation in PYTHIA was switched off, so that a direct comparison of the LO matrix element implementation in PYTHIA and MCFM could be performed. The distributions of the b quark p_T and the Higgs boson mass are shown in Figures A.1 and A.2 respectively, for $m_h=500 \text{ GeV}/c^2$. The dashed line shows the PYTHIA distributions, whereas the dotted line shows the MCFM distributions. There is a clear difference between the PYTHIA and MCFM curves. The dominant reason is that, in PYTHIA the matrix elements make use of the kinematic relation $s + t + u = m_h^2$. In contrast, MCFM uses $s + t + u = Q^2$, where Q^2 is the virtuality of the Higgs boson. This is the appropriate form to use when the Higgs boson is allowed off-shell using the Breit-Wigner approximation; it gives rise to a large discrepancy when the Higgs boson is very far off-shell (for instance, $Q^2 \gg m_h^2$). Corrections to the PYTHIA matrix elements were made by substituting Q^2 for m_h^2 where appropriate¹ and the solid lines in Figures A.1 and A.2 reflect the PYTHIA results after this change. With the corrected matrix elements the discrepancy between PYTHIA and MCFM is significantly reduced. The remaining difference in the Higgs boson mass distribution is due to the different treatment of the Higgs boson propagator. MCFM uses the fixed width approach, whereas PYTHIA uses a width which is

¹ Thanks to T. Sjöstrand for providing the fixed matrix element.

dependent on Q^2 . In particular, the drop near $160 \text{ GeV}/c^2$ corresponds to the closure of the WW decay channel for the Higgs boson. This calculation is most useful in the resonance region. Away from the resonance peak, once the decay of the Higgs boson is included contributions from other interfering diagrams (such as ones in which the Higgs is replaced by a Z boson) can change the shape of the prediction.

A.4 Comparison of next-to-leading order MCFM and PYTHIA

The comparison between the MCFM NLO predictions and PYTHIA was made when the initial and the final state radiation in PYTHIA was switched on. In all figures shown below the solid line represents the distribution for the PYTHIA $gb \rightarrow bh$ process generated with the corrected matrix element and $\hat{p}_T > 20 \text{ GeV}/c$, the dashed line shows the distribution for the PYTHIA $gg \rightarrow b\bar{b}h$ process and the dotted line corresponds to the MCFM $gb \rightarrow bh$ process at NLO.

The p_T distribution of the highest p_T b jet with $|\eta| < 2.4$ is shown in Figure A.3 for $m_h=200 \text{ GeV}/c^2$ and Figure A.4 for $m_h=500 \text{ GeV}/c^2$. Each of the histograms is normalized to unity in the region $p_T > 20 \text{ GeV}/c$. One sees that both PYTHIA processes show good agreement with MCFM.

The efficiency of the central jet veto (after single b tagging) depends, in particular, on the p_T and η distributions of the second (less energetic) b jet. The p_T distribution of the second b jet within $|\eta| < 2.4$ is shown in Figure A.5 for $m_h=200 \text{ GeV}/c^2$ and Figure A.6 for $m_h=500 \text{ GeV}/c^2$, after requiring that the first (most energetic) b jet be in the tagging range $p_T^{b \text{ jet}} > 20 \text{ GeV}/c$ and $|\eta^{b \text{ jet}}| < 2.4$. Once again, the histograms are normalized to unity in the region $p_T > 20 \text{ GeV}/c$. One can see that the second b jet in the PYTHIA $gb \rightarrow bh$ process is much softer than in NLO MCFM, while this calculation agrees well with the PYTHIA $gg \rightarrow b\bar{b}h$ process. This is to be expected since the second b quark (\bar{b}) in the $gb \rightarrow bh$ process is produced by the parton shower in the initial state. At high p_T one expects the $2 \rightarrow 3$ process, which is included as a NLO effect in MCFM, to provide a better description and one sees that this is indeed the case.

Figures A.7, A.8, A.9 and A.10 show the pseudorapidity distributions for the first and the second b jets for Higgs boson masses of 200 and 500 GeV/c^2 . The content of the histograms is normalized to unity in the η interval between -2 and +2. The PYTHIA distributions for the leading b jet for the Higgs boson mass of 200 GeV/c^2 agree well with the MCFM result (Figure A.7), whereas for $m_h=500$

GeV/ c^2 the MCFM η distribution is less central than in PYTHIA (Figure A.8). The second b jet in the $gb \rightarrow bh$ process is distributed in the forward/backward direction more in PYTHIA than in MCFM (Figures A.9 and A.10). This is again due to the aforementioned reason that the second b quark is produced in PYTHIA from the parton shower. The η distribution of the second b jet in the PYTHIA $gg \rightarrow b\bar{b}h$ process is close to MCFM, but there is still some difference which is more pronounced for $m_h=200$ GeV/ c^2 than for $m_h=500$ GeV/ c^2 .

The experimental selections include cuts on the visible τ -lepton energy, on the angle between the two τ leptons in the transverse plane and on the mass reconstructed from the missing transverse energy. Therefore the selection efficiency depends, in particular, on the p_T spectrum of the Higgs boson. Figures A.11 and A.12 show the Higgs boson p_T spectrum after cuts which imitate the experimental selections of single b tagging and a jet veto. These cuts require that:

- the first b jet must lie in the tagging range, $p_T^{b \text{ jet}} > 20$ GeV/ c and $|\eta^{b \text{ jet}}| < 2.4$;
- no other jets should be observed in the central region, $p_T^{\text{other jet}} < 20$ GeV/ c or $|\eta^{\text{other jet}}| > 2.4$.

Since MCFM includes the b quark as a massless particle, predictions are only available when applying a cut on the b quark p_T . By momentum balance, this means that the Higgs boson transverse momentum is constrained at LO to be greater than the jet cut of 20 GeV/ c . However, when moving to NLO, the region below this begins to be populated. This feature means that the NLO calculation does not provide reliable predictions in the close vicinity of the jet cut. Therefore we perform the comparison only for $p_T > 30$ GeV/ c and normalize the histograms in Figures A.11 and A.12 to unity in the p_T interval between 30 and 200 GeV/ c . One can see that the Higgs boson p_T spectrum calculated to NLO in MCFM is slightly softer than either PYTHIA prediction. The effect on the selection efficiency requires further study but is expected to be small.

A.5 Conclusions

A comparison of the shapes of the kinematic distributions of b quarks and the Higgs boson was performed for the PYTHIA $gb \rightarrow bh$ and $gg \rightarrow b\bar{b}h$ processes and the $gb \rightarrow bh$ process implemented at LO and NLO in MCFM. The study was performed for two masses of the Higgs boson, 200 and 500 GeV/ c^2 , which lie at either end of the interesting analysis region.

A. COMPARISON BETWEEN MCFM AND PYTHIA FOR THE $gb \rightarrow bh$ AND $gg \rightarrow bbh$ PROCESSES AT THE LHC

It was observed that the p_T spectrum of the leading b jet in the PYTHIA $gg \rightarrow b\bar{b}h$ process is in good agreement with the one obtained from the NLO MCFM $gb \rightarrow bh$ process. The PYTHIA $gb \rightarrow bh$ process leads to the second b jet being produced with a softer p_T spectrum, due to the parton shower. Neither of the two PYTHIA processes agrees exactly with the η spectrum of the b jets in the NLO MCFM $gb \rightarrow bh$ process, but the PYTHIA $gg \rightarrow b\bar{b}h$ process shows better agreement. The p_T spectrum of the Higgs boson in the PYTHIA processes is slightly harder than in NLO MCFM.

The p_T shapes for the b jet and the Higgs boson were compared for $p_T^{b \text{ jet}} > 20 \text{ GeV}/c$ and $p_T^H > 30 \text{ GeV}/c$. Since the experimental jet energy resolution for 20 GeV jets in CMS is of the order of 40%, it would be very desirable to make a comparison with NLO calculations using a much lower cut-off, for instance $\simeq 5 \text{ GeV}/c$. However, such an exercise would require further theoretical input, namely a calculation which extends the MCFM treatment to include effects due to the mass of the final state b quark.

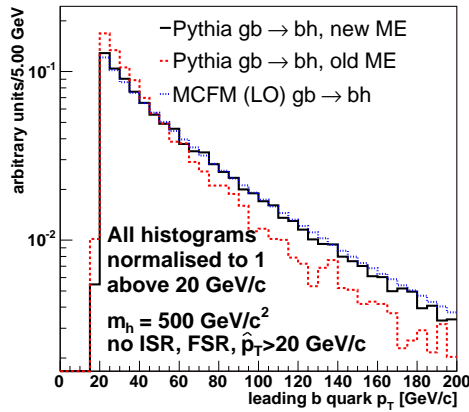


Figure A.1: The p_T of the b quark in PYTHIA and LO MCFM for $gb \rightarrow bh$ process, $m_h=500 \text{ GeV}/c^2$. See more explanations in the text.

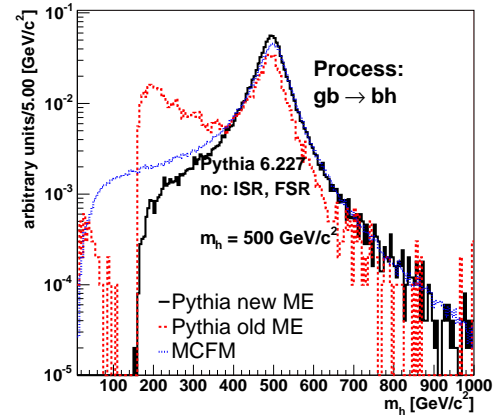


Figure A.2: The Higgs boson distribution in PYTHIA and MCFM for $m_h=500 \text{ GeV}/c^2$.

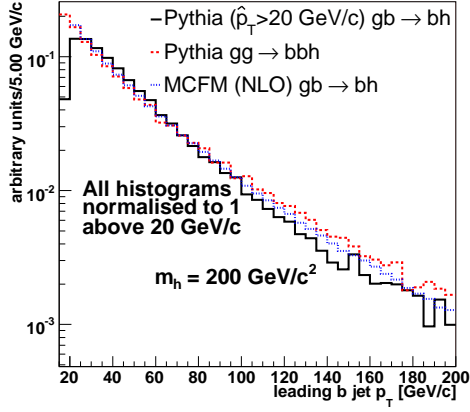


Figure A.3: The p_T of the leading b jet in PYTHIA and in MCFM for $m_h=200$ GeV/c^2 .

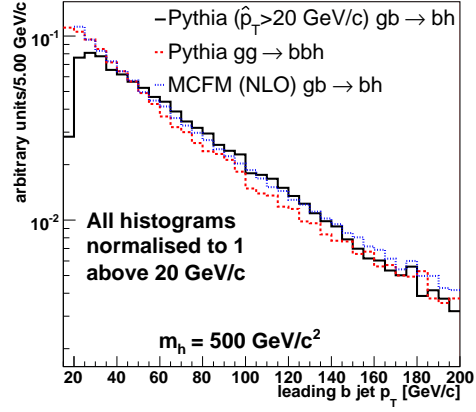


Figure A.4: The p_T of the leading b jet in PYTHIA and in MCFM for $m_h=500$ GeV/c^2 .

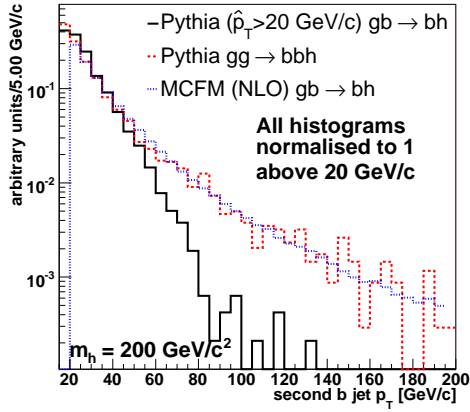


Figure A.5: The p_T of the second b jet in PYTHIA and in MCFM for $m_h=200$ GeV/c^2 .

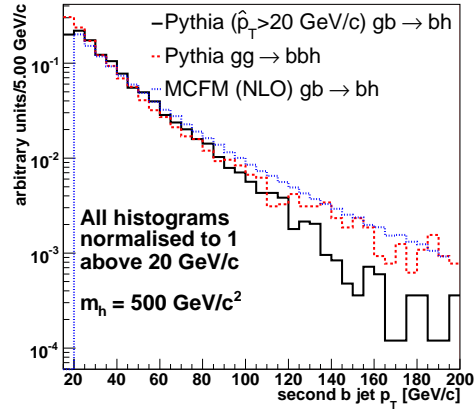


Figure A.6: The p_T of the second b jet in PYTHIA and in MCFM for $m_h=500$ GeV/c^2 .

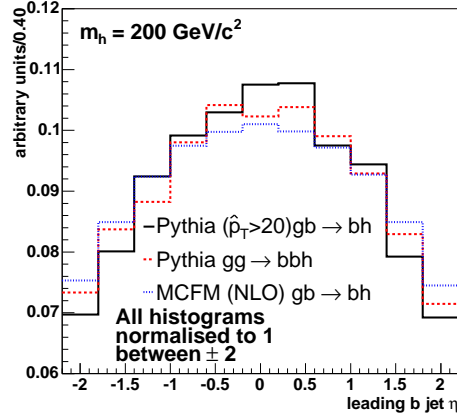


Figure A.7: The η of the leading b jet in PYTHIA and in MCFM for $m_h=200 \text{ GeV}/c^2$.

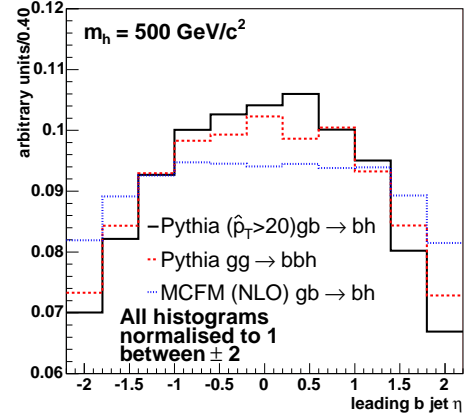


Figure A.8: The η of the leading b jet in PYTHIA and in MCFM for $m_h=500 \text{ GeV}/c^2$.

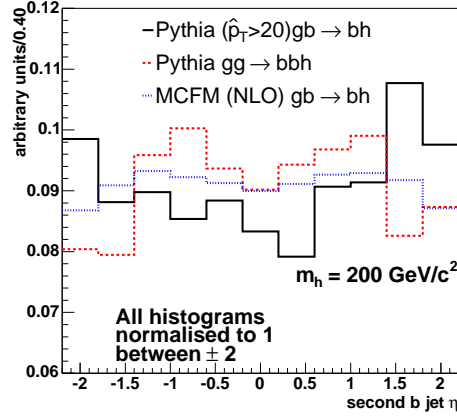


Figure A.9: The η of the second b jet in PYTHIA and in MCFM for $m_h=200 \text{ GeV}/c^2$.

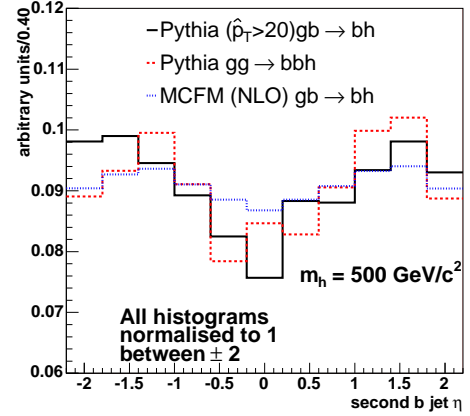


Figure A.10: The η of the second b jet in PYTHIA and in MCFM for $m_h=500 \text{ GeV}/c^2$.

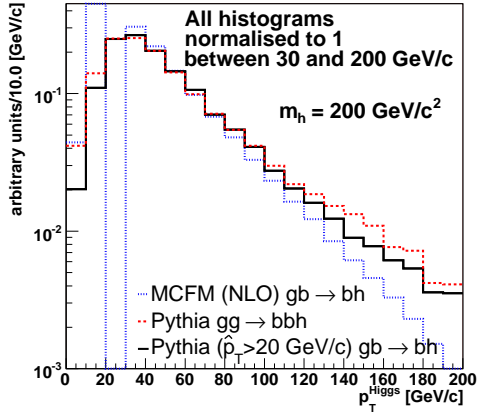


Figure A.11: The p_T of the Higgs boson for the leading b jet in the tagging range and no other jets in the central region, $m_h=200 \text{ GeV}/c^2$.

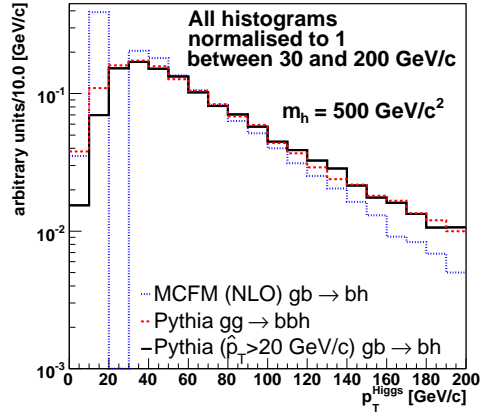


Figure A.12: The p_T of the Higgs boson for the leading b jet in the tagging range and no other jets in the central region, $m_h=500 \text{ GeV}/c^2$.

Appendix B

QCD events simulation

For the estimation of the minimum bias background the $b\bar{b}$ events were used, since this is the main source of muons in the minimum bias near the trigger and analysis muon p_T threshold $p_T^\mu > 14 \text{ GeV}/c$ [65].

The $b\bar{b}$ events can be generated in Pythia in two ways: with massive b quarks, produced with gluon ($gg \rightarrow Q\bar{Q}$) and quark ($q\bar{q} \rightarrow Q\bar{Q}$) fusion processes selected with the MSEL 5 card, or with the general QCD minbias events production, selected with the MSEL 1 card. The MSEL 1 set includes the flavor promotion ($gQ \rightarrow Qg$), and gluon splitting ($g \rightarrow Q\bar{Q}$) processes which are important at the LHC energy [44]. However only 1% of events produced with the MSEL 1 card contains b quark pair, which with the preselection efficiency of the order of 10^{-4} (Tab. 5.2) makes the generation of $b\bar{b}$ events with the MSEL 1 card very CPU time consuming. The $b\bar{b}$ events were produced with the MSEL 5 card and normalized to the total, theoretical cross section of $500 \mu\text{b}$ [46]. The muon rate for muons coming from b decays for the high luminosity ($\mathcal{L} = 10^{34} \text{ cm}^{-2}\text{s}^{-1}$) case is shown in Figure B.1. The muon rate for events produced with the MSEL 5 card is significantly softer than the rate for events produced with the MSEL 1. As the MSEL 1 includes all relevant processes, the $b\bar{b}$ event sample produced with the MSEL 5 card was normalized to the same muon rate at $15 \text{ GeV}/c$. The scale factor was $f=5.16$.

In the QCD minbias processes there are also other sources of muon than b quarks decays. These are the c, K and π decays. These sources are subdominant at muon p_T threshold of order $20 \text{ GeV}/c$. Due to the very large expected rejection factor of the general MSEL 1 set, these sources were not generated. The $b\bar{b}$ process was further renormalized to include the contribution from these sources. Earlier studies based on a large min bias event sample [81] show that, at the High Level Trigger (HLT) level, 73% of events are the $b\bar{b}$ events, and the remaining 27% come from c, K and π decays (Fig. B.2). This leads to a factor of $1/0.73 =$

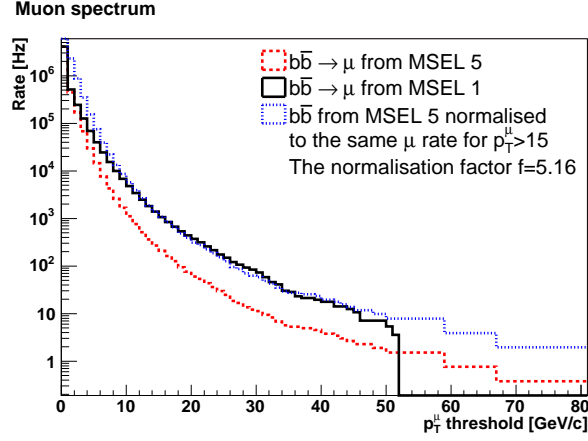


Figure B.1: Muon rate for muons coming from the b quarks. The b quarks were generated with massive Pythia processes selected with card MSEL 5, and Pythia minimum bias (MSEL 1). Both event samples were initially normalized to a total cross section of $500 \mu b$. Only muons in $|\eta| < 2.1$ are considered. Due to the limited statistics, there are no MC events for the MSEL 1 above $50 \text{ GeV}/c$.

1.37 needed to accommodate the missing processes. The total rescaling factor is $1.37 \cdot 5.16 = 7$.

For this analysis only events with the $\hat{p}_T > 20 \text{ GeV}/c$ were generated to save CPU time (Tab. 5.1). The Pythia cross section for $b\bar{b}$ events with $\hat{p}_T > 20 \text{ GeV}/c$ was $3.1 \cdot 10^6 \text{ [pb]}$, and the total Pythia cross section for $b\bar{b}$ events without any cut on the \hat{p}_T was $4.798 \cdot 10^8 \text{ [pb]}$. Therefore the total $b\bar{b}$ normalization for the events used in the analysis was: $3.1 \cdot 10^6 \cdot \frac{500}{479.8} \cdot 5.16 \cdot 1.375 = 2.29 \cdot 10^7 \text{ [pb]}$ as quoted in the Table 6.2.

The above normalization is a pessimistic one, since it assumes that the $b\bar{b}$ events from the gluon splitting and the c , K and π events have the same topology as the $b\bar{b}$ events from gluon fusion.

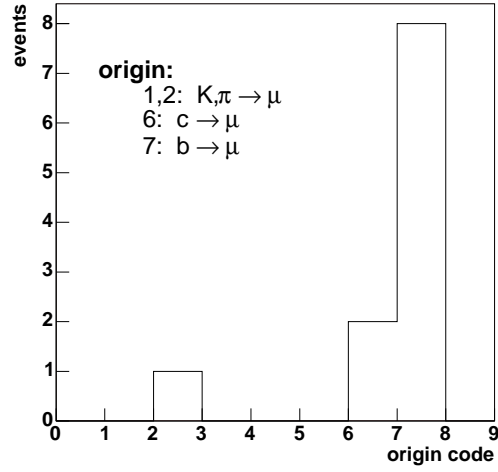


Figure B.2: The origin of muons for the events passing the $\mu\tau$ HLT selection for low luminosity. The c events come from direct c quark production. All events have the same weight [81].

Appendix C

Selection efficiencies as a function of the threshold

In this appendix integrated distributions of variables used for the rejection of background events are collected. The distributions show the state after the offline τ jet isolation. The acceptance ranges are marked by arrows.

The legend entries are ordered by the selection efficiency in the acceptance region. The top entry refers to the sample with the highest selection efficiency on the corresponding variable.

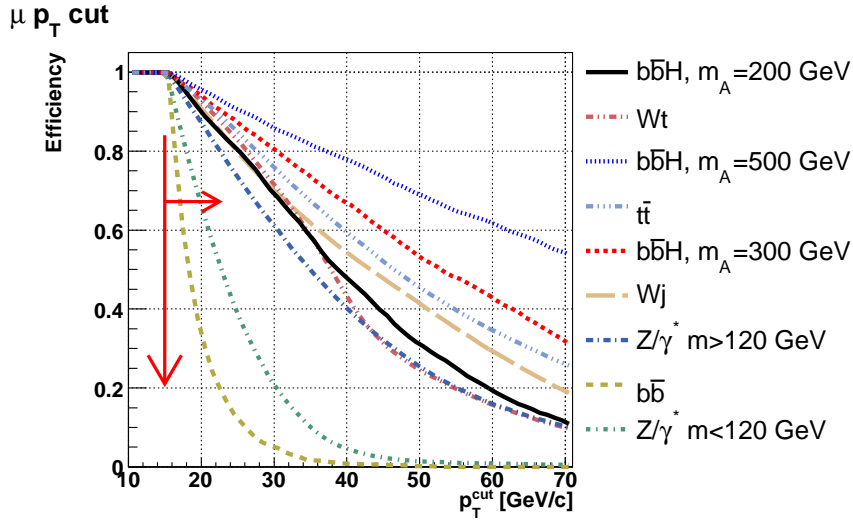


Figure C.1: Integrated distribution of μp_T .

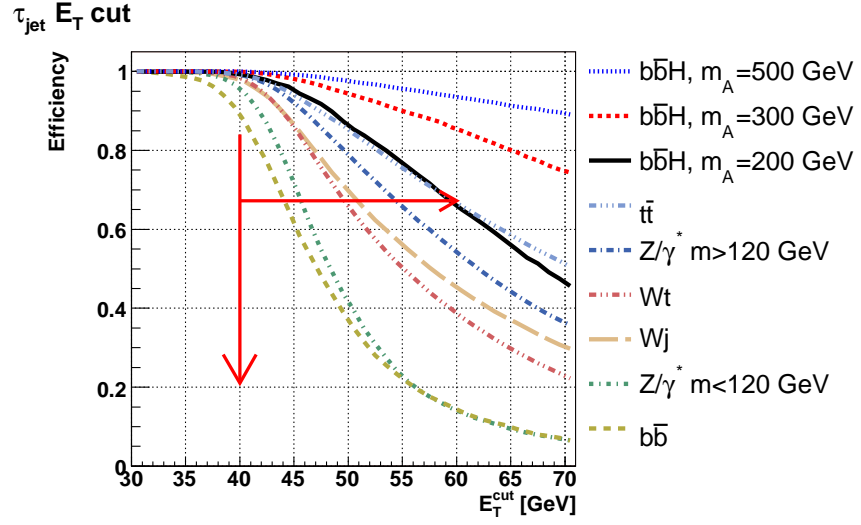


Figure C.2: Integrated distribution for τ – jet E_T .

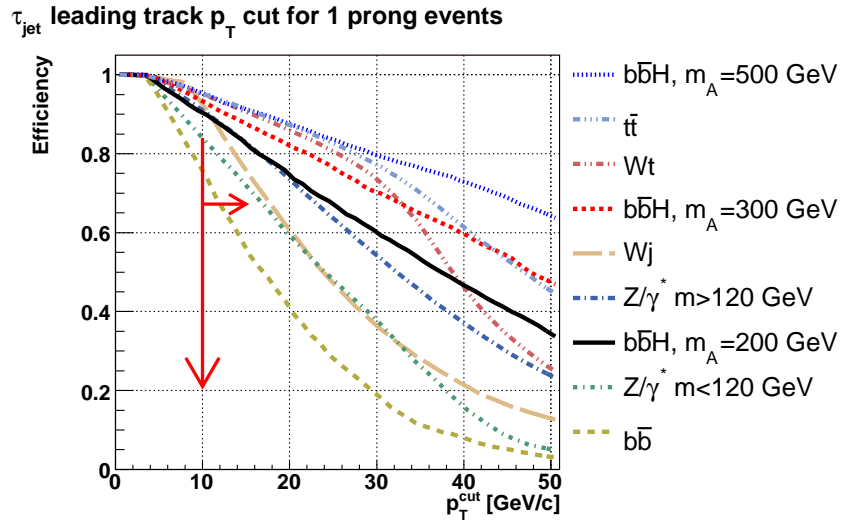


Figure C.3: The τ – jet leading track p_T integrated distribution. Only events with 1 track in the signal cone contribute to the histogram.

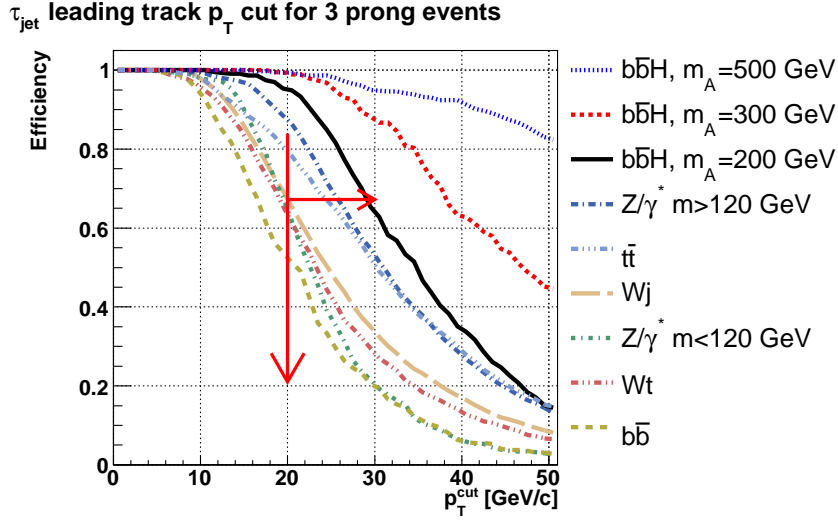


Figure C.4: The τ – jet leading track p_T integrated distribution. Only events with 3 tracks in the signal cone contribute to the histogram.

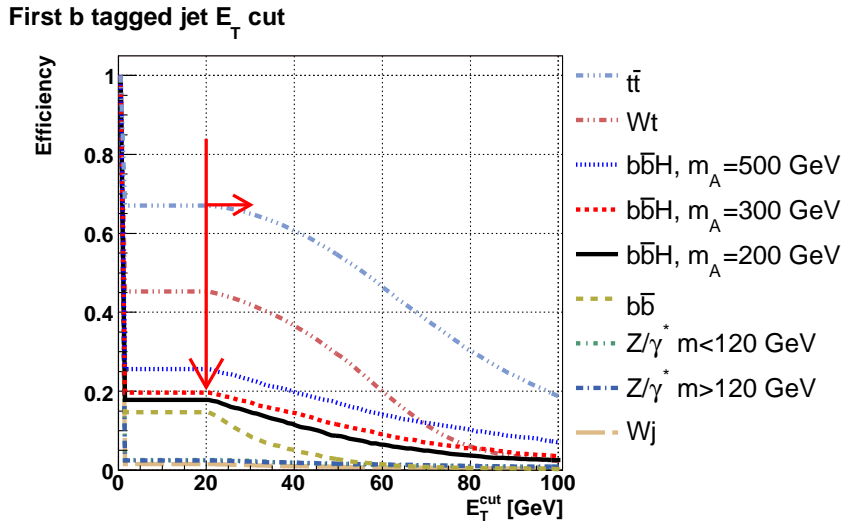


Figure C.5: First b tagged jet E_T integrated distribution. The jets are reconstructed above $E_T = 20 \text{ GeV}$. The value below 20 GeV shows the b tag efficiency for each sample.

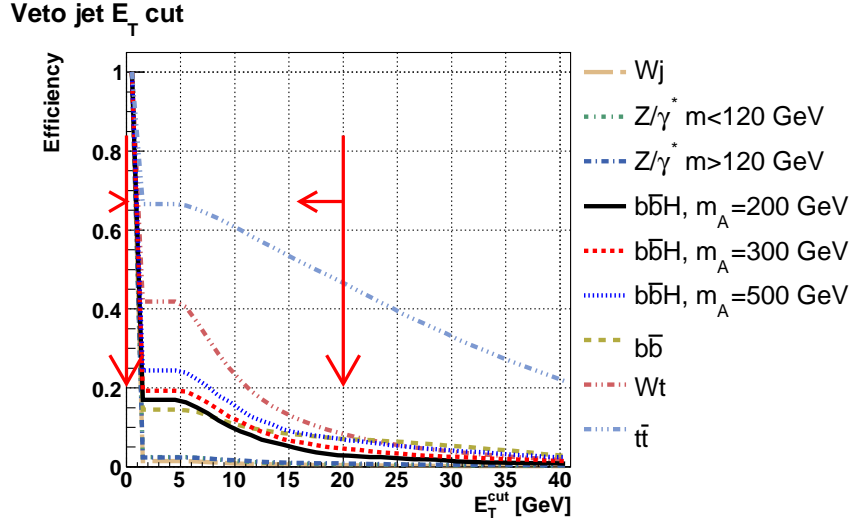


Figure C.6: Integrated distribution for E_T of central jet ($|\eta| < 2.4$) additional to τ jet and b tagged jet. The jets are reconstructed above $E_T = 10$ GeV. The value below 10 GeV shows fraction of additional central jets in each sample.

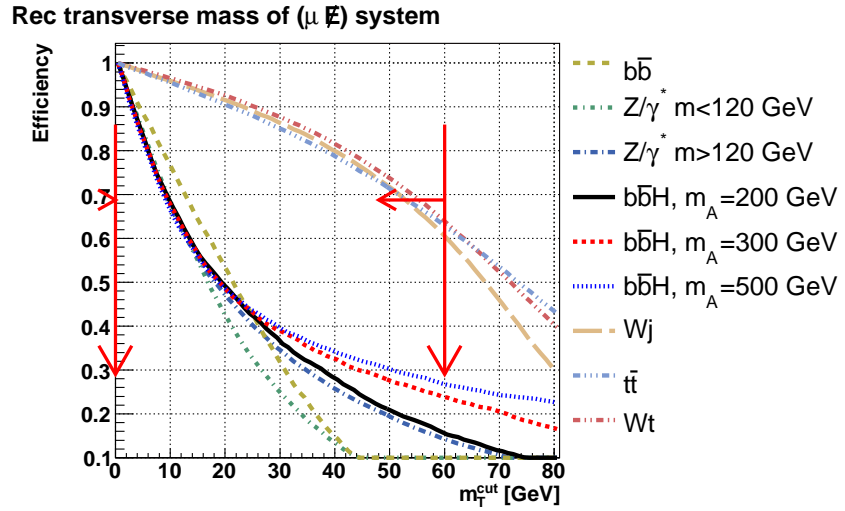


Figure C.7: Integrated distribution of transverse mass of the muon and the missing E_T .

Jet hadronic energy vs leading track momentum.

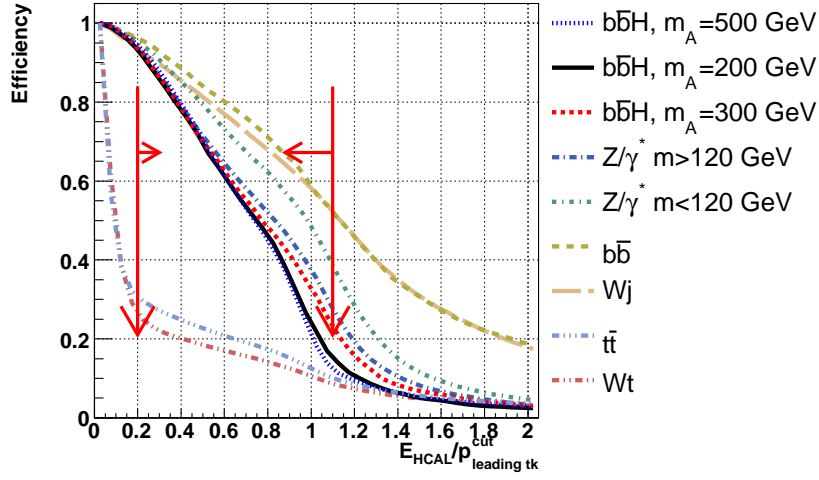


Figure C.8: Integrated distribution of the ratio of the τ – jet hadronic energy and the leading track momentum. Only single prong evens contribute to the histogram.

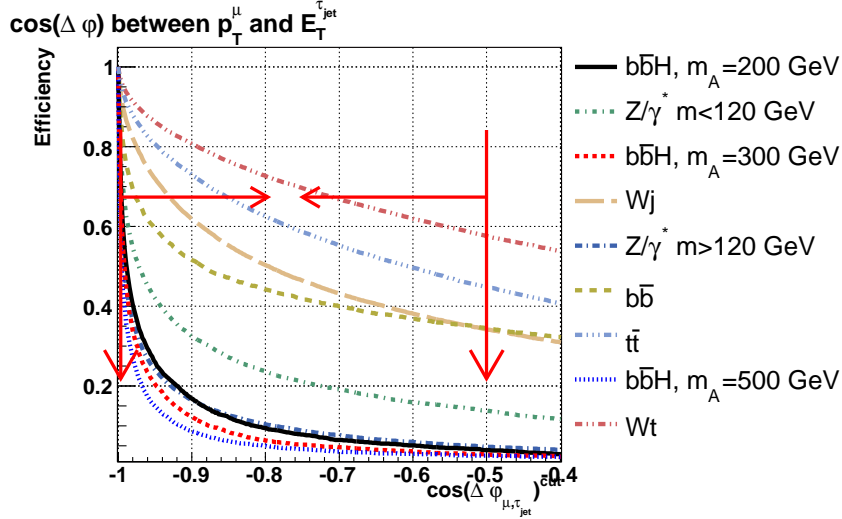


Figure C.9: Integrated distribution of the cosine of the azimuthal angle between the muon and the τ – jet directions.

Appendix D

Correlations between selection variables

The appendix collects integrated distributions of variables used in the reduction of background events. The distributions show the state after each one cut listed in the legend.

The legend entries are ordered by the selection efficiency in the acceptance region. The top entry refers to sample with the highest selection efficiency on the corresponding variable. The acceptance ranges are marked by arrows. The plots are presented for the $b\bar{b}H$ with $m_A = 200 \text{ GeV}/c^2$ and $t\bar{t}$ processes.

D.1 $b\bar{b}H$ with $m_A = 200 \text{ GeV}/c^2$

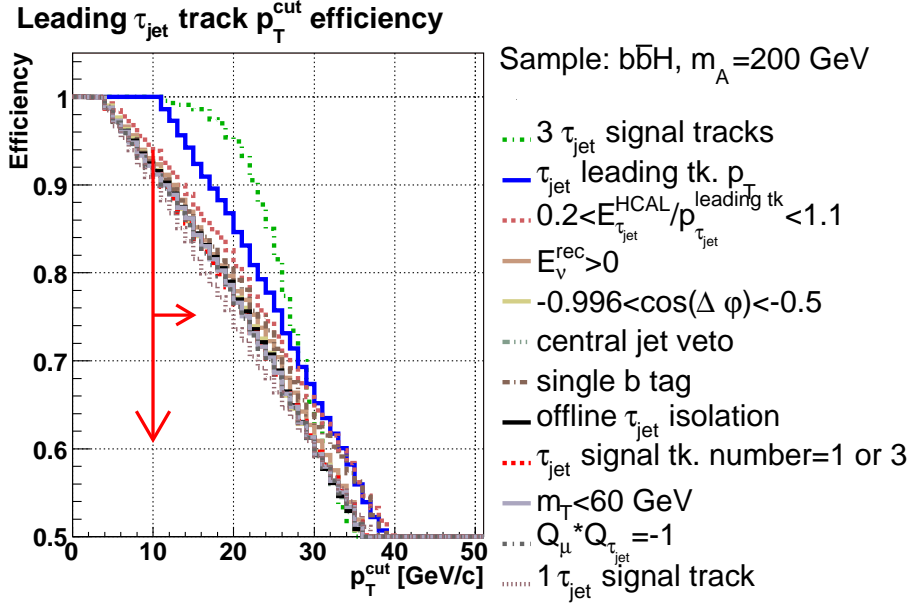


Figure D.1: Integrated distribution of the τ – jet leading track p_T .

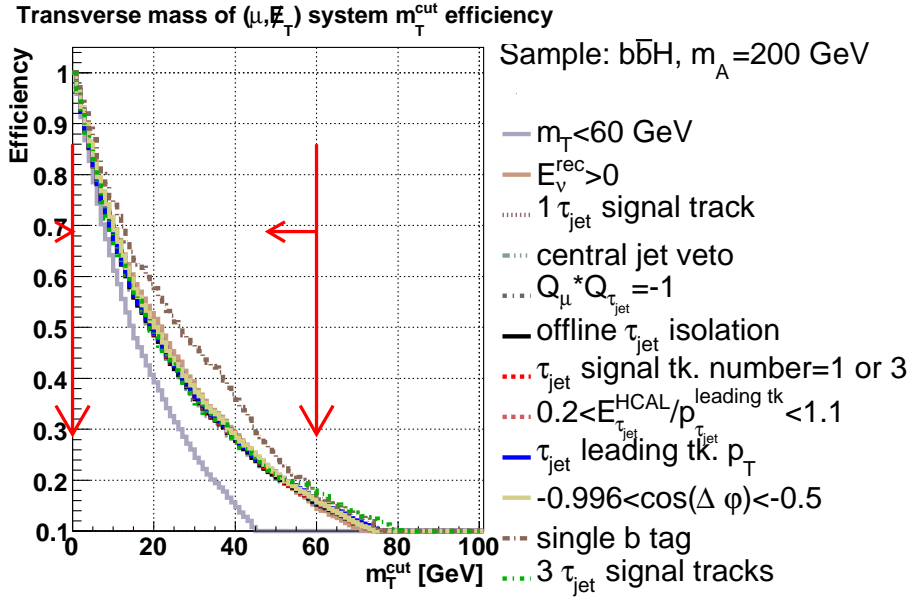


Figure D.2: Integrated distribution of the transverse mass of the muon and the missing E_T .

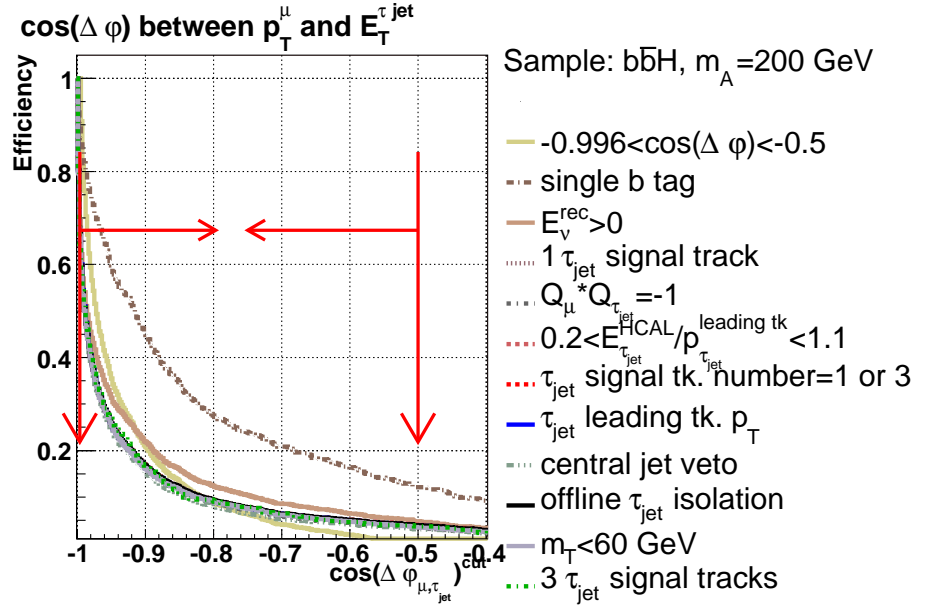


Figure D.3: Integrated distribution of the cosine of the azimuthal angle between the muon and the τ – jet directions.

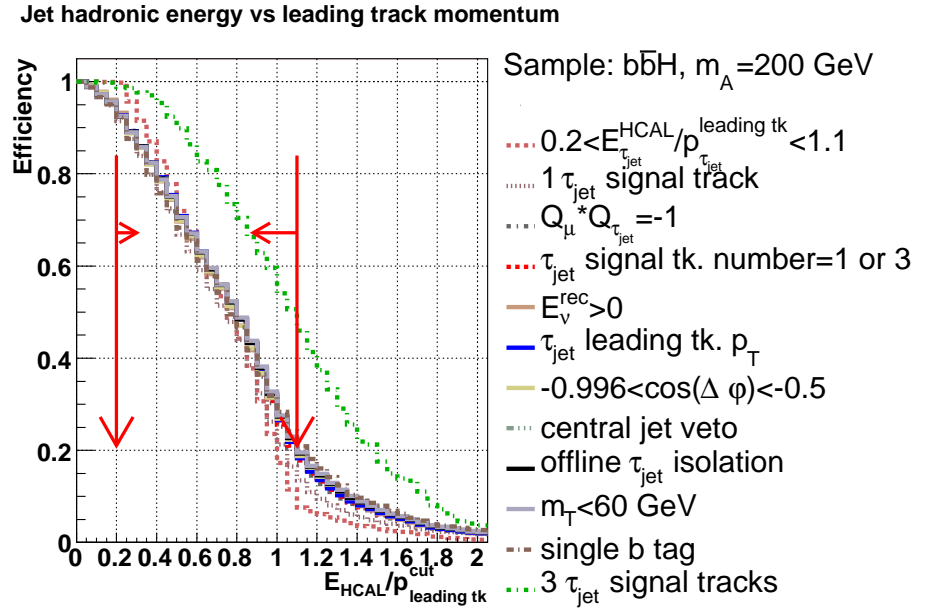


Figure D.4: Integrated distribution of the ratio of the τ – jet hadronic energy and the leading track momentum.

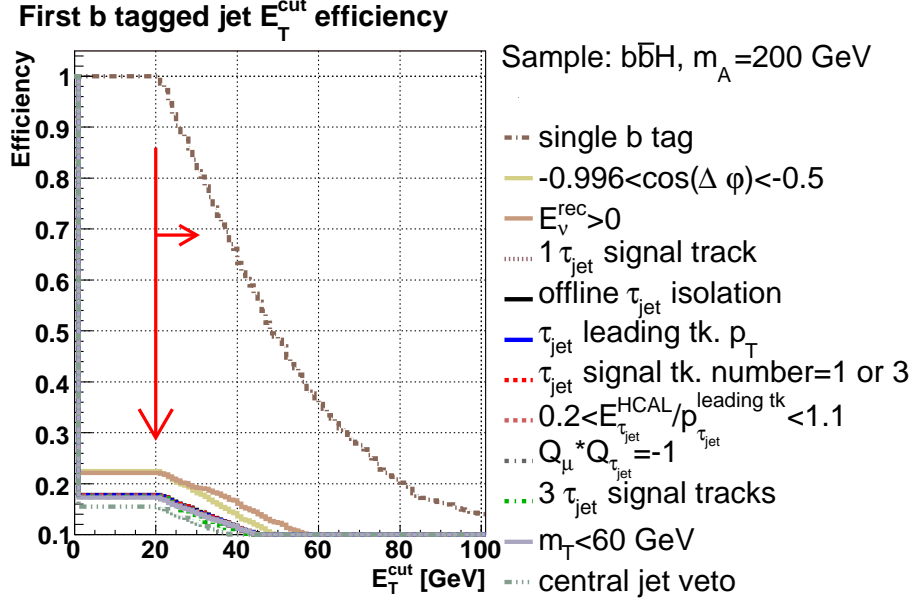


Figure D.5: Integrated distribution of the first b tagged jet E_T . The jets are reconstructed above $E_T = 20$ GeV. The value below 20 GeV shows the b tag efficiency after each selection.

D.2 $t\bar{t}$

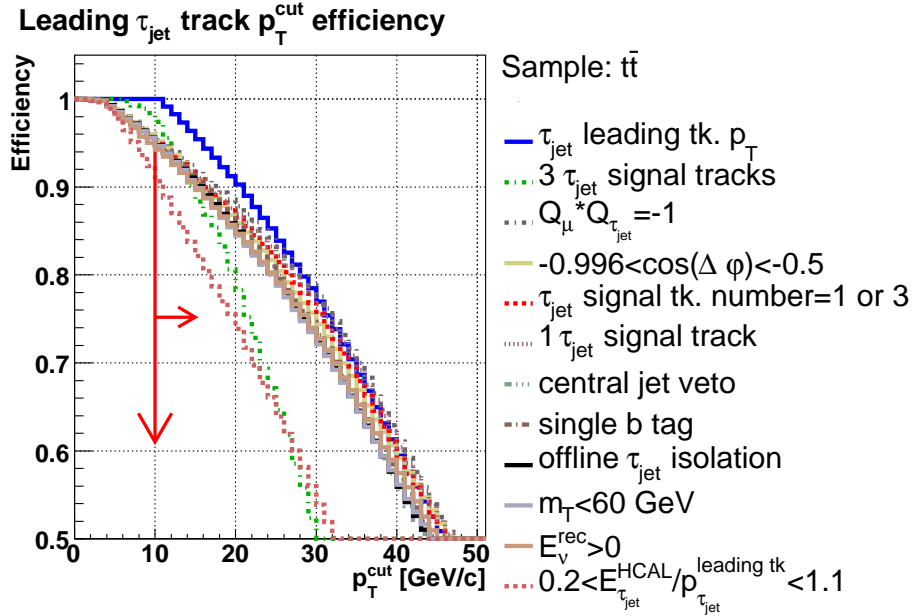


Figure D.6: Integrated distribution of the τ – jet leading track p_T .

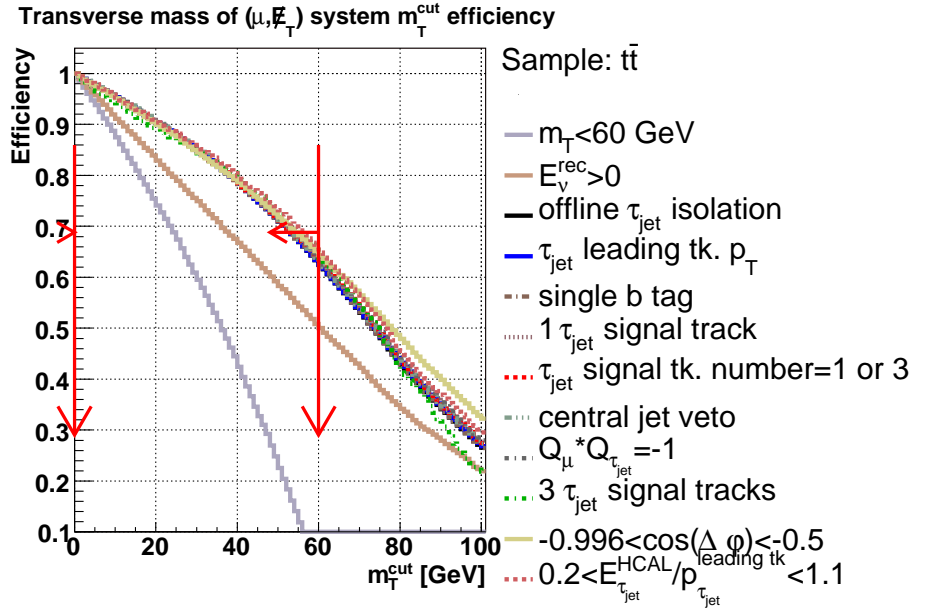


Figure D.7: Integrated distribution of the transverse mass of the muon and the missing E_T .

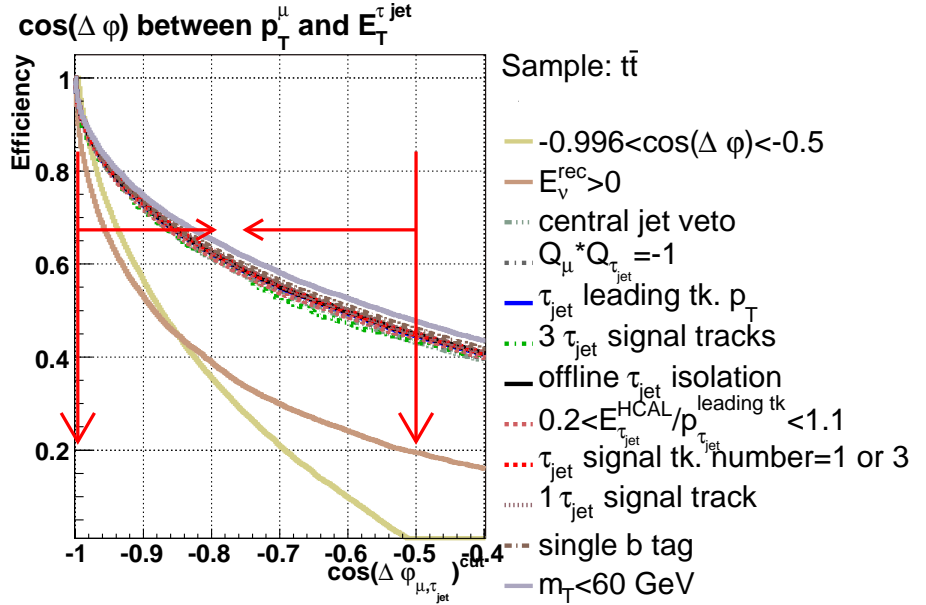


Figure D.8: Integrated distribution of the cosine of the azimuthal angle between the muon and the τ – jet directions.

Jet hadronic energy vs leading track momentum

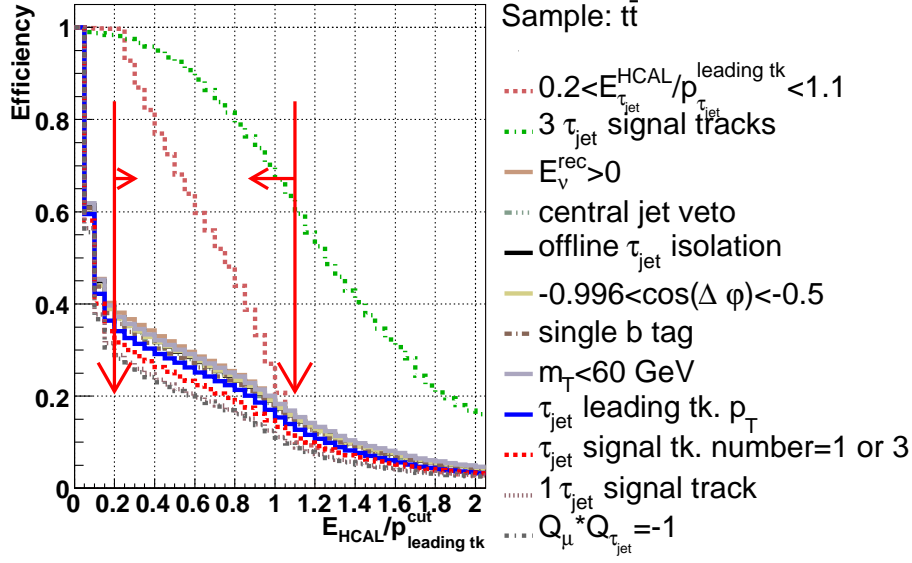


Figure D.9: Integrated distribution of the ratio of the τ – jet hadronic energy and the leading track momentum.

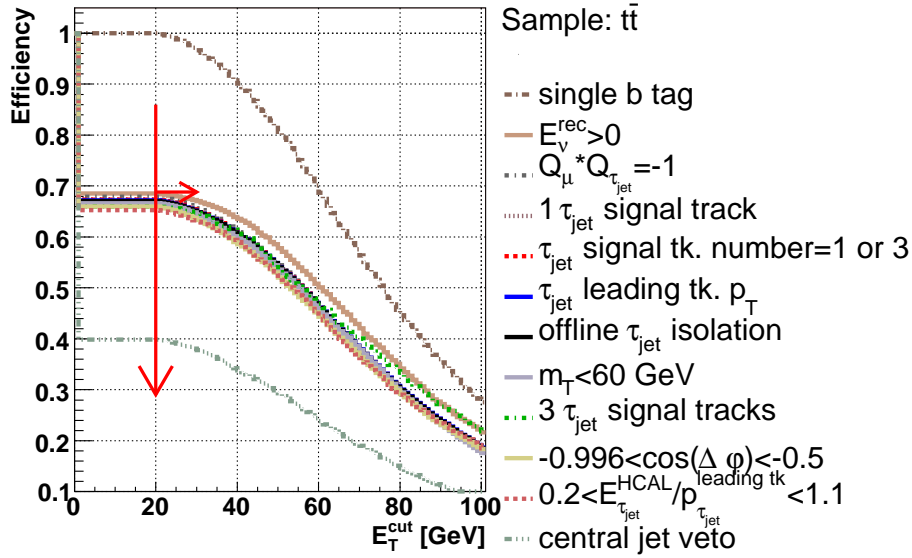
First b tagged jet E_T^{cut} efficiency

Figure D.10: Integrated distribution of the first b tagged jet E_T . The jets are reconstructed above $E_T = 20 \text{ GeV}$. The value below 20 GeV shows the b tag efficiency after each selection.

Appendix E

Plots used for the selections thresholds optimization

The appendix contains distributions used in the optimization of the thresholds values. The X axis on the plots show the threshold value, and Y axis shows the signal significance for given thresholds. For most of the plots the lower threshold is shown on the X axis, e.g. events with the variable value above the thresholds are accepted. In some cases the upper threshold is presented, e.g. events with the variable value below the threshold are accepted.

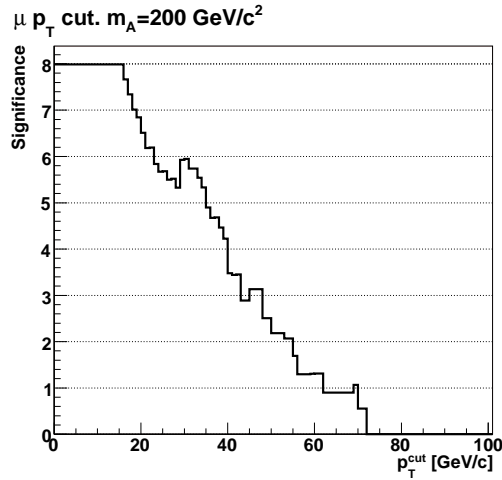


Figure E.1: The signal significance as the function of the offline muon transverse momentum cut.

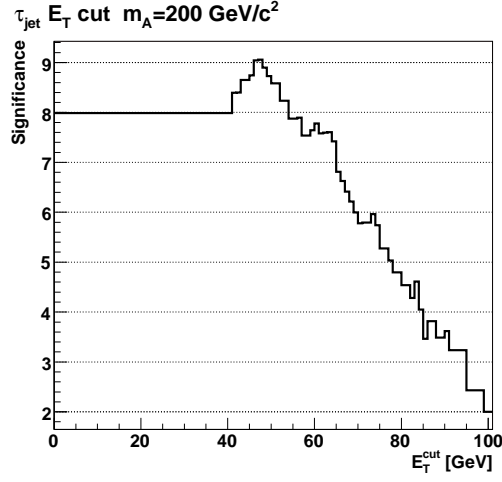


Figure E.2: The signal significance as the function of the offline τ – jet transverse energy cut. The maximum at ~ 45 GeV/c appears due to the limited Monte Carlo statistics.

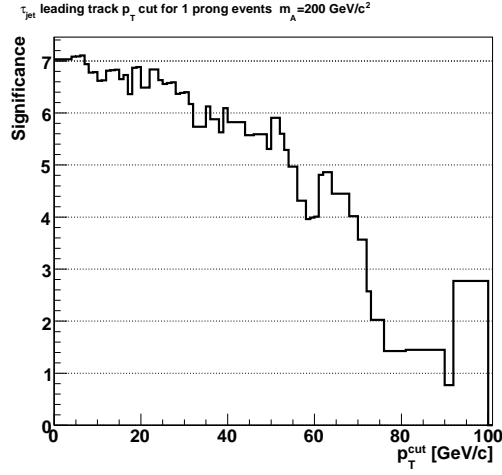


Figure E.3: The signal significance as the function of the offline threshold for the τ – jet leading track p_T thresholds for the 1 prong events.

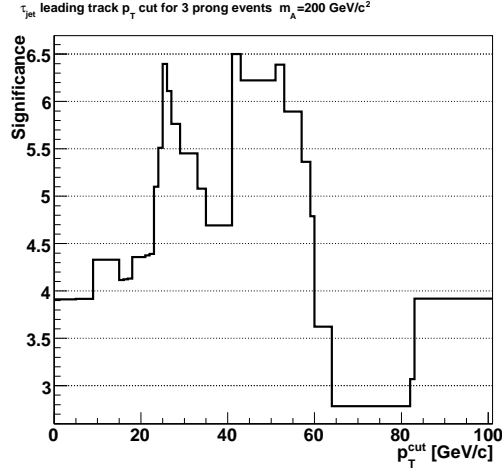


Figure E.4: The signal significance as the function of the offline threshold for the τ – jet leading track p_T thresholds for the 3 prong events. The Monte Carlo events statistics for the background is very limited for this selection, therefore no reasonable conclusion can be drawn here.

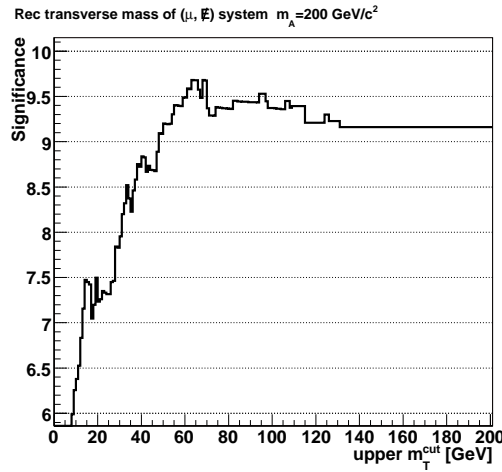


Figure E.5: The signal significance as the function of the upper offline thresholds for the transverse energy of the muon and the missing energy system.

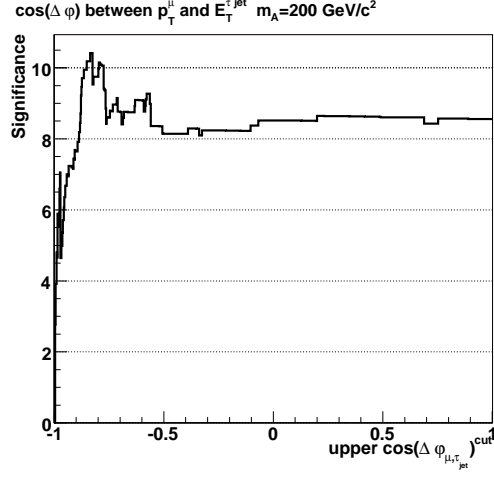


Figure E.6: The signal significance as the function of the upper offline threshold for the $\cos(\Delta\varphi_{\vec{p}_T, \vec{E}_T^{\text{jet}}})$. The maximum near $\cos(\Delta\varphi_{\vec{p}_T, \vec{E}_T^{\text{jet}}}) = -0.2$ appears due to the limited Monte Carlo statistics.

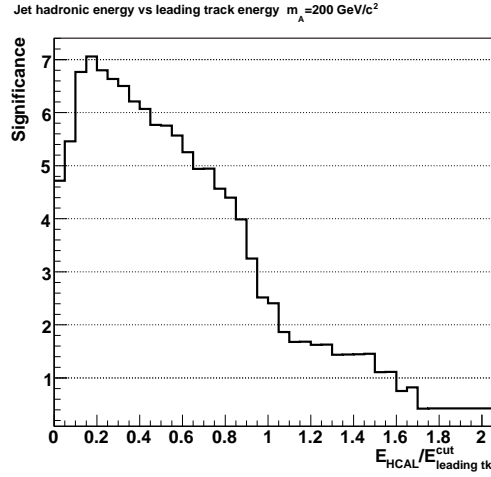


Figure E.7: The signal significance as the function of the lower offline threshold for the ratio of the τ -jet energy stored in the hadron calorimeter to the leading track energy.

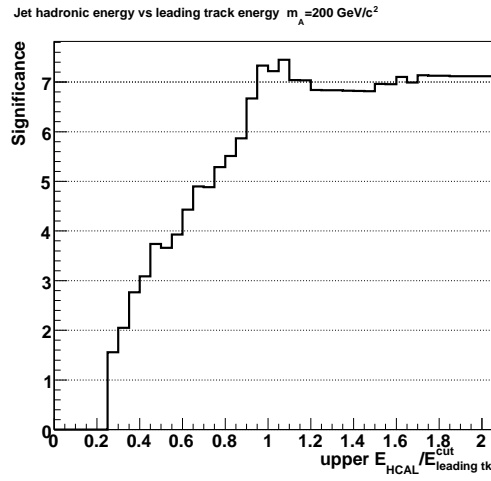


Figure E.8: The signal significance as the function of the upper offline threshold for the ratio of the τ – jet energy stored in the hadron calorimeter to the leading track energy.

Appendix F

Trigger and offline selection efficiencies

The Appendix presents the trigger and offline selection efficiencies after each selection step. The HLT selection was decomposed into the Level 2 (L2) and Level 3 (L3) kinematic and isolation selections. The trigger selections efficiencies are presented with the respect to the preselected events. The offline selections efficiencies are presented with the respect to the events passing the trigger selection.

F.1 Trigger selections

Table F.1: Trigger selection efficiency for signal processes. Lines in bold show the efficiency after L1, L2 kinematic, L2 kinematic with isolation and L3 selections. Numbers in parentheses in the selection name indicate the threshold values.

Cut	$bbH(200)$	$H(200)$	$bbH(300)$
single L1 Mu(14)	0.9	0.89	0.89
single L1 Tau(93)	0.034	0.072	0.27
L1Mu(14)	0.9	0.89	0.89
L1 mu AND single L2 Mu(15)	0.89	0.88	0.88
L1 mu AND single L2 Tau(40)	0.65	0.64	0.71
L1 mu AND L2Mu(15) AND L2Tau(40)	0.64	0.64	0.7
L1 mu AND L2MuPt(15) Isol(0.97) AND L2TauEt(40)	0.62	0.62	0.67
L1 mu AND L2MuPt(15) AND L2TauEt(40) Isol(5.6)	0.57	0.54	0.62
L1 mu AND L2Mu(15) AND L2Tau(40) both with isol	0.55	0.53	0.6
L1 mu AND L2 AND single L3 Mu(15)	0.55	0.52	0.59
L1 mu AND L2 AND single L3 Tau (L2 tau with px isol)	0.43	0.39	0.46
L1 mu AND L2 AND single L3 Mu (15) with isol(0.97)	0.54	0.51	0.55
L1 mu AND L2 AND L3Mu(15) AND L3Tau(40) with isol	0.42	0.38	0.43

F. TRIGGER AND OFFLINE SELECTION EFFICIENCIES

Table F.2: Trigger selection efficiency for signal processes. Lines in bold show the efficiency after L1, L2 kinematic, L2 kinematic with isolation and L3 selections. Numbers in parentheses in the selection name indicate the threshold values.

Cut	$bbH(500)$	$H(500)$
single L1 Mu(14)	0.91	0.9
single L1 Tau(93)	0.55	0.53
L1Mu(14)	0.91	0.9
L1 mu AND single L2 Mu(15)	0.9	0.89
L1 mu AND single L2 Tau(40)	0.76	0.75
L1 mu AND L2Mu(15) AND L2Tau(40)	0.75	0.74
L1 mu AND L2MuPt(15) Isol(0.97) AND L2TauEt(40)	0.72	0.71
L1 mu AND L2MuPt(15) AND L2TauEt(40) Isol(5.6)	0.68	0.63
L1 mu AND L2Mu(15) AND L2Tau(40) both with isol	0.65	0.61
L1 mu AND L2 AND single L3 Mu(15)	0.64	0.6
L1 mu AND L2 AND single L3 Tau (L2 tau with px isol)	0.51	0.46
L1 mu AND L2 AND single L3 Mu (15) with isol(0.97)	0.63	0.59
L1 mu AND L2 AND L3Mu(15) AND L3Tau(40) with isol	0.5	0.45

Table F.3: Trigger selection efficiency for background processes. Rows in bold show the efficiency after L1, L2 kinematic, L2 kinematic with isolation and L3 selections. Numbers in parentheses in the selection name indicate the threshold values. The values for $b\bar{b}$ include the event weight.

Cut	$t\bar{t}$	Wj	Wt	$b\bar{b}$
single L1 Mu(14)	0.91	0.84	0.89	0.023
single L1 Tau(93)	0.1	0.025	0.017	0.000024
L1Mu(14)	0.91	0.84	0.89	0.023
L1 mu AND single L2 Mu(15)	0.9	0.83	0.88	0.022
L1 mu AND single L2 Tau(40)	0.72	0.3	0.5	0.0028
L1 mu AND L2Mu(15) AND L2Tau(40)	0.71	0.3	0.5	0.0028
L1 mu AND L2MuPt(15) Isol(0.97) AND L2TauEt(40)	0.67	0.29	0.47	0.0017
L1 mu AND L2MuPt(15) AND L2TauEt(40) Isol(5.6)	0.31	0.17	0.27	0.0013
L1 mu AND L2Mu(15) AND L2Tau(40) both with isol	0.29	0.17	0.26	0.00083
L1 mu AND L2 AND single L3 Mu(15)	0.29	0.16	0.26	0.00081
L1 mu AND L2 AND single L3 Tau	0.1	0.043	0.11	0.00044
L1 mu AND L2 AND single L3 Mu (15) with isol(0.97)	0.28	0.16	0.25	0.00044
L1 mu AND L2 AND L3Mu(15) AND L3Tau(40)	0.096	0.042	0.11	0.00024

F.1 Trigger selections

Table F.4: Trigger selection efficiency for background processes. Rows in bold show the efficiency after L1, L2 kinematic, L2 kinematic with isolation and L3 selections. Numbers in parentheses in the selection name indicate the threshold values.

	$Z/\gamma^* \rightarrow \tau\tau \rightarrow \mu + \tau_{jet} + \nu$	
	$40 < m_{\tau\tau} < 120$	$m_{\tau\tau} > 120$
single L1 Mu(14)	0.8	0.83
single L1 Tau(93)	0.0085	0.057
L1Mu(14)	0.8	0.83
L1 mu AND single L2 Mu(15)	0.79	0.81
L1 mu AND single L2 Tau(40)	0.24	0.49
L1 mu AND L2Mu(15) AND L2Tau(40)	0.24	0.48
L1 mu AND L2MuPt(15) Isol(0.97) AND L2TauEt(40)	0.23	0.47
L1 mu AND L2MuPt(15) AND L2TauEt(40) Isol(5.6)	0.19	0.42
L1 mu AND L2Mu(15) AND L2Tau(40) both with isol	0.18	0.41
L1 mu AND L2 AND single L3 Mu(15)	0.18	0.4
L1 mu AND L2 AND single L3 Tau (L2 tau with px isol)	0.11	0.29
L1 mu AND L2 AND single L3 Mu (15) with isol(0.97)	0.17	0.38
L1 mu AND L2 AND L3Mu(15) AND L3Tau(40) with isol	0.1	0.28

Table F.5: Trigger selection efficiency for background processes. Rows in bold show the efficiency after L1, L2 kinematic, L2 kinematic with isolation and L3 selections. Numbers in parentheses in the selection name indicate the threshold values.

	$bb(Z \rightarrow \tau\tau)$	
	$60 < m_{\tau\tau} < 100$	$m_{\tau\tau} > 100$
single L1 Mu(14)	0.14	0.16
single L1 Tau(93)	0.0065	0.02
L1Mu(14)	0.14	0.16
L1 mu AND single L2 Mu(15)	0.12	0.14
L1 mu AND single L2 Tau(40)	0.031	0.053
L1 mu AND L2Mu(15) AND L2Tau(40)	0.026	0.046
L1 mu AND L2MuPt(15) Isol(0.97) AND L2TauEt(40)	0.021	0.039
L1 mu AND L2MuPt(15) AND L2TauEt(40) Isol(5.6)	0.016	0.032
L1 mu AND L2Mu(15) AND L2Tau(40) both with isol	0.012	0.027
L1 mu AND L2 AND single L3 Mu(15)	0.0098	0.023
L1 mu AND L2 AND single L3 Tau (L2 tau with px isol)	0.0062	0.016
L1 mu AND L2 AND single L3 Mu (15) with isol(0.97)	0.0089	0.021
L1 mu AND L2 AND L3Mu(15) AND L3Tau(40) with isol	0.0041	0.012

F.2 Offline selections

Table F.6: Offline selection efficiency for the signal events. In parentheses the efficiency relative to the previous cut is shown.

Sample:	$bbH(200)$	$H(200)$	$bbH(300)$
Offline τ_{jet} isolation	$9.54 \cdot 10^{-1}$ (1)	$9.45 \cdot 10^{-1}$ (1)	$9.58 \cdot 10^{-1}$ (1)
1 or 3 tk. in τ_{jet} signal cone	$8.70 \cdot 10^{-1}$ (0.912)	$8.54 \cdot 10^{-1}$ (0.904)	$8.57 \cdot 10^{-1}$ (0.895)
Leading track $p_T > 10 \text{ GeV}/c$	$7.87 \cdot 10^{-1}$ (0.905)	$7.74 \cdot 10^{-1}$ (0.907)	$7.99 \cdot 10^{-1}$ (0.932)
$Q_\mu \cdot Q_{jet} = -1$	$7.57 \cdot 10^{-1}$ (0.961)	$7.49 \cdot 10^{-1}$ (0.967)	$7.48 \cdot 10^{-1}$ (0.936)
Single b tag	$1.31 \cdot 10^{-1}$ (0.173)	$4.56 \cdot 10^{-2}$ (0.0609)	$1.44 \cdot 10^{-1}$ (0.193)
No jet with $E_T > 20$, $ \eta < 2.5$	$1.12 \cdot 10^{-1}$ (0.853)	$2.73 \cdot 10^{-2}$ (0.598)	$1.12 \cdot 10^{-1}$ (0.775)
$m_T(l, MET) < 60 \text{ GeV}$	$9.29 \cdot 10^{-2}$ (0.833)	$2.20 \cdot 10^{-2}$ (0.808)	$8.43 \cdot 10^{-2}$ (0.754)
$-0.9962 < \cos(\Delta\varphi) < -0.5$	$7.48 \cdot 10^{-2}$ (0.805)	$1.08 \cdot 10^{-2}$ (0.488)	$6.82 \cdot 10^{-2}$ (0.809)
$0.2 < \text{HCAL E/lead. tk. p} < 1.1$	$6.15 \cdot 10^{-2}$ (0.822)	$7.08 \cdot 10^{-3}$ (0.659)	$5.09 \cdot 10^{-2}$ (0.747)
$E_\nu^1 > 0, E_\nu^2 > 0$	$4.21 \cdot 10^{-2}$ (0.684)	$5.77 \cdot 10^{-3}$ (0.815)	$3.54 \cdot 10^{-2}$ (0.695)

Table F.7: Offline selection efficiency for signal events. In parentheses the efficiency relative to the previous cut is shown

Sample:	$bbH(500)$	$H(500)$
Offline τ_{jet} isolation	$9.60 \cdot 10^{-1}$ (1)	$9.56 \cdot 10^{-1}$ (1)
1 or 3 tk. in τ_{jet} signal cone	$8.82 \cdot 10^{-1}$ (0.919)	$8.77 \cdot 10^{-1}$ (0.917)
Leading track $p_T > 10 \text{ GeV}/c$	$8.42 \cdot 10^{-1}$ (0.955)	$8.37 \cdot 10^{-1}$ (0.954)
$Q_\mu \cdot Q_{jet} = -1$	$8.08 \cdot 10^{-1}$ (0.96)	$7.98 \cdot 10^{-1}$ (0.954)
Single b tag	$2.07 \cdot 10^{-1}$ (0.256)	$7.87 \cdot 10^{-2}$ (0.0986)
No jet with $E_T^{calib} > 20$, $ \eta < 2.5$	$1.60 \cdot 10^{-1}$ (0.772)	$3.57 \cdot 10^{-2}$ (0.454)
$m_T(l, MET) < 60 \text{ GeV}$	$1.12 \cdot 10^{-1}$ (0.701)	$2.31 \cdot 10^{-2}$ (0.646)
$-0.9962 < \cos(\Delta\varphi) < -0.5$	$8.42 \cdot 10^{-2}$ (0.751)	$1.66 \cdot 10^{-2}$ (0.721)
HCAL E/leading tk. p: $0.2 < f < 1.1$	$7.20 \cdot 10^{-2}$ (0.854)	$1.29 \cdot 10^{-2}$ (0.773)
$E_\nu^1 > 0, E_\nu^2 > 0$	$5.52 \cdot 10^{-2}$ (0.768)	$1.11 \cdot 10^{-2}$ (0.862)

Table F.8: Offline selection efficiency for background events. In parentheses the efficiency relative to the previous cut is shown.

Sample:	$t\bar{t}$	Wj
Offline τ_{jet} isolation	$8.51 \cdot 10^{-1}$ (1)	$6.70 \cdot 10^{-1}$ (1)
1 or 3 tk. in τ_{jet} signal cone	$7.59 \cdot 10^{-1}$ (0.892)	$4.22 \cdot 10^{-1}$ (0.63)
Leading track $p_T > 10 \text{ GeV}/c$	$7.14 \cdot 10^{-1}$ (0.942)	$3.62 \cdot 10^{-1}$ (0.858)
$Q_\mu \cdot Q_{jet} = -1$	$6.56 \cdot 10^{-1}$ (0.918)	$2.65 \cdot 10^{-1}$ (0.731)
Single b tag	$4.42 \cdot 10^{-1}$ (0.673)	$2.88 \cdot 10^{-3}$ (0.0109)
No jet with $E_T^{calib} > 20$, $ \eta < 2.5$	$1.51 \cdot 10^{-1}$ (0.343)	$2.35 \cdot 10^{-3}$ (0.817)
$m_T(l, MET) < 60 \text{ GeV}$	$5.35 \cdot 10^{-2}$ (0.353)	$8.85 \cdot 10^{-4}$ (0.376)
$-0.9962 < \cos(\Delta\varphi) < -0.5$	$2.65 \cdot 10^{-2}$ (0.495)	$5.81 \cdot 10^{-4}$ (0.656)
HCAL E/leading tk. p: $0.2 < f < 1.1$	$4.37 \cdot 10^{-3}$ (0.165)	$2.76 \cdot 10^{-4}$ (0.476)
$E_\nu^1 > 0, E_\nu^2 > 0$	$1.78 \cdot 10^{-3}$ (0.408)	$5.53 \cdot 10^{-5}$ (0.2)

Table F.9: Offline selection efficiency for the background events, continuation. In parentheses the efficiency relative to the previous cut is shown.

Sample:	Wt	$b\bar{b}$
Offline τ_{jet} isolation	$8.79 \cdot 10^{-1}$ (1)	$8.69 \cdot 10^{-1}$ (1)
1 or 3 tk. in τ_{jet} signal cone	$7.97 \cdot 10^{-1}$ (0.907)	$6.25 \cdot 10^{-1}$ (0.719)
Leading track $p_T > 10 \text{ GeV}/c$	$7.47 \cdot 10^{-1}$ (0.937)	$4.48 \cdot 10^{-1}$ (0.717)
$Q_\mu \cdot Q_{jet} = -1$	$7.11 \cdot 10^{-1}$ (0.952)	$2.44 \cdot 10^{-1}$ (0.545)
Single b tag	$3.24 \cdot 10^{-1}$ (0.456)	$2.30 \cdot 10^{-2}$ (0.0942)
No jet with $E_T^{calib} > 20$, $ \eta < 2.5$	$2.79 \cdot 10^{-1}$ (0.86)	$0.99 \cdot 10^{-2}$ (0.43)
$m_T(l, MET) < 60 \text{ GeV}$	$1.01 \cdot 10^{-1}$ (0.362)	$0.99 \cdot 10^{-2}$ (1)
$-0.9962 < \cos(\Delta\varphi) < -0.5$	$4.55 \cdot 10^{-2}$ (0.451)	$4.11 \cdot 10^{-3}$ (0.416)
HCAL E/leading tk. p: $0.2 < f < 1.1$	$5.79 \cdot 10^{-3}$ (0.127)	$1.22 \cdot 10^{-3}$ (0.298)
$E_\nu^1 > 0, E_\nu^2 > 0$	$2.41 \cdot 10^{-3}$ (0.415)	$4.41 \cdot 10^{-4}$ (0.36)

F. TRIGGER AND OFFLINE SELECTION EFFICIENCIES

Table F.10: Offline selection efficiency for the background events, continuation.
In parentheses the efficiency relative to the previous cut is shown.

	$Z/\gamma^* \rightarrow \tau\tau \rightarrow \mu + \tau_{jet} + \nu$	
	$40 < m_{\tau\tau} < 120 \text{ GeV}/c^2$	$m_{\tau\tau} > 120 \text{ GeV}/c^2$
Offline τ_{jet} isolation	$9.12 \cdot 10^{-1}$ (1)	$9.40 \cdot 10^{-1}$ (1)
1 or 3 tk. in τ_{jet} signal cone	$8.23 \cdot 10^{-1}$ (0.903)	$8.39 \cdot 10^{-1}$ (0.893)
Leading track $p_T > 10 \text{ GeV}/c$	$6.69 \cdot 10^{-1}$ (0.812)	$7.55 \cdot 10^{-1}$ (0.9)
$Q_\mu \cdot Q_{jet} = -1$	$6.34 \cdot 10^{-1}$ (0.947)	$7.04 \cdot 10^{-1}$ (0.933)
Single b tag	$1.70 \cdot 10^{-2}$ (0.0268)	$1.77 \cdot 10^{-2}$ (0.0251)
No jet with $E_T^{calib} > 20$, $ \eta < 2.5$	$1.32 \cdot 10^{-2}$ (0.777)	$1.23 \cdot 10^{-2}$ (0.698)
$m_T(l, MET) < 60 \text{ GeV}$	$1.24 \cdot 10^{-2}$ (0.941)	$9.53 \cdot 10^{-3}$ (0.774)
$-0.9962 < \cos(\Delta\varphi) < -0.5$	$4.65 \cdot 10^{-3}$ (0.375)	$6.26 \cdot 10^{-3}$ (0.657)
HCAL E/leading tk. p: $0.3 < f < 1.1$	$3.01 \cdot 10^{-3}$ (0.646)	$4.57 \cdot 10^{-3}$ (0.729)
$E_\nu^1 > 0, E_\nu^2 > 0$	$1.94 \cdot 10^{-3}$ (0.645)	$2.95 \cdot 10^{-3}$ (0.646)

Table F.11: Offline selection efficiency for the background events, continuation.
In parentheses the efficiency relative to the previous cut is shown.

	$bb(Z \rightarrow \tau\tau)$	
	$60 < m_{\tau\tau} < 100 \text{ GeV}/c^2$	$m_{\tau\tau} > 100 \text{ GeV}/c^2$
Offline τ_{jet} isolation	$9.05 \cdot 10^{-1}$ (1)	$9.34 \cdot 10^{-1}$ (1)
1 or 3 tk. in τ_{jet} signal cone	$8.25 \cdot 10^{-1}$ (0.912)	$8.56 \cdot 10^{-1}$ (0.917)
Leading track $p_T > 10 \text{ GeV}/c$	$7.10 \cdot 10^{-1}$ (0.86)	$7.69 \cdot 10^{-1}$ (0.898)
$Q_\mu \cdot Q_{jet} = -1$	$6.68 \cdot 10^{-1}$ (0.941)	$7.30 \cdot 10^{-1}$ (0.948)
Single b tag	$1.82 \cdot 10^{-1}$ (0.273)	$2.00 \cdot 10^{-1}$ (0.275)
No jet with $E_T^{calib} > 20$, $ \eta < 2.5$	$1.31 \cdot 10^{-1}$ (0.72)	$1.55 \cdot 10^{-1}$ (0.772)
$m_T(l, MET) < 60 \text{ GeV}$	$1.27 \cdot 10^{-1}$ (0.968)	$1.36 \cdot 10^{-1}$ (0.88)
$-0.9962 < \cos(\Delta\varphi) < -0.5$	$5.37 \cdot 10^{-2}$ (0.423)	$7.95 \cdot 10^{-2}$ (0.584)
HCAL E/leading tk. p: $0.2 < f < 1.1$	$3.75 \cdot 10^{-2}$ (0.698)	$4.06 \cdot 10^{-2}$ (0.511)
$E_\nu^1 > 0, E_\nu^2 > 0$	$1.62 \cdot 10^{-2}$ (0.432)	$2.28 \cdot 10^{-2}$ (0.562)

Appendix G

Measurement of the τ tag efficiency using the $Z \rightarrow \tau\tau \rightarrow \mu + \text{hadrons} + X$ events

G.1 Introduction

Tau lepton identification is an important part of many analyses on the the Higgs boson search and the Supersymmetry search. A precise knowledge of the τ identification efficiency and its uncertainty is particularly important for analyses based on the event counting. In this Appendix a method to measure the τ tagging efficiency using the τ leptons coming from the Z boson decays is described. The τ identification involves an isolation of the collimated jet (τ jet) of particles coming from the hadronic τ decays [67]. The calorimetry scale uncertainty appears as the main source of the systematic uncertainty of the signal selection and the background rejection efficiencies.

The final state considered in this analysis is $Z \rightarrow \tau\tau \rightarrow \mu + \tau \text{ jet} + \nu$, which is the same as the final state used in some analyses searching for the heavy, supersymmetric Higgs boson decaying into two τ leptons. The τ – jet isolation parameters, and offline selection cuts were chosen similar to the selections used in the analysis on the estimation of the MSSM parameter $\tan(\beta)$ [79; 82], which is an example of the analysis where a precise knowledge of the selection efficiencies, including the τ – jet tagging efficiency is needed.

The primary goal of this Appendix is to show that the $Z \rightarrow \tau\tau \rightarrow \mu + \tau \text{ jet} + \nu$ events can be selected in CMS and the τ -identification efficiency for this process can be measured from the data. It allows comparison with τ identification from the Monte Carlo (MC) for the same process, and thus make the MC predictions of τ identification for other processes like $b\bar{b}A \rightarrow \tau\tau$ more reliable.

G.2 The method

The τ -tagging efficiency can be estimated from the ratio of numbers of the Z events in two decay channels: $Z \rightarrow \mu\mu$, where no τ tagging is performed and $Z \rightarrow \tau\tau \rightarrow \mu + \tau \text{ jet} + X$, where a single τ tag is required. The measured number of $Z \rightarrow \mu\mu$ events is equal to the number of events measured in the $\mu\mu$ channel ($N_{\mu+\mu}^{\text{meas}}$) minus the number of expected number of background events ($N_{\mu+\mu}^{\text{bkg.}}$). Using the Z^0 cross section (σ_{Z^0}), integrated luminosity (L), branching ratio ($\text{BR}(Z \rightarrow \mu\mu)$), selection efficiencies for the trigger ($\epsilon_{\text{HLT}_{1\mu}}$) and the offline selections ($\epsilon_{\text{mass reco}}$), the expected number of events is:

$$N_{Z \rightarrow \mu\mu} = \sigma_{Z^0} \times L \times \text{BR}(Z \rightarrow \mu\mu) \times \epsilon_{\text{HLT}_{1\mu}}^{\mu\mu} \times \epsilon_{\text{mass reco}} = N_{\mu+\mu}^{\text{meas}} - N_{\mu+\mu}^{\text{bkg.}} \quad (\text{G.1})$$

and in the similar way for the number of events with the $\mu + \tau \text{ jet} + X$ final state:

$$N_{Z \rightarrow \tau\tau \rightarrow \mu+\tau \text{ jet}} = \sigma_{Z^0} \times L \times \text{BR}(Z \rightarrow \tau\tau \rightarrow \mu + \tau \text{ jet}) \times \epsilon_{\text{HLT}_{1\mu}}^{\mu\tau \text{ jet}} \times \epsilon_{\tau \text{ tag}} \times \epsilon_{\text{other}} = N_{\mu+\tau \text{ jet}}^{\text{meas}} - N_{\mu+\tau \text{ jet}}^{\text{bkg.}} \quad (\text{G.2})$$

where $\epsilon_{\tau \text{ tag}}$ is defined as the efficiency of the τ isolation in the isolation cone and the efficiency of finding one or three tracks in the signal cone, and ϵ_{other} is defined as the efficiency of selections rejecting background to the $Z \rightarrow \tau\tau \rightarrow \mu + \tau \text{ jet}$ and mass window selection.

The $\epsilon_{\text{mass reco}}$ for the $\mu\mu$ channel is the efficiency to find the second muon and mass window selection efficiency. Using these formulas one can obtain the expression for the $\epsilon_{\tau \text{ tag}}$:

$$\epsilon_{\tau \text{ tag}} = \frac{N_{\mu+\tau \text{ jet}}^{\text{meas}} - N_{\mu+\tau \text{ jet}}^{\text{bkg.}}}{N_{\mu+\mu}^{\text{meas}} - N_{\mu+\mu}^{\text{bkg.}}} \times \frac{\text{BR}(Z \rightarrow \mu\mu)}{\text{BR}(Z \rightarrow \tau\tau \rightarrow \mu + \tau \text{ jet})} \times \frac{\epsilon_{\text{HLT}_{1\mu}}^{\mu\mu}}{\epsilon_{\text{HLT}_{1\mu}}^{\mu\tau \text{ jet}}} \times \frac{\epsilon_{\text{mass reco}}^{\mu\mu}}{\epsilon_{\text{other}}^{\mu\tau \text{ jet}}} \quad (\text{G.3})$$

This expression contains terms which can be measured directly from the data, like branching ratios and the event numbers, but also terms that require additional information from the Monte-Carlo simulations. The uncertainties on the branching ratios are small: $\Delta\text{BR}/\text{BR} \simeq 10^{-3}$ [43] and are neglected in the formula below.

The uncertainty on measured $\epsilon_{\tau \text{ tag}}$ can be expressed in terms of the number of measured events in both channels ($N_{\mu+\mu}^{\text{meas}}$, $N_{\mu+\tau \text{ jet}}^{\text{meas}}$), uncertainty on the background evaluation ($\Delta N_{\mu+\tau \text{ jet}}^{\text{bkg.}}$, $\Delta N_{\mu+\mu}^{\text{bkg.}}$), and uncertainty of experimental selections ($\Delta\epsilon_{\text{HLT}}^{\mu\mu}$, $\Delta\epsilon_{\text{HLT}}^{\mu\tau \text{ jet}}$, $\Delta\epsilon_{\text{mass reco}}^{\mu\mu}$, $\Delta\epsilon_{\text{other}}^{\mu+\tau \text{ jet}}$) in the following way:

$$\begin{aligned}
 \frac{\Delta \epsilon_{\tau \text{ tag}}}{\epsilon_{\tau \text{ tag}}} = & \\
 & \begin{aligned}
 & \mu\mu \text{ stat.} & \mu + \tau \text{ jet stat.} & \text{bkg. to } \mu\mu \text{ eval.} & \text{bkg. to } \mu + \tau \text{ jet eval.} \\
 & \frac{\sqrt{N_{\mu+\mu}^{\text{meas}}}}{N_{\mu+\mu}^{\text{meas}} - N_{\mu+\mu}^{\text{bkg.}}} \oplus & \frac{\sqrt{N_{\mu+\tau \text{ jet}}^{\text{meas}}}}{N_{\mu+\tau \text{ jet}}^{\text{meas}} - N_{\mu+\tau \text{ jet}}^{\text{bkg.}}} \oplus & \frac{\Delta N_{\mu+\mu}^{\text{bkg.}}}{N_{\mu+\mu}^{\text{meas}} - N_{\mu+\mu}^{\text{bkg.}}} \oplus & \frac{\Delta N_{\mu+\tau \text{ jet}}^{\text{bkg.}}}{N_{\mu+\tau \text{ jet}}^{\text{meas}} - N_{\mu+\tau \text{ jet}}^{\text{bkg.}}} \oplus \\
 & \epsilon_{\text{HLT}}^{\mu\mu} \text{ sys} & \epsilon_{\text{HLT}}^{\mu\tau \text{ jet}} \text{ sys} & \epsilon_{\text{mass reco}}^{\mu\mu} \text{ sys} & \epsilon_{\text{other}}^{\mu+\tau \text{ jet}} \text{ calo sys} \\
 & \frac{\Delta \epsilon_{\text{HLT}}^{\mu\mu}}{\epsilon_{\text{HLT}}^{\mu\mu}} \oplus & \frac{\Delta \epsilon_{\text{HLT}}^{\mu\tau \text{ jet}}}{\epsilon_{\text{HLT}}^{\mu\tau \text{ jet}}} \oplus & \frac{\Delta \epsilon_{\text{mass reco}}^{\mu\mu}}{\epsilon_{\text{mass reco}}^{\mu\mu}} \oplus & \frac{\Delta \epsilon_{\text{other}}^{\mu+\tau \text{ jet}}}{\epsilon_{\text{other}}^{\mu+\tau \text{ jet}}}
 \end{aligned}
 \end{aligned}
 \tag{G.4}$$

Where the uncertainty on the number of background events is expressed as a function of Monte Carlo events used for the background estimation (N^{MC}), systematic uncertainty on the background selection efficiency ($\Delta^{\text{sys}}\epsilon$) and uncertainty on the background cross section ($\Delta\sigma$): $\Delta N_{\mu+\tau \text{ jet}}^{\text{bkg.}} = \left(\frac{1}{\sqrt{N^{\text{MC}}}} \oplus \frac{\Delta^{\text{sys}}\epsilon}{\epsilon} \oplus \frac{\Delta\sigma}{\sigma} \right) \cdot N_{\mu+\tau \text{ jet}}^{\text{bkg.}}$

Due to the large expected number of signal events in the $\mu\mu$ channel (Table G.2), uncertainties arising from this channel both statistical and from the background estimation are expected to be less than 1% and are small compared to other terms and can be neglected. Also uncertainties on the trigger selection for both channels are expected to be less than 1%, since the single muon trigger is not sensitive to the misalignment [52]. No additional contributions from the Z boson p_T spectrum uncertainty were considered, since it will be measured with high precision using the $Z \rightarrow \mu\mu$ events. The measured spectrum can be used to reweight the spectrum used in the Monte Carlo simulations.

In this Appendix only the statistical and the systematical uncertainties on the offline selection in the $\mu + \tau$ jet channel are considered. The p_T spectra for considered processes are assumed to be measured. The detector is assumed to be aligned, and the remaining misalignment is expected to introduce much smaller uncertainty than the calorimetry scale.

G.3 Background

Processes leading to a hard isolated muon and hard jet have been selected as possible backgrounds. The list of analyzed backgrounds includes QCD jets, top pair production, and W boson accompanied by a jet. The cross sections used are listed in Table G.1. For all processes except the W+jet one the Next to Leading Order (NLO) cross section was used.

Table G.1: Cross section of all the considered processes. The calculation order and the generator level preselection efficiency are shown.

Events sample	Cross section [pb]	Calculation order	Preselection efficiency
$Z \rightarrow \mu\mu$	2127	NLO [49]	0.21
$Z \rightarrow \tau\tau \rightarrow \mu + \tau \text{ jet} + X$	468	NLO [49]	0.068
$t\bar{t}$	830	NLO [83]	0.09
$W + \text{jet}$	41457	LO (Pythia)	0.014
QCD($b\bar{b}$)	$2.29 \cdot 10^7$	normalisation described in App. B	$7.6 \cdot 10^{-4}$

G.4 Experimental selections

G.4.1 Trigger selection

The events are selected with the single muon trigger. The L1 p_T threshold is set to 14 GeV/c. The L2 single muon trigger includes the calorimetric isolation and $p_T > 19$ GeV/c cut, the L3 trigger requires the tracker isolation and $p_T > 19$ GeV/c cut. The muon isolation algorithms are described in the details in 6 and [65].

G.4.2 Offline selection

The offline selections follow the MSSM Higgs analyses [79]. Offline selection cuts can be divided into three groups: offline τ identification, cuts providing efficient background reduction and cuts necessary for a good Higgs boson mass reconstruction:

- Offline τ identification:
 - full tracker τ isolation;
 - 1 or 3 tracks in the τ signal cone.
- Background reductions:
 - muon $p_T > 20$ GeV/c;
 - leading τ – jet $E_T > 45$ GeV/c;
 - p_T of the leading track in the τ jet > 40 GeV/c;

- jet veto: exactly one jet with $E_T \geq 25$ GeV and $|\eta| \leq 2.4$ additional to the τ jet;
 - transverse mass of the muon and the missing E_T system
 $m_T(\mu, \cancel{E}_T) \leq 30$ GeV;
 - electron veto: ratio of jet energy stored in the HCAL to the leading track momentum: $0.3 < f$.
- Mass reconstruction specific selections:
 - $\cos(\Delta\varphi_{\mu, \tau \text{ jet}}) \geq -0.9962$;
 - positive reconstructed energy of the neutrinos: $E_{\nu 1} > 0, E_{\nu 2} > 0$;
 - mass window $70 < m_{\tau\tau} < 130$ GeV/ c^2 .

The mass of the Z boson was reconstructed using the collinear assumption for the decay products of the τ leptons, described in details in Chapter 6. The method requires the muon and τ jet transverse momenta are not back-to-back. Therefore $\cos(\Delta\varphi_{\mu, \tau \text{ jet}}) \geq -0.9962$ is required. The requirement for exactly one additional central jet also improves the mass reconstruction efficiency, since it selects events with larger Z boson p_T , which results in less back-to-back configuration of the muon and the τ jet. Since the jet veto reduces significantly the W+jet background this requirement improves the signal over background ratio.

The events are counted in the window in the $\tau\tau$ mass between 70 and 100 GeV/ c^2 . The number of events after each selection step is reported in Table G.2. At the end there are $7.2 \cdot 10^6$ $Z \rightarrow \mu\mu$ events, but only ~ 1000 $Z \rightarrow \tau\tau \rightarrow \mu + \tau \text{ jet} + X$ signal events. The total number of background events is 166 with the main contribution from the $t\bar{t}$ and $b\bar{b}$ events.

G.5 Selection uncertainty due to the calorimeter scale

The main source of the systematic selection uncertainty is the uncertainty on the global calorimetry scale. For the integrated luminosity of 30 fb^{-1} , the measured jet scale uncertainty is expected to be of order of 3%, with the use of the W mass constraint [52]. The uncertainty of the missing transverse energy scale was assumed to be 5%. The energy scale uncertainty for the τ jets was assumed to be the same as for the QCD jets. There are no detailed studies on the estimation of the τ jet energy calibration. Preliminary studies show that it might be possible

G. MEASUREMENT OF THE τ TAG EFFICIENCY USING THE $Z \rightarrow \tau\tau \rightarrow \mu + \text{HADRONS} + X$ EVENTS

Table G.2: Number of events for 30 fb^{-1} , with low luminosity, passing each selection step. The number of events after the τ tagging is marked in bold. Efficiency of all other selections contribute to the ϵ^{other} defined in the Section G.2. The numbers for the two mass windows are shown: i) the nominal: $70 < m_{\text{inv}} < 130 \text{ GeV}/c^2$, and ii) wide mass window: $70 < m_{\text{inv}} < 200 \text{ GeV}/c^2$.

Process:	$Z \rightarrow \mu\mu$	$Z \rightarrow \mu + \tau_{\text{jet}}$	$t\bar{t}$	$W + \text{jet}$	$b\bar{b}$
$\sigma \times BR \text{ [pb]}$	2127	468	830	41457	22904478
Events for 30 fb^{-1}	63810000	14038200	24900000	1243720312	687134340000
HLT (single μ , $p_T > 19 \text{ GeV}/c$)	12113522	532024	1714285	12825148	1658017
only one, μ $p_T > 20 \text{ GeV}/c$	not applied	449087	1093926	11256357	1044637
$\tau_{\text{jet}} E_T > 45 \text{ GeV}$	not applied	82211	534301	2174934	51228
leading τ_{jet} $tk.$ $p_T > 40 \text{ GeV}/c$	not applied	17030	204978	466396	4609
τ tag	not applied	12379	137657	190844	2499
$m_T(\mu, MET) < 30 \text{ GeV}/c^2$	not applied	8588	21407	32485	1464
$\Delta\varphi(\mu, \tau_{\text{jet}}) < 175^\circ$	not applied	6820	20107	25663	1266
$E_{\nu_1, \nu_2} > 0$	not applied	3665	8531	5633	694
Electron veto	not applied	3032	2664	3839	504
Jet veto (1 central jet)	not applied	1666	682	1460	116
Mass window	7191968 \pm 28658	988 \pm 99	63\pm22	42 \pm 30	61 \pm 34
Mass window (wide)	7191968 \pm 28658	1291 \pm 113	206\pm40	271 \pm 75	75 \pm 37

to calibrate the τ jet energy scale using a selected sample of the γ +jet events [67].

To estimate the selection efficiency uncertainty due to the calorimetry scale the reconstructed jet E_T and missing transverse energy magnitudes were scaled by uncorrelated factors of 1 ± 0.03 for the jet scale and 1 ± 0.05 for the missing transverse energy scale. The variations on the selection efficiencies are presented below for both the signal and the background events. The selection uncertainty due to the calorimetry for the signal scale uncertainty is 8%.

G.5.1 Signal

The selection efficiency variation for the jet and missing transverse energy scales variation is presented in Figure G.1. Each selection is applied separately. It is clear that the most sensitive selection is cut on the τ – jet E_T , since with the threshold on 45 GeV, the selection is done at the deeply falling tail of the τ – jet E_T distribution, (Fig. G.3). The requirement for the positive reconstructed energy of the both neutrinos is not sensitive to the missing transverse energy scale, since it depends only on the angle between the muon and τ -jet transverse momenta (Section 6.3).

The selection efficiency variation for the case where each selection is imposed consecutively, after previous one, starting from the cut on the muon p_T is presented in Figure G.2. The large sensitivity of the τ – jet E_T cut is reduced from

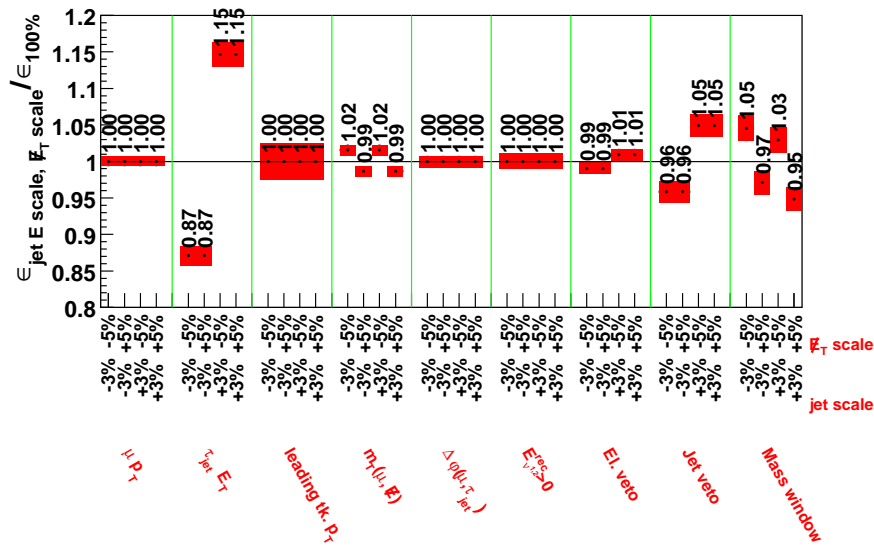


Figure G.1: Ratio of the selection efficiency, after the jet scale variation by $\pm 3\%$ and missing transverse energy scale variation by $\pm 5\%$, to the efficiency for the nominal calorimetry scale. Each selection is applied separately. The filled area shows the statistical uncertainty. Only selections involving calorimetric objects show the sensitivity to the calorimetry scale variations.

15% to 5% after requiring the leading track to have $p_T > 45$ GeV/c. The requirement for a large p_T for the leading track in the jet moves the jet spectrum toward higher E_T values and therefore the cut on E_T is more efficient than before the leading track p_T cut. Figure G.3 shows that the efficiency variations near the threshold are of order of 3% before and after the leading track p_T cut, but the E_T selection efficiency is higher after the leading track p_T cut, and the resulting relative efficiency change is smaller as shown in the Fig. G.2

G.5.2 Background

Figures G.4, G.5 and G.6 show the selection efficiency variation due to the calorimetry scale variation for the considered background processes. Due to the very low number of the Monte Carlo events after the last selection for the W +jet processes, the uncertainty after the jet veto selection was taken as the final selection uncertainty. For the $t\bar{t}$ process, (Fig. G.4), the selection uncertainty is 12%, for the W +jet, (Fig. G.5) the selection uncertainty is 6%. The $b\bar{b}$ selection uncertainty is 9%, (Fig. G.6).

The estimated uncertainties for the background events selection have very large statistical uncertainty, but due to the large signal to background ratio the

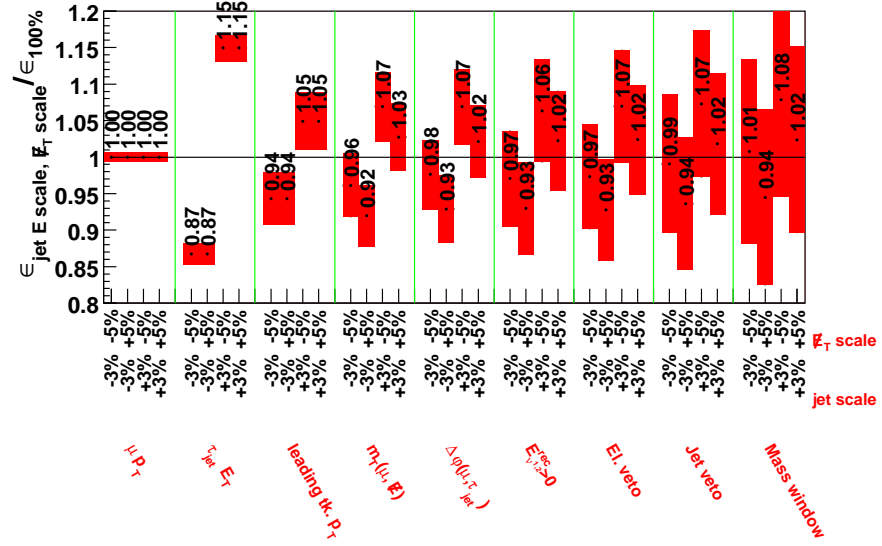


Figure G.2: Ratio of the selection efficiency after the jet scale variation by $\pm 3\%$ and missing transverse energy scale variation by $\pm 5\%$, to the efficiency for the nominal calorimetry scale. Each selection is applied consecutively, after the previous one, starting from the muon p_T cut. The filled area shows the statistical uncertainty. The maximal efficiency variation after all selections was taken as the selection uncertainty estimate.

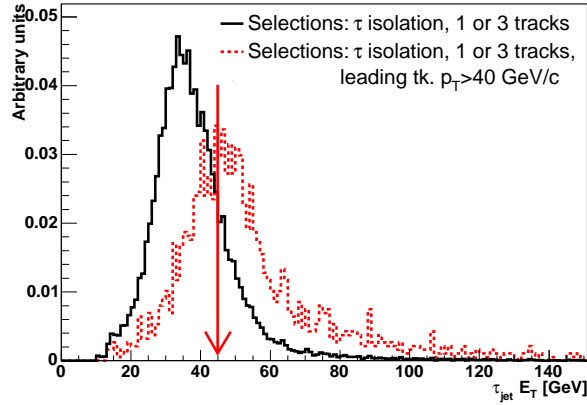


Figure G.3: The τ jet E_T distribution after the τ identification cuts before and after the leading track $p_T > 40$ GeV/c selection. The arrow marks the offline τ jet E_T cut on the value of 45 GeV. Both histograms are separately normalized to unit area.

contribution to the total τ tagging selection uncertainty from the background selection uncertainty is small, even for large relative uncertainty on the background events selection.

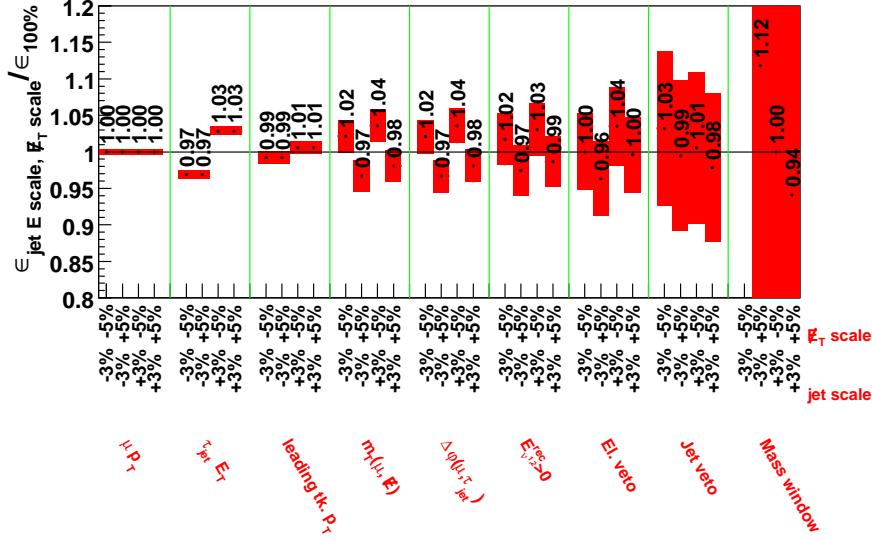


Figure G.4: Ratio of the selection efficiency after the jet scale variation by $\pm 3\%$ and missing transverse energy scale variation by $\pm 5\%$, to the efficiency for the nominal calorimetry scale for the $t\bar{t}$ events. Each selection is applied on the top of the previous one, starting from the muon p_T cut. The filled area shows the statistical uncertainty. The maximal efficiency variation after all selections was taken as the selection uncertainty estimate.

G.6 Results

G.6.1 Total uncertainty on the number of background events

As described in the Section G.2, the total background estimate uncertainty contains the process cross section uncertainty, the selection uncertainty and the Monte Carlo statistical uncertainty. For the cross section uncertainty it was assumed that the cross sections for considered processes will be measured. The expected statistical uncertainty on the measured cross section for the single leptonic $t\bar{t}$ is 0.23% for 30 fb^{-1} and the systematic uncertainty is expected to be of the order of 9.2% [84]. Here it is assumed that there will be very large number of Monte Carlo events available at the time, therefore the MC statistical

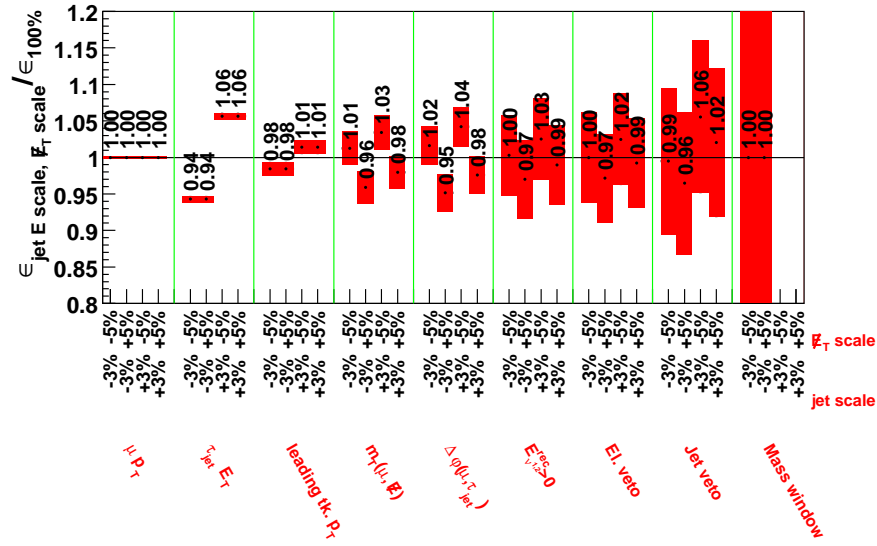


Figure G.5: Ratio of the selection efficiency after the jet scale variation by $\pm 3\%$ and missing transverse energy scale variation by $\pm 5\%$, to the efficiency for the nominal calorimetry scale for the W+jet events. Each selection is applied on the top of the previous one, starting from the muon p_T cut. The filled area shows the statistical uncertainty. The maximal efficiency variation after the jet veto selection was taken as the selection uncertainty estimate.

uncertainty is assumed to be negligible. Below, the uncertainties for the $t\bar{t}$ background are summarized. The total uncertainty is taken as a sum in quadrature of all contributions and is equal to 15.1%. The assumption of independence of all contributions is only approximate, since the systematic uncertainty on the cross section and the uncertainty on the offline selection depend on the common uncertainty on the calorimeter scale. For the W+jet and the $b\bar{b}$ similar uncertainties on the measured cross sections, as for the $t\bar{t}$ were assumed, as there is no detailed analysis on those processes available yet. Below the summary of all the contributions to the selection uncertainty for the background processes is shown:

$t\bar{t}$:	Xsec.	sys. uncert.		selection efficiency		MC stat.	Total
		9.2%	\oplus	12%	\oplus	0%	= 15.1%
W + jet:	Xsec.	sys. uncert.		selection efficiency		MC stat.	Total
		9.4 %	\oplus	6%	\oplus	0%	= 11.2%
QCD($b\bar{b}$ events):	Xsec.	sys. uncert.		selection efficiency		MC stat.	Total
		9.4 %	\oplus	9%	\oplus	0%	= 13%

The total uncertainty on the number of background events is taken as a sum in quadrature of all the individual uncertainties and is equal to 1.3%:

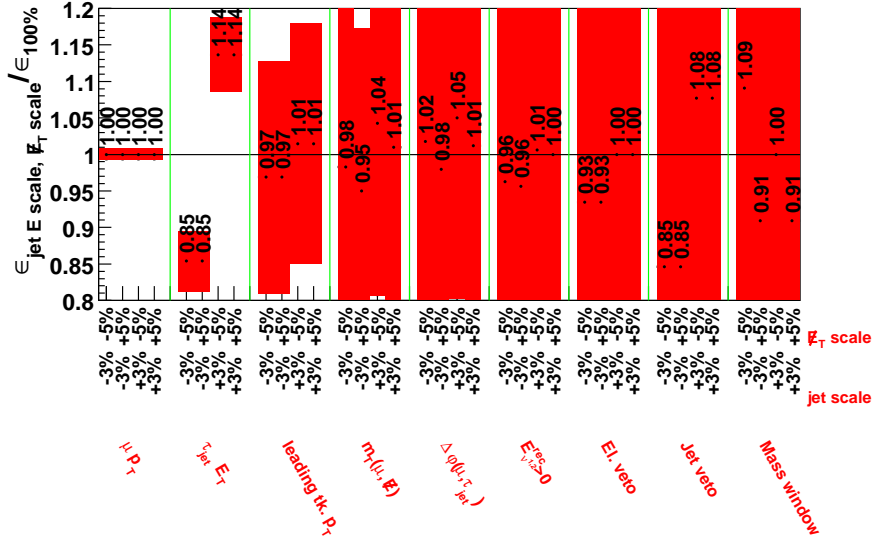


Figure G.6: Ratio of the selection efficiency after the jet scale variation by $\pm 3\%$ and missing transverse energy scale variation by $\pm 5\%$, to the efficiency for the nominal calorimetry scale for the $b\bar{b}$ events. Each selection is applied on the top of the previous one, starting from the muon p_T cut. The filled area shows the statistical uncertainty. The maximal efficiency variation after all selections was taken as the selection uncertainty estimate.

$$\frac{\Delta N_{background}}{N_{\mu+\tau jet}^{meas} - N_{\mu+\tau jet}^{tt} - N_{\mu+\tau jet}^{Wj} - N_{\mu+\tau jet}^{QCD}} = \frac{\sqrt{(0.151 \cdot 63)^2 + (0.112 \cdot 42)^2 + (0.13 \cdot 61)^2}}{988} = 1.3\%$$

G.6.2 Total uncertainty on the τ tag efficiency

The total uncertainty on the τ -tag efficiency is a sum of contributions from the signal events and from the background. Table G.3 summarizes all the contributions. The total relative uncertainty is 8.8%.

Table G.3: Contributions to the total measured τ tag efficiency relative uncertainty.

Source:	Number of $\mu \tau$ jet events	Calorimetry scale uncert.	Background uncertainty	Total
Contribution [%]:	3.4	8	1.3	8.8

G.7 Conclusions

The procedure for estimating the τ -tagging efficiency from the data has been proposed. The procedure uses τ leptons coming from the Z boson decays. The estimated uncertainty of the method is 9%. It is important to stress that the τ

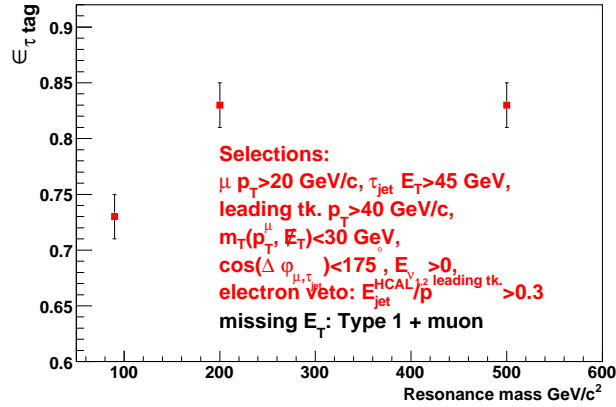


Figure G.7: The τ -tag efficiency for the τ leptons coming from the Z bosons decay and Higgs bosons with $m_H = 200$ and 500 GeV/c². The efficiency is plotted as a function of the τ mother particle mass.

tag efficiency measured for τ coming from Z boson decay is different from the τ tag efficiency for the τ from Higgs bosons decays for Higgs masses larger than the Z mass, (Fig. G.7). Although the τ -tagging does not include the kinematic selection the efficiency varies with the τ – jet energy due to the following effects:

- fraction of 3-prong events with at least one track beyond the signal cone - the more energetic τ jet is the more collimated it is, and less events are rejected due to the effect of signal tracks falling out of the signal cone and spoiling the isolation;
- fake track rate for highly collimated τ jets - for very energetic τ jet the signal tracks are very close in space. It may happen that different tracks share hits in the tracking detectors, which causes problems with the standard track reconstruction;
- the τ – jet energy scale is different for 1 and for 3-prong events, and the relative fraction of these events changes with the τ – jet energy;
- the τ – jet transverse energy distribution is very narrow, (Fig. G.3), and it allows for only one or two bins with high statistics, which is not enough to make reliable efficiency extrapolation to high τ – jet E_T region.

This means that there is no simple, data based way to use the efficiency measured from the Z events for the Higgs events. Rather, one has to get it from the Monte Carlo, with the careful checking of the result for the τ from Z, where the “direct” measurement will be possible. Prediction of the ratio of single to three prong τ events in $\tau - \text{jet } E_T$ bins may serve as a good Monte Carlo validation test, since this number can be measured directly from the data.

Bibliography

- [1] **LEP** Collaboration, “A combination of preliminary electroweak measurements and constraints on the standard model” **hep-ex/0412015**. 1, 2.4
- [2] S. Weinberg, “A model of leptons” *Phys. Rev. Lett.* **19** (1967) 1264–1266. 1
- [3] A. Salam, “Weak and electromagnetic interactions”. Originally printed in *Svartholm: Elementary Particle Theory, Proceedings Of The Nobel Symposium Held 1968 At Lerum, Sweden*, Stockholm 1968, 367-377. 1
- [4] J. F. Gunion, H. E. Haber, G. L. Kane, and S. Dawson, “The Higgs Hunter’s Guide”. 1
- [5] M. Carena and H. Haber, “Higgs Boson theory and Phenomenology” **hep-ph/0208209**. 1, 2.3
- [6] S. Weinberg, “Implications of dynamical symmetry breaking” *Phys. Rev.* **D13** (1976) 974–996. 1
- [7] C. Csaki, C. Grojean, H. Murayama, L. Pilo, and J. Terning, “Gauge theories on an interval: Unitarity without a Higgs” *Phys. Rev.* **D69** (2004) 055006, [**hep-ph/0305237**]. 1
- [8] M. C. Gonzalez-Garcia and Y. Nir, “Developments in neutrino physics” *Rev. Mod. Phys.* **75** (2003) 345–402, [**hep-ph/0202058**]. 1
- [9] A. Djouadi, “The anatomy of electro-weak symmetry breaking. I: The Higgs boson in the standard model” **hep-ph/0503172**. 1
- [10] A. D. Dolgov and Y. B. Zeldovich, “Cosmology and elementary particles” *Rev. Mod. Phys.* **53** (1981) 1–41. 1
- [11] V. Trimble, “Existence and Nature of Dark Matter in the Universe” *Annu. Rev. Astron. Astrophys* **25** (1987) 425. 1

- [12] B. Sadoulet, “Deciphering the nature of dark matter” *Rev. Mod. Phys.* **71** (1999) S197–S204. 1
- [13] **LEP SUSY Working Group** Collaboration, “LEPSUSYWG, ALEPH, DELPHI, L3 and OPAL experiments.”
<http://lepsusy.web.cern.ch/lepsusy/Welcome.html>. 1
- [14] M. Carena *et. al.*, “Report of the Tevatron Higgs working group”
hep-ph/0010338. 1
- [15] R. Kinnunen and A. Nikitenko, “Study of
 $H, A \rightarrow \tau^+\tau^- \rightarrow l + \tau jet + E_T^{miss}$ ” *CMS NOTE* 1997/106. 1
- [16] **CMS** Collaboration, “Object-oriented Reconstruction for CMS Analysis”
<http://cmsdoc.cern.ch/orca/>. 1
- [17] **CMS** Collaboration, “CMS Simulation and Reconstruction Package”
<http://cmsdoc.cern.ch/cmsim/cmsim.html>. 1
- [18] **CMS** Collaboration, “Object oriented Simulation for CMS Analysis and Reconstruction” <http://cmsdoc.cern.ch/oscar/>. 1, 5.2
- [19] A. Kalinowski, M. Konecki, and D. Kotliński, “Search for MSSM heavy neutral Higgs boson in $\tau + \tau \rightarrow \mu + \text{jet}$ decay mode” *CMS NOTE*-2006/105. 1
- [20] C. Buttar *et. al.*, “Les Houches physics at TeV colliders 2005, standard model, QCD, EW, and Higgs working group: Summary report”
hep-ph/0604120. 1
- [21] A. Kalinowski and A. Nikitenko, “Measurement of the τ tag efficiency using the $Z \rightarrow \tau\tau \rightarrow \mu + \text{hadrons} + X$ events.” *CMS NOTE*-2006/074. 1
- [22] M. J. G. Veltman, “Second threshold in weak interactions” *Acta Phys. Polon.* **B8** (1977) 475. 2.1
- [23] A. Djouadi, “The anatomy of electro-weak symmetry breaking. II: The Higgs bosons in the minimal supersymmetric model” hep-ph/0503173. 2.1, 2.1
- [24] S. Martin, “A Supersymmetry primer” hep-ph/9709356. 2.1, 2.2

- [25] F. Gabbiani, E. Gabrielli, A. Masiero, and L. Silvestrini, “A complete analysis of FCNC and CP constraints in general SUSY extensions of the standard model” *Nucl. Phys.* **B477** (1996) 321–352, [[hep-ph/9604387](#)]. 2.4
- [26] S. Dimopoulos and D. W. Sutter, “The Supersymmetric flavor problem” *Nucl. Phys.* **B452** (1995) 496–512, [[hep-ph/9504415](#)]. 2.4
- [27] H. Georgi, “The flavour problem” *Phys. Lett.* **B169** (1986) 231. 2.4
- [28] S. Dimopoulos and H. Georgi, “Softly broken supersymmetry and SU(5)” *Nucl. Phys.* **B193** (1981) 150. 2.4, 2.4
- [29] M. Dine and A. E. Nelson, “Dynamical supersymmetry breaking at low-energies” *Phys. Rev.* **D48** (1993) 1277–1287, [[hep-ph/9303230](#)]. 2.4
- [30] M. Dine, A. E. Nelson, and Y. Shirman, “Low-energy dynamical supersymmetry breaking simplified” *Phys. Rev.* **D51** (1995) 1362–1370, [[hep-ph/9408384](#)]. 2.4
- [31] A. H. Chamseddine, R. Arnowitt, and P. Nath, “Locally supersymmetric grand unification” *Phys. Rev. Lett.* **49** (1982) 970. 2.4
- [32] L. J. Hall, J. D. Lykken, and S. Weinberg, “Supergravity as the messenger of supersymmetry breaking” *Phys. Rev.* **D27** (1983) 2359–2378. 2.4
- [33] M. Carena, S. Heinemeyer, C. E. M. Wagner, and G. Weiglein, “Suggestions for benchmark scenarios for MSSM Higgs boson searches at hadron colliders” *Eur. Phys. J.* **C26** (2003) 601–607, [[hep-ph/0202167](#)]. 2.4
- [34] S. Heinemeyer, W. Hollik, and G. Weiglein, “Constraints on $\tan(\beta)$ in the MSSM from the upper bound on the mass of the lightest Higgs boson” *JHEP* **06** (2000) 009, [[hep-ph/9909540](#)]. 2.4
- [35] M. Carena, S. Heinemeyer, C. E. M. Wagner, and G. Weiglein, “MSSM Higgs boson searches at the Tevatron and the LHC: Impact of different benchmark scenarios” *Eur. Phys. J.* **C45** (2006) 797–814, [[hep-ph/0511023](#)]. 2.4, 2.4, 7.2
- [36] **LEP Higgs Working Group** Collaboration, “Searches for the neutral Higgs bosons of the MSSM: Preliminary combined results using LEP data collected at energies up to 209-GeV” [hep-ex/0107030](#). 2.4

-
- [37] V. M. Abazov *et. al.*, “Search for neutral supersymmetric Higgs bosons in multijet events at $s^{*}(1/2) = 1.96\text{-TeV}$ ” *Phys. Rev. Lett.* **95** (2005) 151801, [[hep-ex/0504018](#)]. 2.4
 - [38] A. Abulencia *et. al.*, “Search for neutral MSSM Higgs bosons decaying to tau pairs in p anti-p collisions at $s^{*}(1/2) = 1.96\text{-TeV}$ ” *Phys. Rev. Lett.* **96** (2006) 011802, [[hep-ex/0508051](#)]. 2.4
 - [39] “<http://www.feynhiggs.de/>”. 3.1
 - [40] S. Heinemeyer, “MSSM Higgs physics at higher orders” [hep-ph/0407244](#). 3.1
 - [41] M. Spira <http://people.web.psi.ch/spira/proglist.html>. 3.1
 - [42] S. Lehti and V. Petila, “SigmaBr6, a c++ interface to HDECAY,HIGLU,HQQ,VV2H,V2HV” CMS IN 2005-005. 3.1
 - [43] S. Eidelman *et. al.*, “Review of Particle Physics” *Physics Letters B* **592** (2004) 1+. 3.1, G.2
 - [44] T. Sjöstrand, P. Eden, C. Friberg, L. Lönnblad, G. Miu, S. Mrenna, and E. Norrbin, “High-energy-physics event generation with PYTHIA 6.1” *Comput. Phys. Commun.* **135** (2001) 238–259, [[hep-ph/0010017](#)]. 3.2, 5.1.1, 5.1.2, A.1, B
 - [45] A. Pukhov *et. al.*, “CompHEP: A package for evaluation of Feynman diagrams and integration over multi-particle phase space. User’s manual for version 33” [hep-ph/9908288](#). 3.2, 3.1
 - [46] M. Beneke, “Workshop on Standard Model Physics (and more) at the LHC Top Quark Physic” [cernrep / 2000-004](#). 3.1, B
 - [47] M. Beneke *et. al.*, “Top quark physics” [hep-ph/0003033](#). 3.1
 - [48] A. Belyaev and E. Boos, “Single top quark $t W + X$ production at the LHC: A closer look” *Phys. Rev.* **D63** (2001) 034012, [[hep-ph/0003260](#)]. 3.1
 - [49] J. Campbell, calculations with the MCFM program. Private communication. 3.1, G.1
 - [50] M. Battaglia *et. al.*, “Updated post-WMAP benchmarks for supersymmetry” *Eur. Phys. J.* **C33** (2004) 273–296, [[hep-ph/0306219](#)]. 3.2

- [51] W. Beenakker, R. Hopker, and M. Spira, “PROSPINO: A program for the PROduction of Supersymmetric Particles In Next-to-leading Order QCD” `hep-ph/9611232`. 3.2
- [52] CMS Collaboration, “CMS Physics Technical Design Report, Volume I: Software and Detector Performance” CERN-LHCC-2006-001. 4.1, 4.1, 4.2, 4.2.2.1, 4.4, 4.2.2.2, 4.5, 4.6, 4.4, 4.4.1, 4.2, 4.8, 4.4.4, 4.9, 4.4.4, 4.10, 4.4.5, 4.11, 4.12, 4.13, 4.14, 5.1, 5.2, 5.3, 6.1.1, 6.4.1, 8, G.2, G.5
- [53] M. H. Seymour, “Jets in hadron collisions” `hep-ph/0007051`. 4.4.5
- [54] T. Affolder *et. al.*, “Charged jet evolution and the underlying event in proton-antiproton collisions at 1.8 TeV” *Phys. Rev.* **D 65** (2002). 5.1.1
- [55] D. Acosta *et. al.*, “The underlying event in hard interactions at the Tevatron anti-p p collider” *Phys. Rev.* **D70** (2004) 072002, [`hep-ex/0404004`]. 5.1.1
- [56] D. Acosta *et. al.*, “The Underlying Event at the LHC” CMS NOTE-2006/067. 5.1.1
- [57] B. Andersson, “The Lund model” *Camb. Monogr. Part. Phys. Nucl. Phys. Cosmol.* **7** (1997) 1–471. 5.1.1
- [58] H. L. Lai *et. al.*, “Global QCD analysis of parton structure of the nucleon: CTEQ5 parton distributions” *Eur. Phys. J.* **C12** (2000) 375–392, [`hep-ph/9903282`]. 5.1.2
- [59] CMS Collaboration, “CMS Physics Generators Interface” <http://cmsdoc.cern.ch/cms00/projects/CMKIN/index.html>. 5.1.2
- [60] S. Jadach, Z. Was, R. Decker, and J. H. Kuhn, “The tau decay library TAUOLA: Version 2.4” *Comput. Phys. Commun.* **76** (1993) 361–380. 5.1.2
- [61] <http://cmsdoc.cern.ch/cms/production/www/html/general/index.html>. 5.1.2
- [62] <http://batch.web.cern.ch/batch/>. 5.1.2
- [63] S. Agostinelli *et. al.*, “GEANT 4– a simulation toolkit” *Nucl. Inst. & Meth. in Phys. Res.* **506** (2003) 250–303. 5.2

- [64] **CMS** Collaboration, “The TriDAS Project Technical Design Report, Volume 1: The Trigger Systems” **CERN/LHCC 2000-38**. 6.1, 6.1.1
- [65] **CMS** Collaboration, “The TriDAS Project Technical Design Report, Volume 2: Data Acquisition and High-Level Trigger” **CERN/LHCC 2002-26**. 6.1, B, G.4.1
- [66] S. Eno, S. Dasu, W. Smith, R. Kinnuen, and A. Nikitenko, “A Study of a First and Second Level Tau Trigger” **CMS NOTE-2000/055**. 6.1.1, 6.1.2
- [67] S. Gennai *et. al.*, “Tau jet reconstruction and tagging with CMS” **CMS NOTE-2006/028**. 6.1.2, 6.2.1, G.1, G.5
- [68] D. Kotliński and A. Nikitenko, “Study of a Level-3 Tau Trigger with the Pixel Detector” **CMS NOTE-2001/017**. 6.1.2
- [69] N. Amapane, M. Fierro, and K. M., “High Level Trigger Algorithms for Muon Isolation” **CMS NOTE-2002/040**. 6.1.2
- [70] T. Speer *et. al.*, “Track reconstruction in the CMS tracker” *Nucl. Instrum. Meth.* **A559** (2006) 143–147. 6.1.2
- [71] S. Lethi, “Tagging b-Jets in $b\bar{b}H_{SUSY} \rightarrow \tau\tau$ ” **CMS NOTE-2001/019**. 6.2.2.3
- [72] R. Demina *et. al.*, “Study of Cell Energy Thresholds in CMS Calorimeters for Jet Reconstruction” **CMS AN-2005/039**. 6.2.2.4
- [73] R. Brun and F. Rademakers, “Proceedings AIHENP’96 Workshop, Lausanne, Sep. 1996, ROOT - An Object Oriented Data Analysis Framework” *Nucl. Inst. & Meth. in Phys. Res.* **A389** (1997) 81–86. <http://root.cern.ch/>. 6.3.2
- [74] S. Haywood *et. al.*, “Electroweak physics” **hep-ph/0003275**. 6.4.2
- [75] S. Lehti, “Observability of bbZ events at the CMS as a benchmark for MSSM bbH search” **CMS NOTE-2006/099**. 6.4.2
- [76] S. I. Bitjukov and N. V. Krasnikov, “New physics discovery potential in future experiments” *Mod. Phys. Lett.* **A13** (1998) 3235–3249. 7.1
- [77] V. Bartsch and G. Quast, “Expected Signal Observability at Future Experiments” **CMS NOTE-2005/004**. 7.1

- [78] CMS Collaboration, “CMS Physics Technical Design Report, Volume II: Software and Detector Performance” CERN-LHCC-2006-XXX. 8.1
- [79] R. Kinnunen, S. Lehti, F. Moortgat, A. Nikitenko, and M. Spira, “Measurement of the $H/A \rightarrow \tau\tau$ cross section and possible constraints on $\tan\beta$ ” *Eur. Phys. J.* **C40N5** (2005) 23–32, [hep-ph/0503075]. A.1, G.1, G.4.2
- [80] J. Campbell, R. K. Ellis, F. Maltoni, and S. Willenbrock, “Higgs boson production in association with a single bottom quark” *Phys. Rev.* **D67** (2003) 095002, [hep-ph/0204093]. A.1
- [81] M. Konecki, Private communication. B, B.2
- [82] R. Kinnunen, S. Lehti, F. Moortgat, A. Nikitenko, and M. Spira, “Estimate of $\tan\beta$ measurement precision in $H/A \rightarrow \tau\tau$ and $H^\pm \rightarrow \tau\nu$ in CMS” CMS NOTE-2004/027. G.1
- [83] N. Kidonakis and R. Vogt, “Next-to-next-to-leading order soft-gluon corrections in top quark hadroproduction” *Phys. Rev.* **D68** (2003) 114014, [hep-ph/0308222]. G.1
- [84] J. D’Hondt, J. Heyninck, and S. Lowette, “Measurement of the cross section of single leptonic $t\bar{t}$ events” CMS NOTE-2006/064. G.6.1